ANALYSIS AND DESIGN OF WIDEBAND PASSIVE MIXER-FIRST RECEIVERS

A Dissertation

Presented to the Faculty of the Graduate School

of Cornell University

in Partial Fulfillment of the Requirements for the Degree of

Doctor of Philosophy

by

Caroline Jayne Andrews

August 2012

ANALYSIS AND DESIGN OF WIDEBAND PASSIVE MIXER-FIRST RECEIVERS

Caroline Jayne Andrews, Ph.D.

Cornell University 2012

This dissertation focuses on the design of wideband SAW-less receivers for software-defined radios. The entire body of work is based on a single RF front-end architecture type: a passive mixer connected directly to the antenna port of the radio, without an LNA or matching network up front. This structure is inherently wideband which allows for a single receiver front-end to operate at a wide range of frequencies, as tuned by its local oscillator (LO). Additionally, the mixer exhibits the property of transparency from the baseband port of the radio to the RF port of the radio, and vice versa. The focus of the first half of the thesis is on developing a simple theoretical framework for the impedance characteristics of the passive mixer, and implementing a maximally flexible receiver which utilizes the mixer's transparency to the fullest extent. Additionally, it is shown that mixing with 8 non-overlapping phases instead of the traditional 4 has benefits beyond harmonic rejection extending to improved noise performance and increased impedance tuning range. This receiver exhibits low noise figure (~3dB), excellent wideband linearity (IIP3≥25dBm), and unprecedented RF impedance control from the baseband side of the passive mixer. Another wideband receiver is presented which explores increasing the number of LO phases even further to 16 and 32, increasing the impedance matching range. The same chip contains a circuit technique for alleviating the shunting effects of LO phase overlap on mixer conversion gain, noise, and impedance match range. Finally in a new design, the power consumption of the receiver architecture is decreased by a factor of 5x (and not scaling with RF frequency). This is done using

a resonant LO drive with 8 non-overlapping phases, incorporating the large mixer gate capacitance directly into the LC tank of the VCO. Baseband power consumption is also reduced by reusing current in the four baseband amplifier channels, and performing harmonic rejection, all in one stage of amplification.

BIOGRAPHICAL SKETCH

Caroline Andrews was born in Dallas, Texas in 1986, but did not stay for long. She spent her childhood in England and Switzerland, and went to high school in Ellicott City, Maryland. She then attended the University of Virginia where she wore the honors of Honor, receiving the Bachelor of Science degree in Electrical Engineering in 2008. In that same year she moved to Cornell University for graduate school and joined Prof. Alyosha Molnar's lab as his third PhD student.

To my parents

ACKNOWLEDGEMENTS

I would like to thank the many individuals who supported me in at least as many different ways over the past four years:

My advisor, Al Molnar, for putting so much trust in and giving so much responsibility to someone who started out knowing so little. Also for giving me the freedom to occasionally say ‘no’.

My other committee members, Alyssa Apsel, David Winkler, and Ehsan Afshari, for helpful discussions about my work and my life choices.

My office mates, Albert Wang and Ben Johnson, it hurts to think about how many hours and nights we spent together in that room.

My other lab mates, Patrick Gill, Changhyuk Lee, Sriram Sivaramakrishnan, and Dong Yang. I’m sorry I didn’t clean up the lab better before I left.

My Masters of Engineering students, Garret Phillips, Isaac Wang, and especially Luke Diamente, without whom Chapter 5 would not exist.

My undergraduate research students, Chad Watson, Adam Mendrela, and Kevin Boyle who put up with my often conflicted priorities.

All of my friends in Ithaca and beyond who were always there when I popped back up to the surface occasionally.

This work was supported by Irwin and Joan Jacobs Fellowship, the National Science Foundation, some sweat, a few tears (no blood, but a few soldering iron burns), and a good dose of hobo science.

TABLE OF CONTENTS

LIST OF TABLES

LIST OF FIGURES

CHAPTER 1

INTRODUCTION

1.1 Background

Demand for highly integrated, multifunction wireless transceivers has exploded over the last decade, driving innovations in radio architecture to permit on-the-fly programmability of various radio parameters. Although many key parameters have been made fully flexible, the physical interface to the antenna has not.

After the matching network, traditional receivers have an LNA which must be low noise, provide power gain, and exhibit good linearity, while providing an input impedance that is matched. This is not entirely straightforward: a simple resistive matching network always results in a noise figure above 3dB. In fact, a reasonable definition for an LNA is an amplifier which provides a real impedance match while maintaining a sub-3dB noise figure. For applications requiring low noise figure and a good impedance match, a resonant antenna impedance matching network is typically used. Such a network's passive RF components are not easily tunable over a wide range of values [1,2]. To make matters worse, the impedance of the antenna and matching network is strongly frequency dependent, severely limiting channel tuning range for high performance receivers.

Because performance trade offs tend to fall so heavily on the receiver front-end, and involve relatively inflexible components, many multi-band systems which receive a range of frequencies use multiple, parallel front-ends, tuned to different frequencies, using distinct matching networks and LNAs [3,4]. Alternatively, an LNA with wideband impedance matching and good noise figure *can* be achieved using either a wideband amplifier with resistive feedback [5,6], or with a noise-canceled LNA [7]. Such designs intrinsically require large amounts of power to operate at RF frequencies while maintaining a constant antenna impedance, and still generally provide a relatively fixed input impedance. At the other extreme, applications requiring low power consumption and cost can simply forgo the LNA completely, connecting directly to a passive mixer [8,9].

As gate lengths continue to fall, smaller, faster MOSFETs allow sampling passive mixers to operate in the gigahertz range with better linearity and lower power consumption than traditional active mixers [8–10]. These circuits have unusual properties, such as very high linearity [9] and a capacity to pass the impedance presented at one port (ie. the baseband port) to the other port (ie. the RF port) [11]. This transparency property has been used to translate baseband filtering onto a mixer's RF port, suppressing wideband interference [8, 12–14]. However until very recently, these improvements have come at the cost of significantly higher noise figure (typically 5-6dB) [8, 9, 12].

In this dissertation we show that using a passive mixer without an LNA in a receiver front-end can achieve both good noise figure, very high linearity, and baseband controllable impedance matching. We obtain a simple linear time-invariant model for such a passive mixer's input impedance, which can also be utilized to compute noise figure. We demonstrate that the input impedance can be tuned through the baseband port of the mixer with easily tunable baseband circuits.

1.2 Thesis Organization

This dissertation examines and exploits the properties of passive mixers in various ways throughout its chapters. In Chapter 2 we examine the impedance translation properties of the 4 and 8 phase passive mixers and how this relates to input impedance, noise performance, and tunable wideband filtering and rejection. We demonstrate a method for controlling the real component of input impedance of the mixer (and receiver) by tuning the values of resistors coupled to its baseband port. We also demonstrate a way to manipulate the imaginary input impedance using cross-connected feedback paths between the in-phase and quadrature paths of the baseband ports of the mixer.

In Chapter 3 we demonstrate an implementation of many of the ideas presented in Chapter 2. We present a passive mixer-first receiver fabricated in 65nm CMOS which can be tuned from .01 to 2.4GHz. The receiver includes both 4 and 8 LO phase mixers, and their LO generation circuitry, tunable sampling capacitors, baseband amplifiers with tunable feedback resistors, and second stage harmonic recombination amplifiers. The receiver's input impedance can be tuned to achieve <-10dB S_{11} across the whole range of operation. The RX bandwidth can be adjusted from >40MHz to <1MHz by switching in more sampling capacitors on the baseband side of the mixers.

In Chapter 4 we expand on the concepts developed earlier and incorporate a study into the various loss mechanisms which affect the mixer's performance, including LO phase overlap and harmonic downconversion. We present a receiver similar to that of Chapter 3, with the number of LO phases increased to a selectable N =4, 8, 16 or 32. We show in measurement that increasing the number of phases beyond 8 further increases the impedance matching range. We also measure the rejection of higher harmonics than in the 8-phase mixing case when utilizing 16 or 32 phases. Additionally we investigate the effect of overlap in the mixer LO phases and its effect on noise performance in input impedance. Finally we present a method for counter-acting the shunting due to LO phase overlap, and measure its effects in a comparative study.

Finally in Chapter 5 we begin to scale down the power consumption of the architecture while maintaining most of the same functionalities. The main problem with driving passive mixers in wideband systems is that the power consumption scales linearly with frequency, since the LO is essentially a digital waveform driving large gates (the mixers). In this chapter we implement a novel resonant 8-phase LO pulse generation topology which incorporates the mixer switches directly into a resonant tank. To first order this removes the direct frequency relation to power consumption. Additionally, in order to achieve harmonic rejection and lower noise figure (as discussed in Chapter 2), an 8-phase mixer is desirable. However this requires twice as many baseband amplifiers, since there are 4 differential mixer outputs instead of two. In this receiver we employ current reuse in the baseband to share input pair bias current among the 4 baseband channels, while implementing harmonic rejection at the same time. We also demonstrate a technique for shorting anti-phase mixers together directly on their baseband ports in order to halve the effective number of phases of the receiver and double the RX frequency without any additional high frequency circuits.

CHAPTER 2

IMPLICATIONS OF PASSIVE MIXER TRANSPARENCY FOR IMPEDANCE MATCHING AND NOISE FIGURE IN PASSIVE MIXER-FIRST RECEIVERS

In this chapter, a class of passive mixer-first, LNA-less receivers is analyzed in depth. Quadrature passive mixers are shown to present the impedance of their baseband port to the RF port and vice-versa. This transparency property, in combination with resistive feedback differential amplifiers, and "complex" feedback between the I and Q paths, can be used to control the impedance at the RF port. This impedance can be tuned using only baseband components (i.e. resistors). The noise limits of such an architecture are analyzed and simulated, and are shown to be comparable to standard RF-LNA-first receivers. Accounting for the higher harmonics of the LO frequency proves critical in accurately analyzing the behavior of these circuits and their ability to provide an impedance match with low noise figure. Additionally, it is shown that expanding quadrature passive mixers to harmonic rejection mixers allows for even better noise performance and wider matching range.

2.1 Introduction

In this chapter we analyze the transparency of passive mixers in detail, especially analyzing a method by which this transparency can be used to provide a baseband-tunable, complex impedance match to the antenna. The bidirectional nature of passive mixers also causes their noise figure to depend strongly on the circuits at both the RF and IF interfaces [11]. Here we analyze the fundamental dependencies between RF and IF impedance and limits on both matching and noise figure (NF). We show that both NF and matching can be made competitive with traditional LNA-first receivers, while

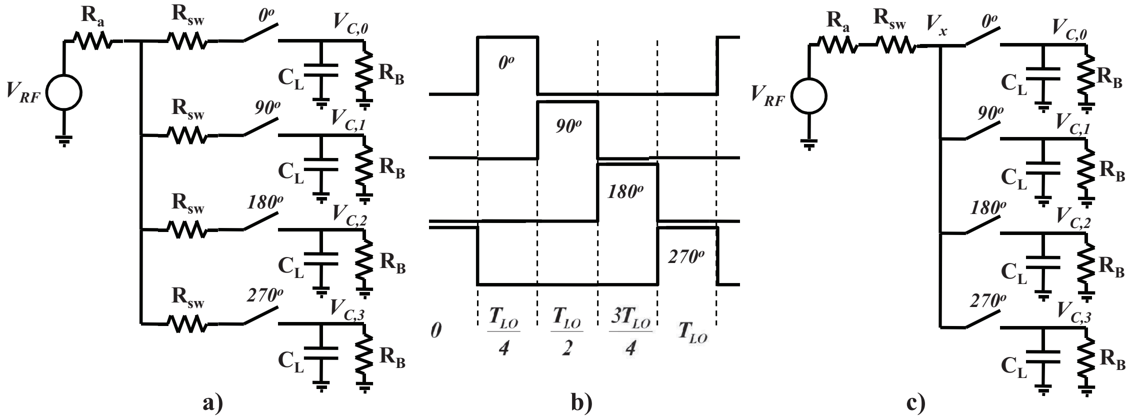

Figure 2.1: a) Simplified circuit model of 4-phase passive mixer, b) LO driving waveforms, c) equivalent model to a), with R_{sw} lumped with R_a based on non-overlapping nature of the waveforms in the middle.

providing high-Q front end filtering (which is good for linearity: [9, 12]) and extreme frequency tuning range. These advantages imply that passive mixer-first receivers will likely provide the next step in improving the flexibility and performance of highly integrated wireless receivers.

2.2 Passive Mixer Transparency: 1st Order Analysis

The passive mixer analyzed here contains four switches (transistors) which are successively turned on in four non-overlapping, 25% duty-cycle phases over the course of one local oscillator (LO) period [9, 12, 15–17]. These non-overlapping pulses are necessary for preventing the I-Q crosstalk described in [11]. The input port of the mixer is connected directly to the antenna port. The switches sample the RF voltage onto four capacitors loaded by the baseband resistances R_B. The phase-split nature of the LO, the mixer, and hence the amplifiers, produces differential baseband signals with both I (from the 0° and 180° switches) and Q (from 90° and 270°) components.

2.2.1 Impedance Analysis

The analysis begins with a simplified model of a 4-phase passive mixer with non-overlapping, 25% duty cycle, quadrature LO pulses, as shown in Fig. 2.1a and b. The model treats the switches as ideal except for a small series resistance, R_{sw}, which represents the on-resistance of the switching MOSFET. Since the LO pulses are completely non-overlapping, only one R_{sw} is active at a time, so the series resistance of all of the switches can be lumped together and treated as a single resistor of the same value, as shown in Fig. 2.1c.

If we treat the antenna impedance as a resistor R_a, (neglecting its reactive components for the moment) then the entire RF portion of the circuit can be modeled as a single lumped series combination of R_a and R_{sw} in series with a parallel array of four ideal switches. We can define an effective antenna resistance:

$$R'_a = R_{sw} + R_a \tag{2.1}$$

We now define a virtual voltage V_x at the node in between R_{sw} and the ideal switches. The baseband port of the switches is loaded by the parallel combination of a filtering capacitor C_L and the amplifier input resistance, R_B. If the time constants $R_B C_L$ and $R'_a C_L$ are significantly larger than the LO period, T_{LO}, then we can approximate these capacitors as holding their voltage constant over a given LO cycle. For in-band signals, the input from the antenna can be approximated as a sinusoid with fundamental frequency $\omega_{LO} = 2\pi/T_{LO}$ and time varying phase $\phi(t)$ and amplitude $A(t)$, which capture both modulation and offset frequency of the received signal. If the amplitude and phase offset change slowly relative to T_{LO} they can be approximated as constant over a given LO period, and the input can be approximated as:

$$V_{RF}(t) = A\cos(\omega_{LO}t + \phi). \tag{2.2}$$

To compute the input impedance presented by the mixer to the antenna, we start by computing the voltage across each of the output capacitors in response to the input. Specifically, each capacitor will continuously dissipate current through its resistive load, R_B, such that the m-th capacitor ($m = 0, 1, 2, 3$) dissipates a current of $I_{C,m} = V_{C,m}/R_B$. For a full cycle of the LO, assuming $R_B C_L \gg T_{LO}$, this corresponds to a charge of $Q_m = T_{LO} V_{C,m}/R_B$. Meanwhile, for each cycle of the LO, this charge is replenished from the antenna during the quarter cycle during which the m-th switch is closed. Assuming that the voltage across the m-th capacitor, $V_{C,m}$ is at steady state (that is, assuming $\phi(t)$ and $A(t)$ change slowly relative to the time constants $R_B C_L$ and $R'_a C_L$), conservation of charge implies that charge dissipated by R_B is balanced by the integral of the input current during a given quarter-LO cycle. To simplify this and future integrals, we also introduce a time shift in the integration limits of $-T_{LO}/8$.

$$Q_m = \frac{V_{C,m} T_{LO}}{R_B} = \int\limits_{m\frac{T_{LO}}{4} - \frac{T_{LO}}{8}}^{(m+1)\frac{T_{LO}}{4} - \frac{T_{LO}}{8}} \frac{V_{RF} - V_{C,m}}{R'_a} dt \qquad m = 0, 1, 2, 3 \tag{2.3}$$

Substituting in (2.2) for V_{RF} and solving for $V_{C,m}$ results in the expression:

$$V_{C,m} = \frac{2\sqrt{2}}{\pi} \frac{R_B}{R_B + 4R'_a} A \cos(\phi + \frac{m\pi}{2}) \tag{2.4}$$

Note that this implies that that the output of the mixer depends not just on the strength of the RF input, but on the *relative* impedance of the antenna (R'_a) compared to the baseband (R_B).

Passive mixers allow current to flow in both directions through the switches, from the RF port to the IF, and back. This means there will be a return or re-radiation current generated by the difference between the voltage levels maintained on the filter capacitors of the mixer and the input on the antenna. Because the virtual voltage at V_x in Fig. 2.1c is always short-circuited to one of the output capacitors, it can be described by a stair-

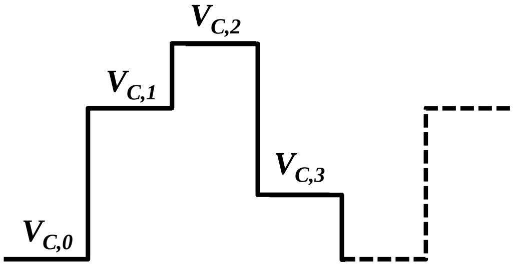

Figure 2.2: Approximation of waveform V_x from Fig. 1

step waveform (shown in Fig. 2.2) with four phases corresponding to the four phases of the LO, and with a voltage at each phase corresponding to one of the output capacitors.

In order to characterize the effective impedance seen by the antenna, we find the current flowing out of the antenna into the receiver. In the time domain this will be:

$$I_A(t) = \frac{V_{RF}(t) - V_x(t)}{R'_a} \tag{2.5}$$

We will now look for the impedance seen by the antenna for a near-zero-IF system, where $\omega_{RF} \approx \omega_{LO}$. To find $I_A(t)$ we extract the component of V_x which resides at this frequency using a Fourier series representation of the signal over a period of time T_{LO}, and extract the fundamental term. Substituting (2.4) into the waveform shown in Fig. 2.2 yields a term for the fundamental at ω_{LO}:

$$\begin{aligned} V_{x,fund}(t) &= A\frac{8}{\pi^2}\frac{R_B}{R_B + 4R'_a}\cos(\omega_{LO}t + \phi) \\ &= V_{RF}(\omega_{LO})\frac{8}{\pi^2}\frac{R_B}{R_B + 4R'_a} \end{aligned} \tag{2.6}$$

from which we can compute $I_{A,fund}(t)$:

$$\begin{aligned} I_{A,fund}(t) &= \frac{V_{RF}(t) - V_{x,fund}(t)}{R'_a} \\ &= V_{RF}(t)\frac{4R'_a + (1 - 8/\pi^2)R_B}{R'_a R_B + 4R'^2_a} \end{aligned} \tag{2.7}$$

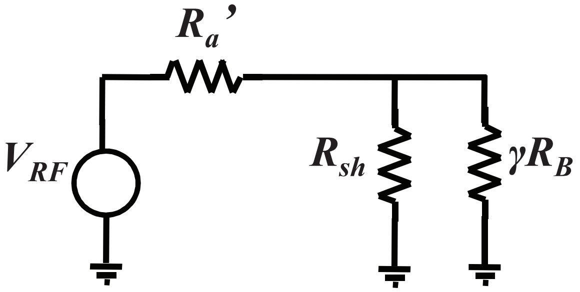

Figure 2.3: LTI equivalent circuit for passive mixer with R_{sh} due to harmonics and impedance-transformed R_B.

The current described in (2.7) looks like the input V_{RF} transformed by a combination of R'_a and R_B. Several observations can be made from equation (2.7). The first is that as $R_B \rightarrow 0$, $I_A \rightarrow V_{RF}/R'_a$, implying that R'_a acts in series with R_B. The second is that as $R_B \rightarrow \infty$, $I_A \rightarrow V_{RF}(1 - 8/\pi^2)/R'_a$, implying that there is additional antenna-dependent shunting in parallel with R_B. This leads us to introduce the time-invariant model in Fig. 2.3 for the original time-varying circuit in Fig. 2.1. This circuit accounts for the linear time-varying (LTV) effects of the switches with an impedance transform term γ acting on R_B, and an additional resistance R_{sh}, in shunt with the baseband resistance R_B. R_{sh} emerges from the charge balance in (2.3). However, as we will show in section 2.3.1, *R_{sh} in fact represents power lost due to up-conversion by harmonics of the LO* through the switches to the antenna.

Given the model in Fig. 2.3 we can write a simple expression for its current I_A.

$$I_A(\omega_{LO}) = V_{RF}(\omega_{LO})\frac{\gamma R_B + R_{sh}}{R'_a\gamma R_B + R'_a R_{sh} + R_{sh}\gamma R_B} \tag{2.8}$$

To find the values for the scaling factor γ and the virtual shunt resistance R_{sh} we set the current in our LTV circuit (2.7) equal to the current for our LTI model (2.8).

$$\gamma = \frac{2}{\pi^2} \approx 0.203 \tag{2.9}$$

$$R_{sh} = R'_a \frac{4\gamma}{1 - 4\gamma} \approx 4.3R'_a \tag{2.10}$$

Note that while R_{sh} is proportional to R'_a in (2.10), this only holds as long as R_a is constant across all frequencies, once this ceases to be true, a more complex description is required, as explored in section 2.5.

2.2.2 Consequence: Impedance Matching

This model for the passive mixer shows that the impedance seen by the antenna through a quadrature passive mixer consists of the parallel combination of R_{sh} and γR_B in series with the switch resistance R_{sw}. Specifically, this impedance becomes:

$$R_{in} = R_{sw} + \gamma R_B || R_{sh} \tag{2.11}$$

This result indicates that the impedance seen at the antenna interface can be modified by changing R_B. In particular, (2.11) shows that changing baseband resistance can be used to tune the input resistance R_{in} over a range that is limited by the properties of the mixer:

$$R_{sw} < R_{in} < R_{sw} + R_{sh} \tag{2.12}$$

We have confirmed this impedance analysis using numerical circuit simulation (PSS and PSP analyses in SpectreRF) of Fig. 2.1, with NMOS transistors as the switches. We choose transistor dimensions such that $R_{sw} = 5\Omega$, and choose $R_a = 50\Omega$, C_L=200pF, f_{LO} = 100MHz, and $f_{RF} = f_{LO}$ + 1 kHz. As can be seen in Fig. 2.4, sweeping R_B from 10Ω to 100kΩ and applying (2.11) analytically predicts numerical, periodic steady-state simulations with high accuracy. The resulting curve shows that for very high values

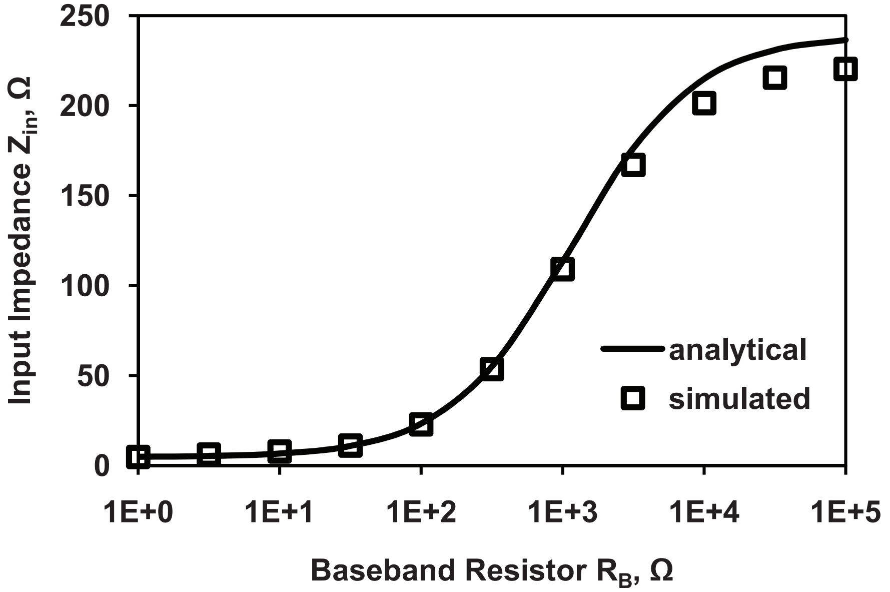

Figure 2.4: Simulated and analytical equivalent input impedance R_{in} vs swept baseband resistor R_B

of R_B, the effective R_{in} converges to near R_{sh}, and that for very low values of R_B, R_{in} converges to R_{sw}. The difference in the two curves for large R_B values is due to the parasitic shunt capacitance present on the antenna side of the switch, which changes the effective R'_a (and therefore R_{sh}) as the RF frequency increases. The effects of a frequency-dependent R_a will be examined in sections 2.3 and 2.5.

The limits in (2.12) imply that an impedance match, where $R_{in} = R_a$, can be achieved provided that $R_{sw} < R_a$ and $R_{sh} > R_a - R_{sw}$. As we will show, maintaining switch resistance such that $R_{sw} \ll R_a$ is also desirable from a noise perspective, and can usually be achieved in a modern process. Equation (2.11) implies that when antenna impedance R_a is treated as constant and real, and $R_{sh} > R'_a$, an impedance match can always be achieved by choosing R_B such that:

$$R_B = \frac{1}{\gamma} \frac{R_{sh}R_a - R_{sw}R_{sh}}{R_{sw} + R_{sh} - R'_a} \tag{2.13}$$

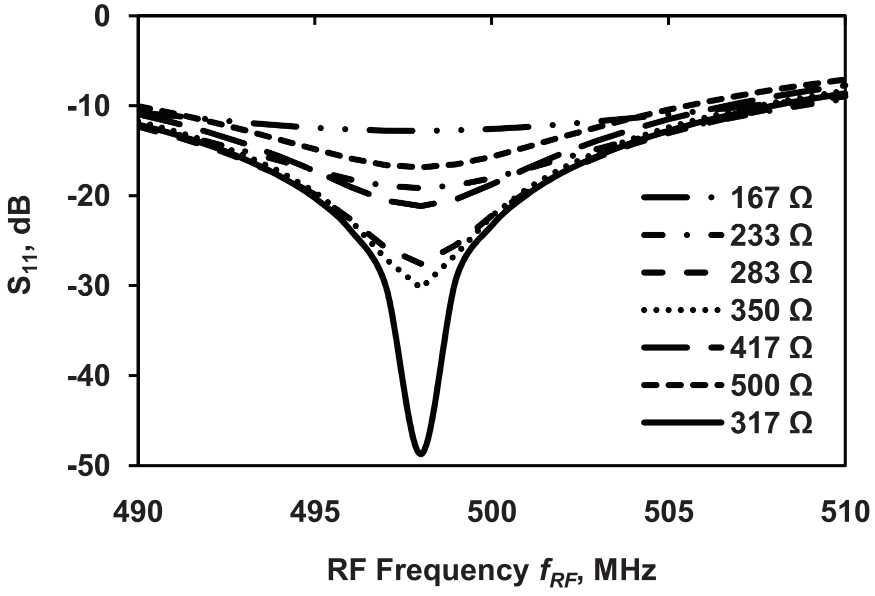

Figure 2.5: Simulated S_{11} for varying R_B

We have confirmed the impedance matching ability of the circuit in Fig. 2.1 with periodic S-parameter analysis for swept R_B. Here we have chosen f_{LO} = 500MHz and C_L = 50pF, with other circuit parameters the same as in Fig. 2.4. Figure 2.5 shows that a real RF impedance match with S_{11} <-45dB can be achieved through passive mixer directly connected to the antenna port.

There are two additional features to notice about Fig. 2.5. The first is that the match is fairly narrowband. We will show in section 2.3.2. that the shape of this match as a function of ω_{IF} is in fact determined by the capacitor C_L. The second is that the center frequency of the match is slightly shifted from the LO. We will show in section 2.5 that this offset is due to complex antenna impedance, and demonstrate a method by which the location of this optimal match can be controlled.

2.3 Effects of Frequency Dependent Components

2.3.1 Accounting for harmonic down-conversion

In the previous section, we defined the up-converted voltage V_x only at the fundamental of the LO, or ω_{LO}. However, its stair-step nature seen in Fig. 2.2 indicates that V_x contains odd harmonics of the LO as well as its fundamental. These harmonics in V_x come from the up-sampling and superposition of the four baseband signals. We now analyze the effect of these harmonics on matching. We start by describing V_x in terms of its Fourier series:

$$V_x(t) = \sum_{n=1,3,5...}^{\infty} V_{x,n}(t) \tag{2.14}$$

With the n-th harmonic, $V_{x,n}$ taking the form

$$\begin{aligned} V_{x,n}(t) \quad &= \quad \frac{4}{n\pi}((V_I \cos(n\omega_{LO}t)\sin(\frac{n\pi}{4}) \\ &\quad +V_Q \sin(n\omega_{LO}t)\cos(\frac{n\pi}{4})) \end{aligned} \tag{2.15}$$

Here we define the baseband voltages $V_I = (V_{C,0} - V_{C,2})/2$, and $V_Q = (V_{C,1} - V_{C,3})/2$. Since n is odd, the trailing $\sin(n\pi/4)$ and $cos(n\pi/4)$ terms always have a magnitude of $1/\sqrt{2}$ but change sign with harmonic number.

The presence of odd harmonics in V_x indicates that current flowing through the antenna impedance must also contain these harmonics. Because antennas generally do not present a constant impedance across frequency, we treat impedance as being different at each harmonic of the LO, and so define a distinct antenna resistance at each harmonic: $R'_a(n\omega_{LO})$. Note that for simplicity, we are assuming that $R'_a(n\omega_{LO})$ is a real impedance, a description for complex antenna impedance will be provided in section 2.5. After once again combining the switch resistance and antenna resistance we define a new $R'_a(n\omega_{LO})$:

$$R'_a(n\omega_{LO}) = R_a(n\omega_{LO}) + R_{sw} \tag{2.16}$$

The current flowing through the switches can now be defined as:

$$I_A(t) = \frac{V_{RF}(t)}{R'_a(\omega_{LO})} - \sum_{n=1,3,5...}^{\infty} \frac{V_{x,n}(t)}{R'_a(n\omega_{LO})} \tag{2.17}$$

The first term represents the current coming from the antenna through the series R'_a and the second term represents the return current due to V_x. Translating these currents back to baseband, we can once again balance charge flow into and out of each baseband capacitor for each LO cycle.

$$Q_m = \frac{V_{C,m}T_{LO}}{R_B} = \int\limits_{m\frac{T_{LO}}{4}}^{(m+1)\frac{T_{LO}}{4}-\frac{T_{LO}}{8}} I_A dt \tag{2.18}$$
$$m = 0, 1, 2, 3$$

Substituting in (2.15) and (2.17) and solving the integral and noting that $V_{c0} = -V_{c2} = V_I$ and $V_{c1} = -V_{c3} = V_Q$, we find:

$$\begin{aligned} V_{x,1}(t)\left(\frac{1}{R_B} + \frac{2}{\pi^2 R'_a(\omega_{LO})} + \sum_{n=1,3,5...}^{\infty} \frac{2}{n_2\pi^2 R'_a(\omega_{LO})}\right) \\ = \frac{2}{\pi^2 R'_a(\omega_{LO})} V_{RF}(t) \end{aligned} \tag{2.19}$$

For comparison, we apply Kirchoff's current law to the V_x node of Fig. 2.3, yields a similar equation:

$$\begin{aligned} V_{x,1}(t)\left(\frac{1}{R_B} + \frac{\gamma}{Ra(\omega_{LO})} + \frac{\gamma}{R_{sh}}\right) \\ = \frac{\gamma}{R'_a(\omega_{LO})} V_{RF}(t) \end{aligned} \tag{2.20}$$

These two equations are equivalent provided that

$$\begin{aligned} R_{sh} &= \left(\sum_{n=3,5...}^{\infty} \frac{1}{n^2 R'_a(n\omega_{LO})}\right)^{-1} \\ &= \left(\sum_{n=3,5...}^{\infty} \frac{1}{n^2} \frac{1}{R_a(n\omega_{LO}) + R_{sw}}\right)^{-1} \end{aligned} \tag{2.21}$$

Thus, we see that in the general case, R_{sh} depends upon the antenna impedance at each of the odd harmonics of the LO frequency, and represents the dissipation and/or reradiation of power due to these harmonics. If we remove the frequency dependence of R_a and perform the summation we find that this impedance is actually equal to the R_{sh} found using the charge balance method in section 2.2. This confirms that the virtual resistance R_{sh} which is used in the LTI model (Fig. 2.3) actually represents the loss due to harmonic re-upconversion and dissipation.

$$\begin{aligned} R_{sh} &= \left(\sum_{n=1,3,5...}^{\infty} \frac{1}{n^2} \frac{1}{R_a + R_{sw}} \right)^{-1} \\ &= \left((\frac{\pi^2}{8} - 1) \frac{1}{R_a + R_{sw}} \right)^{-1} \\ &= R'_a \frac{4\gamma}{1 - 4\gamma} \end{aligned} \tag{2.22}$$

2.3.2 Impedance as a function of varying IF

So far, we have made several assumptions in order generate a simple model for impedance matching. We assumed that $\omega_{IF} \rightarrow 0$, and so did not take into account the effect of the sampling capacitor C_L from Fig. 2.1 on the impedance seen at the antenna port. In this section we will remove the zero-IF requirement and show the effect of the baseband capacitor C_L as the input frequency varies around a constant LO.

We begin by modifying the input tone (2.2) to incorporate a baseband frequency ω_{IF}, such that $\omega_{RF} = \omega_{LO} + \omega_{IF}$ (where ω_{IF} can be either positive or negative), and reformulate time as $t = kT_{LO} + \tau$ so as to separate time within a given LO cycle (τ) from slow changing effects across LO cycles introduced by ω_{IF}.

$$V_{RF}(t) = A\cos((\omega_{LO} + \omega_{IF})(kT_{LO} + \tau)) \tag{2.23}$$

We then incorporate this new V_{RF} into the charge balance equation (2.3):

$$\begin{aligned} Q_m &= \frac{V_{C,m}T_{LO}}{Z_B} \qquad (2.24)\\ &= \int_{kT_{LO}+m\frac{T_{LO}}{4}-\frac{T_{LO}}{8}}^{kT_{LO}+(m+1)\frac{T_{LO}}{4}-\frac{T_{LO}}{8}} \frac{V_{RF}-V_{C,m}}{R'_a}dt \end{aligned}$$

$$m = 0, 1, 2, 3$$

Note that the load present at the baseband is now Z_B, which will vary in frequency as a function of ω_{IF}, and can be written as:

$$Z_B(\omega_{IF}) = R_B||(j\omega_{IF}C_L) = \frac{R_B}{1 + j\omega_{IF}C_LR_B} \qquad (2.25)$$

After performing the integral, moving R'_a to the left side and evaluating at the limits, we compute a $V_{C,m}$ which is very similar to (2.4), with the arbitrary phase shift now becoming $\omega_{IF}kT_{LO}$.

$$\begin{aligned} V_{C,m} = \frac{4}{\pi}\frac{Z_B}{Z_B+4R'_a}\frac{\omega_{LO}}{\omega_{RF}}A\sin(\frac{\pi}{4}+\omega_{IF}\frac{T_{LO}}{8}) \\ \cos(\omega_{IF}kT_{LO}+\omega_{IF}\frac{mT_{LO}}{4}+\frac{m\pi}{2}) \qquad (2.26) \end{aligned}$$

Which, provided that $\omega_{IF} \ll \omega_{LO}$ implies

$$V_{C,m} = \frac{2\sqrt{2}}{\pi}\frac{Z_B}{Z_B+4R'_a}A\cos(\omega_{IF}T_{LO}(k+\frac{m}{4})+\frac{m\pi}{2}) \qquad (2.27)$$

Discretized over one quarter period of the LO, the term $T_{LO}(k+m/4)$ equals t. Using this fact and extracting the up-converted $V_x(\omega_{RF})$, we find an expression becomes essentially identical to (2.6).

$$V_x(\omega_{RF}) = V_{RF}(\omega_{RF})\frac{8}{\pi^2}\frac{Z_B}{Z_B+4R'_a} \qquad (2.28)$$

This then produces the same derivation of the current I_A as shown above.

If we now re-introduce the LTI model with a simple transformation from γR_B to γZ_B (see Fig. 2.6), we can rewrite the expression for impedance seen by the antenna (2.11),

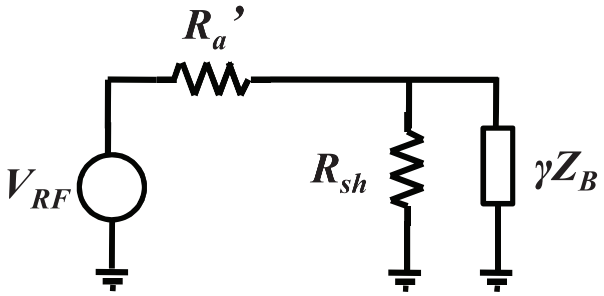

Figure 2.6: New LTI equivalent circuit for frequency dependent Z_B

including the frequency-dependent Z_B.

$$\begin{aligned} Z_{in}(\omega_{IF}) &= R_{sw} + \gamma Z_B(\omega_{IF})||R_{sh} \\ &= R_{sw} + \frac{\gamma R_B||R_{sh}}{1 + j\omega_{IF}C_L(\gamma R_B||R_{sh})} \end{aligned} \tag{2.29}$$

Figure 2.7 shows the effective real and imaginary components of the impedance seen at IF and at RF due to the frequency dependent components. The presence of the baseband capacitor C_L has two notable effects on the tunable impedance presented to the antenna port. First, because the capacitor shunts high frequency IF signals on the baseband port, it creates a band pass filter. As a result, the effect of tuning R_B on the impedance match diminishes for larger baseband frequencies as Z_{in} becomes dominated by C_L and ultimately approaches R_{sw} for larger offset frequencies. The presence of this band pass filter has been shown to contribute to the attenuation of out-of-band blockers resulting in measurements of IIP3 > 25dBm [12, 18]. Second, the imaginary component of Z_{in} looks negative for positive ω_{IF} and positive for negative ω_{IF}. This means that for a negative IF, the antenna port sees a complex conjugate of the impedance presented by the baseband. Meanwhile, the asymmetric imaginary component of Z_{in} accounts for the frequency offset of the ideal match in Fig. 2.5. This imaginary component is interacting with the capacitive parasitics on the RF port of the mixer, such that an ideal complex

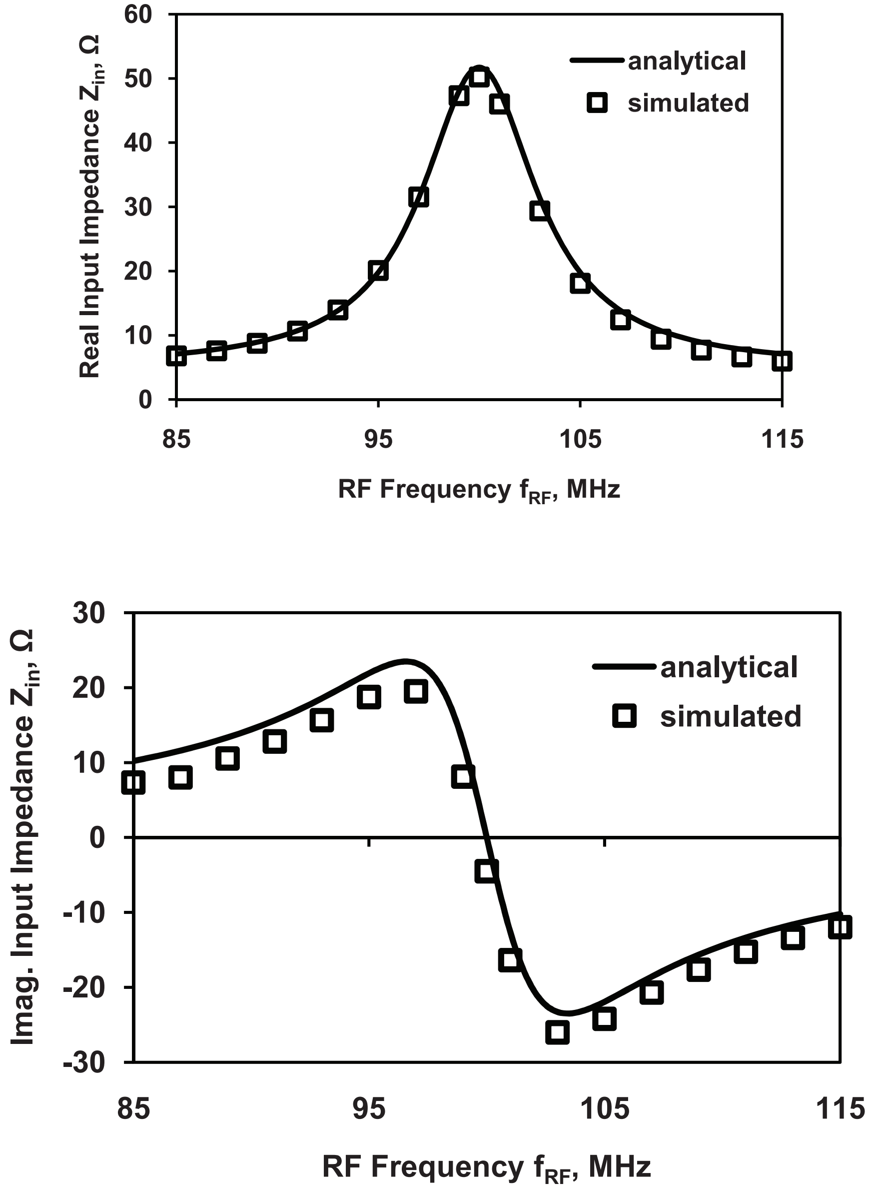

Figure 2.7: Effective real and imaginary components of Z_{in} as a function of RF frequency

conjugate match occurs at a slight frequency offset from the LO.

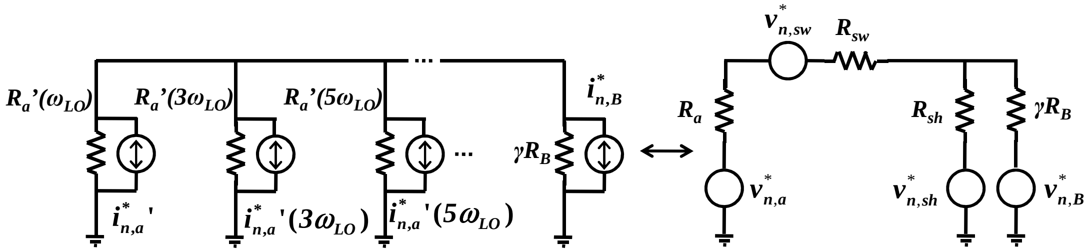

Figure 2.8: Equivalent noise models for LTI model from Fig. 2.3

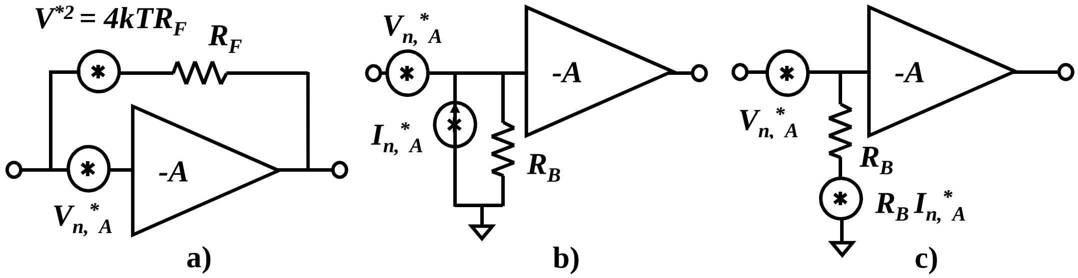

Figure 2.9: Equivalent baseband amplifier noise models

2.4 Noise Performance

2.4.1 Noise Performance of Passive Mixer

The time-invariant model in Fig. 2.3 also simplifies the calculation of the noise contributions for the mixer. To see this, we first need to look at the various sources of noise in the circuit shown in Fig. 2.1. There are three fundamental sources of noise: the baseband resistance R_B, the switch resistance, R_{sw}, and the thermal noise from the antenna itself, R_a. As before, we can safely merge the antenna and switch resistance into a single resistor, R_a'. To find the total noise, we compute the total noise current injected into the baseband node, and multiply this with the total impedance at that node. Thus, if R_B is a real resistor, this current will be: $i^{*2}_{n,b} = 4kT/\gamma R_B$.

Similarly the noise from R'_a is $i^{*2}_{n,a'} = 4kT/R'_a$. However, to be complete, this noise must also include noise down-converted by the mixer at odd harmonics of the LO, such that $i^{*2}_{n,a'}(n\omega_{LO}) = 4kT/n^2R'_a(n\omega_{LO})$. The schematic on the left side of Fig. 2.8 shows this model. However, we note that the sum of the antenna noise currents $i^{*2}_{n,a'}(n\omega_{LO})$ for n =3,5,7 etc. is exactly the noise that would be generated by R_{sh} if it was a real resistor. Therefore we can use the two noise models in Fig. 2.8 interchangeably. The total noise voltage is the sum of the thermal voltage sources corresponding to each resistor in the circuit. The noise factor for this circuit is found by dividing the total output noise by the portion of that noise caused by the input noise of R_a.

$$\begin{aligned} F &= 1 + \frac{v^{*2}_{n,sw}}{v^{*2}_{n,a}} + \frac{v^{*2}_{n,sh}}{v^{*2}_{n,a}}\left(\frac{R_a + R_{sw}}{R_{sh}}\right)^2 \\ &\quad + \frac{v^{*2}_{n,B}}{v^{*2}_{n,a}}\left(\frac{R_a + R_{sw}}{\gamma Z_B}\right)^2 \end{aligned} \tag{2.30}$$

If we assume impedance matching to 50Ω and a switch resistance of 5Ω, this results in $NF = 3.88dB$. Note that this noise is dominated by contributions from the baseband resistor R_B and includes no noise from subsequent amplifiers. In the next section we will demonstrate how this noise contribution can be minimized in the implementation of an actual receiver using the passive mixer-first architecture.

2.4.2 Receiver Architecture

In order to add gain to the receiver and to improve its noise figure, all while maintaining the impedance matching functionality through the passive mixer, we have proposed the receiver architecture shown in Fig. 2.10 [12]. This receiver consists of a passive quadrature mixer, followed by baseband amplifiers in resistive feedback.

We find the new effective R_B present on each branch by applying the Miller effect to

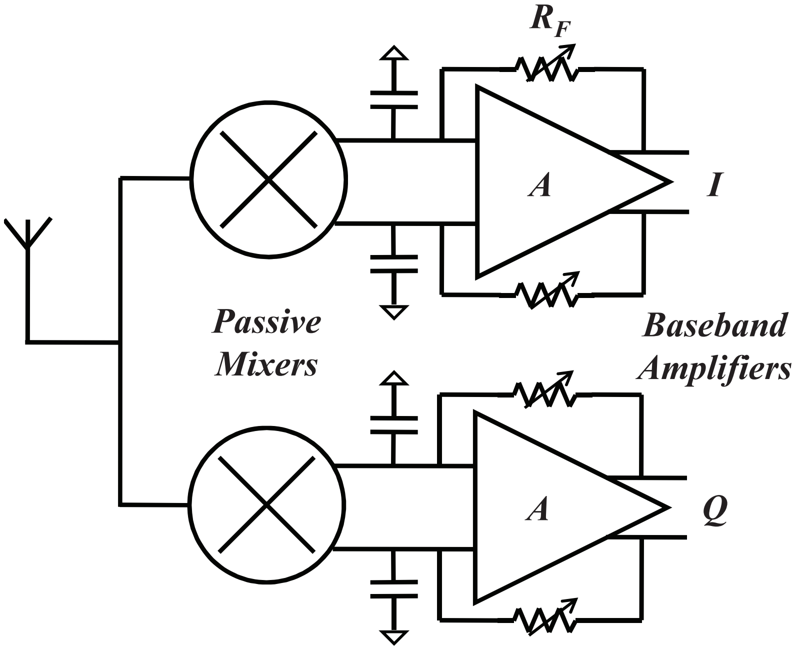

Figure 2.10: Proposed passive-mixer first receiver with resistive feedback amplifiers

the feedback resistor R_{FR}:

$$R_B = \frac{R_{FR}}{1 + A} \tag{2.31}$$

Substituting the new R_B into the impedance matching LTI model shows that we can perform impedance matching using the amplifier feedback resistors.

Once we have added the feedback amplifiers to implement R_B, the noise performance changes as well. Whereas most of the noise sources in (2.30) can be treated as standard resistive thermal noise, the baseband noise is now due to the feedback resistor and the input referred noise of the amplifier itself (Fig. 2.9a). This noise is traditionally modeled by a pair of correlated noise sources: a series voltage and shunt current (Fig. 2.9b). This is equivalent to two voltage sources, as shown on the right of Fig. 2.9c:

These two sources both depend upon the input referred voltage noise of the amplifier, and so are correlated. However, the source present in shunt also depends upon the feedback resistor and amplifier gain, and can be computed to be

$$i_{n,A}^{*2} R_B^2 = \left(\frac{4kTR_{FR}}{(A+1)^2} + \frac{\overline{v}_{n,A}^{*2}}{(A+1)^2} \right) \tag{2.32}$$

Substituting the equation for thermal noise and (2.32) into (2.30), and accounting for γ both in the baseband noise (by multiplying the squared noise by γ) and in the baseband resistance (by multiplying R_B by γ), yields the following noise factor:

$$\begin{aligned} F = {} & 1 + \frac{R_{sw}}{R_a} + \frac{R_{sh}}{R_a} \left(\frac{R_a + R_{sw}}{R_{sh}} \right)^2 \\ & + \gamma \frac{R_{FR}}{R_a} \left(\frac{R_a + R_{sw}}{\gamma R_{FR}} \right)^2 \\ & + \gamma \frac{\overline{v}_{n,A}^{*2}}{4kTR_a} \left(\frac{R_a + R_{sw}}{\gamma R_{FR}} + \frac{R_a + R_{sw} + R_{sh}}{R_{sh}} \right)^2 \end{aligned} \tag{2.33}$$

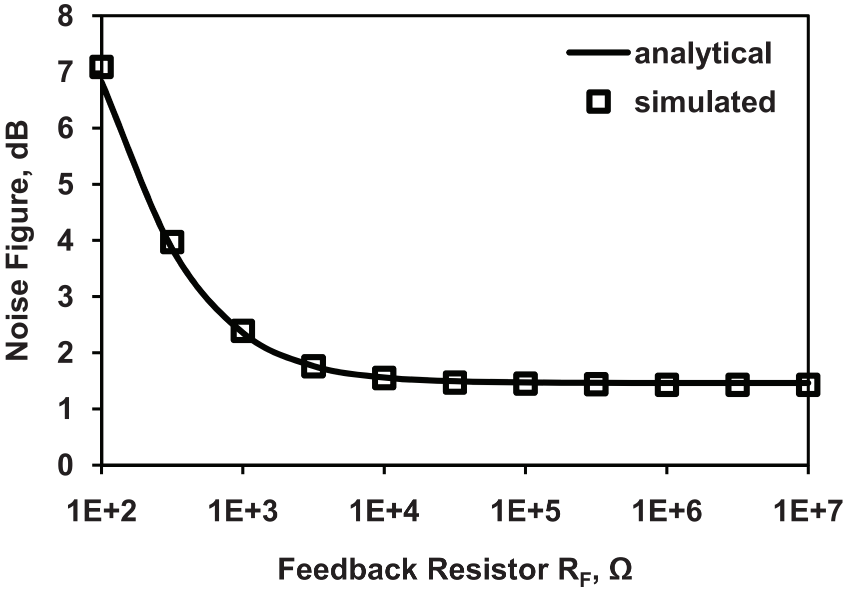

Figure 2.11: Simulated and analytical noise figure vs feedback resistor R_{FR}

We have verified this relationship (see Fig. 2.11) with simulation using periodic steady state analysis in SpectreRF, with f_{LO} = 100MHz, A=30, $v_{n,A}^* = 400pV/\sqrt{Hz}$, and the same device parameters as in Fig. 2.4. The simulation results match analytical predictions well.

By making baseband gain A (and so R_{FR}) large, and biasing the amplifier with sufficient current to make $\overline{v}^{*2}_{n,A}$ small, the latter terms can be made small. Furthermore, by choosing transistor dimensions such that the switch resistance and therefore its noise are small relative to R_a, we find a limit on the noise factor which depends on R_{sh}:

$$F > 1 + \frac{R_a}{R_{sh}} \tag{2.34}$$

For constant $R'_a(\omega)$, where (2.10) holds, (2.34) implies that $F > 1.23$, or $NF = 0.91dB$. In cases where antenna impedance decreases with frequency, this limit is degraded. More generally, Provided that $R_{sh} \gg R_a$, $R_{sw} \ll R_a$, and $R_{FR} \gg R_a$, all of these terms will be much less than one except the final term which also depends upon amplifier noise. Under these conditions, the baseband amplifier can be expected to limit noise figure. Indeed, amplifier noise has been reported as the dominant noise source in existing work [8, 9, 12].

It is worth noting, however, that the effect of baseband amplifier noise is also dependent on the value of R_{sh}, and will degrade strongly as R_{sh} is made small. The effect of R_{sh} on both the impedance matching range and NF of passive mixers shows that neglecting the effects of re-upconversion of baseband signals to higher harmonics (as was done in [11]) will result in an inaccurate model.

2.5 Complex Antenna Impedance

2.5.1 Effects of Complex Antenna Impedance

Thus far, the model we have presented assumes a purely real antenna impedance. We will now expand this treatment to incorporate a complex antenna impedance $Z_a(\omega)$. Such a complex impedance can appear either directly on the antenna as it is used across wide frequency ranges, and also through bond wires, pads, and parasitic capacitances on the switches themselves.

By performing the analysis is section 2.2 again, except with the inclusion of $Z'_a = Z_a(\omega_{LO}) + R_{sw}$, we find a new model which is very similar to the previous one except with the replacement of R_a with Z_a. This means that the harmonic shunting impedance will also be complex, so we rename it Z_{sh}. Z_{sh} can be computed as above in (18)-(21), but including phase shifts in the current due to the harmonics of V_x. Because the effects of these phase shifts depend upon which harmonic is being shifted, this calculation results in a Z_{sh} which incorporates Z_a for the 5th, 9th, 13th, etc. harmonic of ω_{LO} and the complex conjugate of Z_a (Z_a^*) for the 3rd, 7th, 11th, etc.

$$\begin{aligned} Z_{sh}(n\omega_{LO}) = (&\sum_{n=3,7,11\ldots}^{\infty} \frac{1}{n^2 Z_a'^*(n\omega_{LO})} \\ &+ \sum_{n=5,9,13\ldots}^{\infty} \frac{1}{n^2 Z'_a(n\omega_{LO})})^{-1} \end{aligned} \tag{2.35}$$

Using these, we can rewrite the expression for Z_{in} similar to that derived from Fig. 2.3.

$$Z_{in} = R_{sw} + \gamma Z_B || Z_{sh} \tag{2.36}$$

We confirmed the analysis leading to (2.29) with numerical simulations, using the same model as in Fig. 2.4, and sweeping LO frequency, but with 300fF of parasitic capacitance on the RF port of the mixer (in parallel with 150fF parasitic capacitance from the

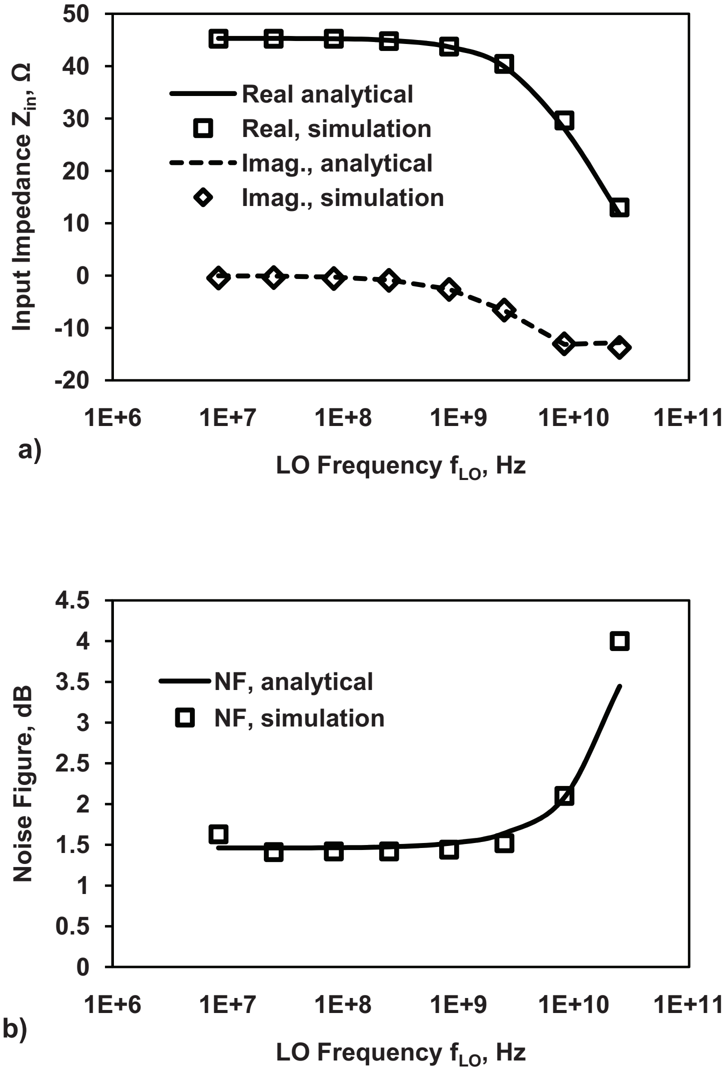

Figure 2.12: Comparison of analytical and simulated receiver a) input impedance, and b) noise figure vs frequency, accounting for frequency dependent antenna impedance.

switch transistors themselves) and setting $R_{FR} = 2660\Omega$. As can be seen in Fig. 2.12, this demonstrates close agreement between analysis and simulation. Additionally, we

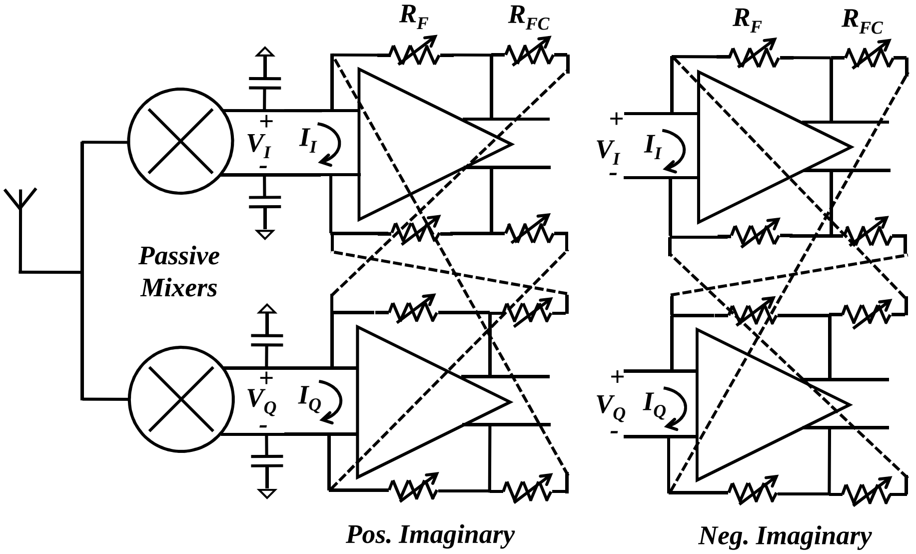

Figure 2.13: Positive and negative complex feedback applied to the baseband amplifier

may write an expression for noise factor similar to (2.33):

$$
\begin{aligned}
F = 1 &+ \frac{R_{sw}}{\mathrm{Re}(R_a)} + \frac{\mathrm{Re}(Z_{sh})}{\mathrm{Re}(Z_a)} \left| \frac{Z_a + R_{sw}}{Z_{sh}} \right|^2 \\
&+ \frac{\gamma R_{FR}}{\mathrm{Re}(Z_a)} \left| \frac{Z_a + R_{sw}}{\gamma R_{FR}} \right|^2 \\
&+ \frac{\gamma \overline{v}^{*2}_{n,A}}{4kT\mathrm{Re}(Z_a)} \left| \frac{Z_a + R_{sw}}{\gamma R_{FR}} + \frac{Z_a + R_{sw} + R_{sh}}{R_{sh}} \right|^2
\end{aligned}
\tag{2.37}
$$

2.5.2 Matching to a complex antenna impedance: Complex Feedback

In this formulation, the antenna impedance and shunt impedance can both take on complex values, and a complex conjugate match will only be achieved if the complex component of Z_B is tunable. With the architecture described so far, making the capacitor C_L

tunable would provide this, but only as a negative reactance, and would also strongly affect the bandwidth of the match. Instead, in order to introduce the complex term in the context of the circuit shown in Fig. 2.1, we can modify the original baseband amplifiers by applying additional feedback resistors from the I to the Q channel and the Q to the I channel as shown in Fig. 2.13. A similar feedback technique is utilized in [19] but was used to modify the phase of a filter rather than to present a complex impedance to the input.

In order to analyze this circuit, we will begin with a simple case where we define the signal coming from the antenna as:

$$V_{RF}(t) = \cos(\omega_{LO} t). \tag{2.38}$$

When this signal is down-converted through the I and Q paths of the mixer, assuming the two paths are perfectly balanced, we should get:

$$\begin{aligned} V_I &= 1 \\ V_Q &= 0 \end{aligned} \tag{2.39}$$

We then look at the amplitude of the current present at the inputs of the amplifiers due to the new cross-connected feedback resistors we see:

$$\begin{aligned} I_I &= \frac{V_I(1+A)}{R_{FR}} + \frac{V_I}{R_{FC}} \\ I_Q &= \frac{V_I A}{R_{FC}} \end{aligned} \tag{2.40}$$

Equation (2.40) shows that the cross-channel feedback connections introduce a scaled 90° out of phase component of V_{RF} back to the input. When these currents are back upconverted to the antenna port, we find

$$\begin{aligned} I_{RF} &= I_I \cos(\omega_{LO} t) + I_Q \sin(\omega_{LO} t) \\ &= \left(\frac{V_I(1+A)}{R_{FR}} + \frac{V_I}{R_{FC}} \right) \cos(\omega_{LO} t) \\ &\quad + \frac{V_I A}{R_{FC}} \sin(\omega_{LO} t) \end{aligned} \tag{2.41}$$

Using (2.41) we may write an expression for the effective complex baseband impedance, Z_B, where the sign of the imaginary term depends on whether the feedback is connected in positive or negative complex feedback (see Fig. 2.13) :

$$Z_B = \left[\left(\frac{1+A}{R_{FR}} + \frac{1}{R_{FC}}\right) \pm j\frac{A}{R_{FC}}\right]^{-1}. \tag{2.42}$$

Note that if we repeat this analysis for the case where $V_{RF} = \sin(\omega_{LO}t)$, we find that because of the relative phases of sin and cos, we actually need to flip the polarity of the feedback resistors from the Q channel to the I channel, in order to get the same equivalent complex phase shift. This result is seen in the schematic in Fig. 2.13.

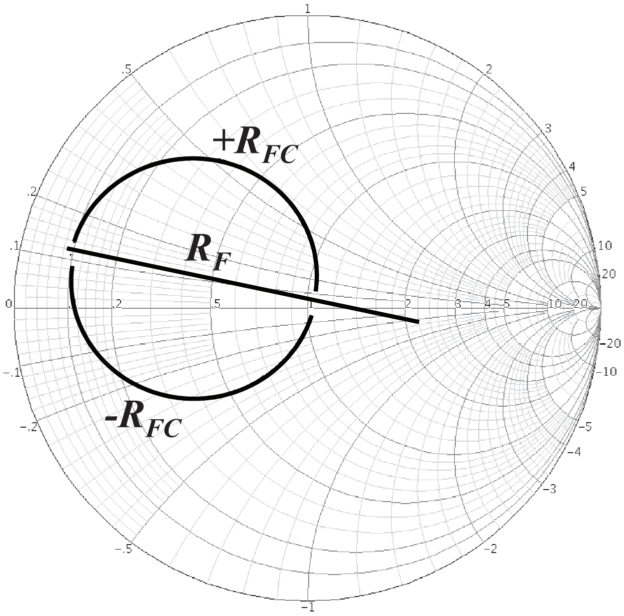

Figure 2.14: Simulated S_{11} Smith chart for varying $\pm R_{FC}$

Using a similar simulation setup to Fig. 2.5, Fig. 2.14 shows an S_{11} Smith-chart of the sweeps of both the real feedback resistor R_{FR} and the complex feedback resistor R_{FC}. This figure demonstrates the distinct complex nature of the impedance presented to the antenna port using complex feedback. The sweep using R_{FR} alone shows some complex impedance due to the parasitic capacitances present on the switches.

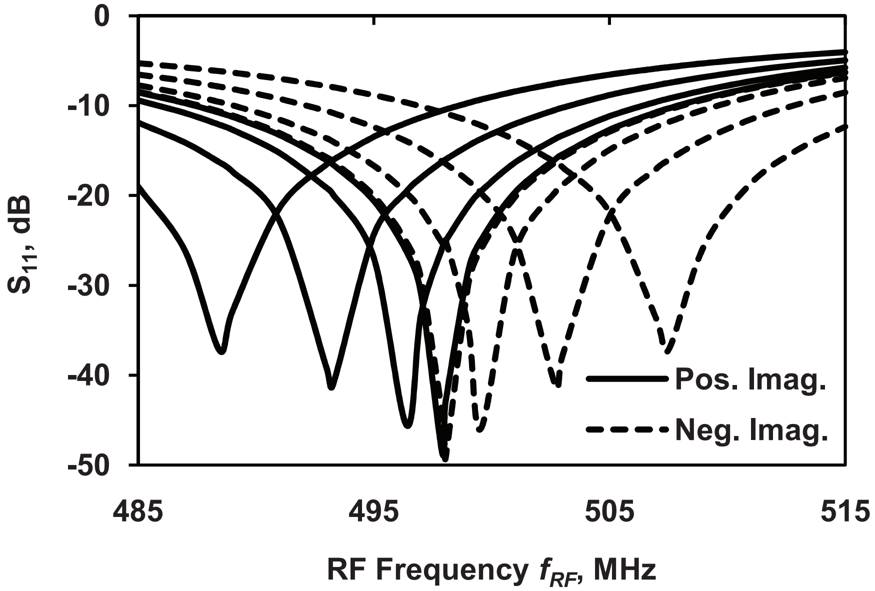

Figure 2.15: Simulated S_{11} for varying $\pm R_{FC}$ showing shift in center frequency of optimal match

Fig. 2.15 shows an S_{11} plot of sweeps of frequency for varying complex feedback resistor R_{FC}. Here we have chosen the value of R_{FR} from Fig. 2.5 which provided the best match to $R_a = 50\Omega$. However as we noted earlier, this match was narrowband and centered around 497 MHz. Figure 2.15 shows that complex feedback can change this center frequency to either side of the LO by interacting with the imaginary component of the antenna impedance and of the baseband capacitors. Each curve is for a different value of R_{FC}, with smaller resistors pushing the center frequency further from the LO.

2.6 Limitations of 4-phase Mixing and Benefits of more LO phases

2.6.1 Implications of Z_{sh}

One implication of (2.11), (2.29), and (2.36) is that in order to maximize impedance tuning range and minimize noise figure, it is desirable to maximize Z_{sh}. Equation (2.35) in turn shows that maximizing Z_{sh} requires maximizing the impedance presented to the RF port of the mixer at higher harmonics of the LO frequency. Note that this is exactly the opposite result from that typically created by simple resonant matching networks, where shunting parasitic capacitance reduces impedance at higher frequencies, and a resonant network maximizes impedance at the fundamental [8].

Another implication is that noise figure is not necessarily minimized by simply reducing switch resistance. Since parasitic capacitance on the mixer input acts to shunt Z_a, driving $Z_a(\omega) \to 0$, and therefore $Z'_a(\omega) \to R_{sw}$ as $\omega \to \infty$. Under this condition reduction in R_{sw} will also act to reduce Z_{sh}. Furthermore, widening the mixer transistors to reduce R_{sw} will also increase the parasitic capacitance on the mixer input, further reducing Z_{sh}. Thus, it is expected that intermediate width mixer devices with small but finite switch resistance will provide optimal noise, especially under resonant match. This can be analyzed for the extreme case of a very high-Q antenna with impedance R_a near ω_{LO}, but zero at harmonics of ω_{LO}. In this case, $R_{sh} = 4.3R_{sw}$, and so

$$NF = 1 + \frac{R_{sw}}{R_a} + \frac{(R_a + R_{sw})^2(1 - 4\gamma)}{4\gamma R_a R_{sw}} \tag{2.43}$$

(neglecting baseband noise entirely). The NF is minimum when

$$R_{sw} = R_a\sqrt{1 - 4\gamma} \Rightarrow NF \geq 4.05dB \tag{2.44}$$

No matter how high an impedance is achieved by a high-Q resonant match, NF will always be worse than 3 dB, whereas a wider band match can actually provide lower NF.

2.6.2 Enhancements due to multi-phase mixers

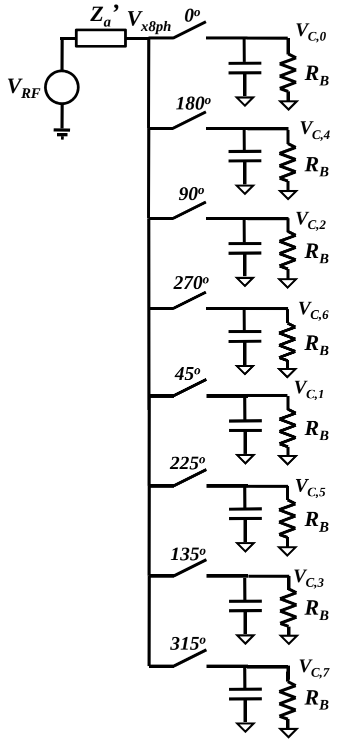

Figure 2.16: Eight-phase passive mixer

It is clear that performance improves as Z_{sh} is increased, and as (2.35) shows, Z_{sh} can be considered to be a parallel combination of the antenna and switch impedance computed at each of the odd harmonics of the LO, weighted by the harmonic number. This harmonic impedance dependence is a consequence of the harmonic content of the virtual voltage $V_x(t)$. For the switching waveforms in Fig. 2.2, $V_x(t)$ contains all of the odd harmonics of ω_{LO}, weighted by one over the harmonic number, and so dissipates or reradiates power at all of these frequencies. This indicates that if an alternate mixer structure was chosen which provided for a less harmonic rich V_x, reradiation would be reduced, and consequently Z_{sh} made larger. One such structure is the 8-phase passive mixer shown in Fig. 2.16, driven by 8 non-overlapping LO signals similar in concept to "harmonic suppression mixers" recently discussed in the literature [12, 13, 18, 20].

Using such a mixer and the definition of V_{RF} from (2.2), we can compute that the four differential outputs will take the form:

$$\begin{aligned}
V_{C,0} - V_{C,4} &= GA(t)\cos(\phi(t) + \theta) \\
V_{C,1} - V_{C,5} &= GA(t)\cos(\phi(t) + \theta - \pi/4) \\
&= \frac{GA(t)}{\sqrt{2}}(\sin(\phi(t) + \theta) + \cos(\phi(t) + \theta) \\
V_{C,2} - V_{C,6} &= GA(t)\cos(\phi(t) + \theta - \pi/2) \\
&= GA(t)(\sin(\phi(t) + \theta) \\
V_{C,3} - V_{C,7} &= GA(t)\cos(\phi(t) + \theta - 3\pi/4) \\
&= \frac{GA(t)}{\sqrt{2}}(\sin(\phi(t) + \theta) - \cos(\phi(t) + \theta)
\end{aligned} \tag{2.45}$$

where the constants G and θ are introduced to account for the effects of Z'_a and Z_B. The key point here is that the down sampling of this mixer results in outputs with exactly the relative weights needed for harmonic suppression when back up-converted, without any explicit weighting circuitry. Thus V_{x8ph}, which takes the form shown in Fig. 2.17, has a Fourier series which only contains half of all odd harmonics, driving the terms

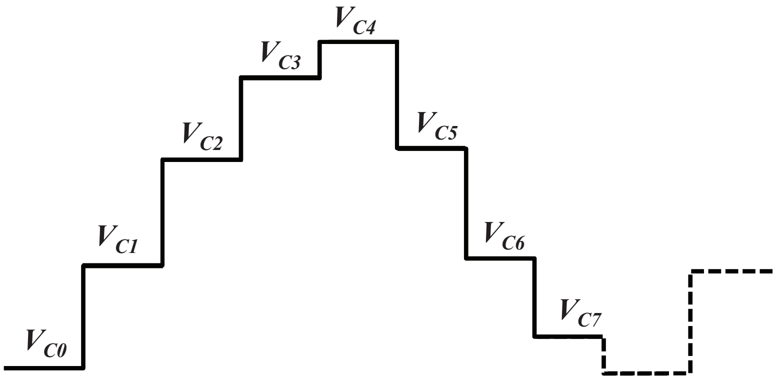

Figure 2.17: Approximation of waveform V_{x8ph} for 8-phase mixer

corresponding to n =3, 5, 11, 13,... to zero.

This reflects in Z_{sh}, which following a derivation similar to (2.35), is

$$Z_{sh}(n\omega_{LO}) = \Big(\sum_{n=7,15...}^{\infty} \frac{1}{n^2 Z_a'^*(n\omega_{LO})} + \sum_{n=9,17...}^{\infty} \frac{1}{n^2 Z_a'(n\omega_{LO})} \Big)^{-1} \tag{2.46}$$

Once again, half of the odd harmonics are eliminated, dramatically increasing Z_{sh}. The complex version of the model in Fig. 2.3 still applies, using this new Z_{sh} and altering the term γ, such that

$$\gamma_{8ph} = \frac{2}{\pi^2}(2 - \sqrt{2}) \approx 0.119 \tag{2.47}$$

Substituting (2.46) and (2.47) into (2.36) and (2.37) allows us to compute input impedance and noise figure. In the case of constant, real antenna resistance, analogous to (2.10), the 8-phase mixer provides a shunting resistance of

$$R_{sh8ph} = R_a' \frac{8\gamma_{8ph}}{1 - 8\gamma_{8ph}} \approx 18.9 R_a' \tag{2.48}$$

This is almost five times larger than the 4-phase case. Furthermore, applying the fundamental limit to NF from (2.34) to the 8-phase case, we find that NF > 0.22 dB for a constant antenna impedance. These results are confirmed by numerical simulation in Fig. 2.18, and show both a much larger input impedance range and lower noise figure for an 8-phase mixer than for a 4-phase mixer. Note that the analytical result for the input impedance in Fig. 2.18a must take into account the parasitic shunt capacitance on the antenna port, even at 100MHz. This is because higher harmonics of the LO now dominate Z_{sh}, and since the capacitor has more effect at these higher frequencies, its contribution to Z_{sh} is greater. For the case of a high-Q match as in (2.43) and (2.44), NF is best when

$$R_{sw} = R_a \sqrt{1 - \frac{16(2 - \sqrt{2})}{\pi^2}} \Rightarrow NF \geq 2dB \tag{2.49}$$

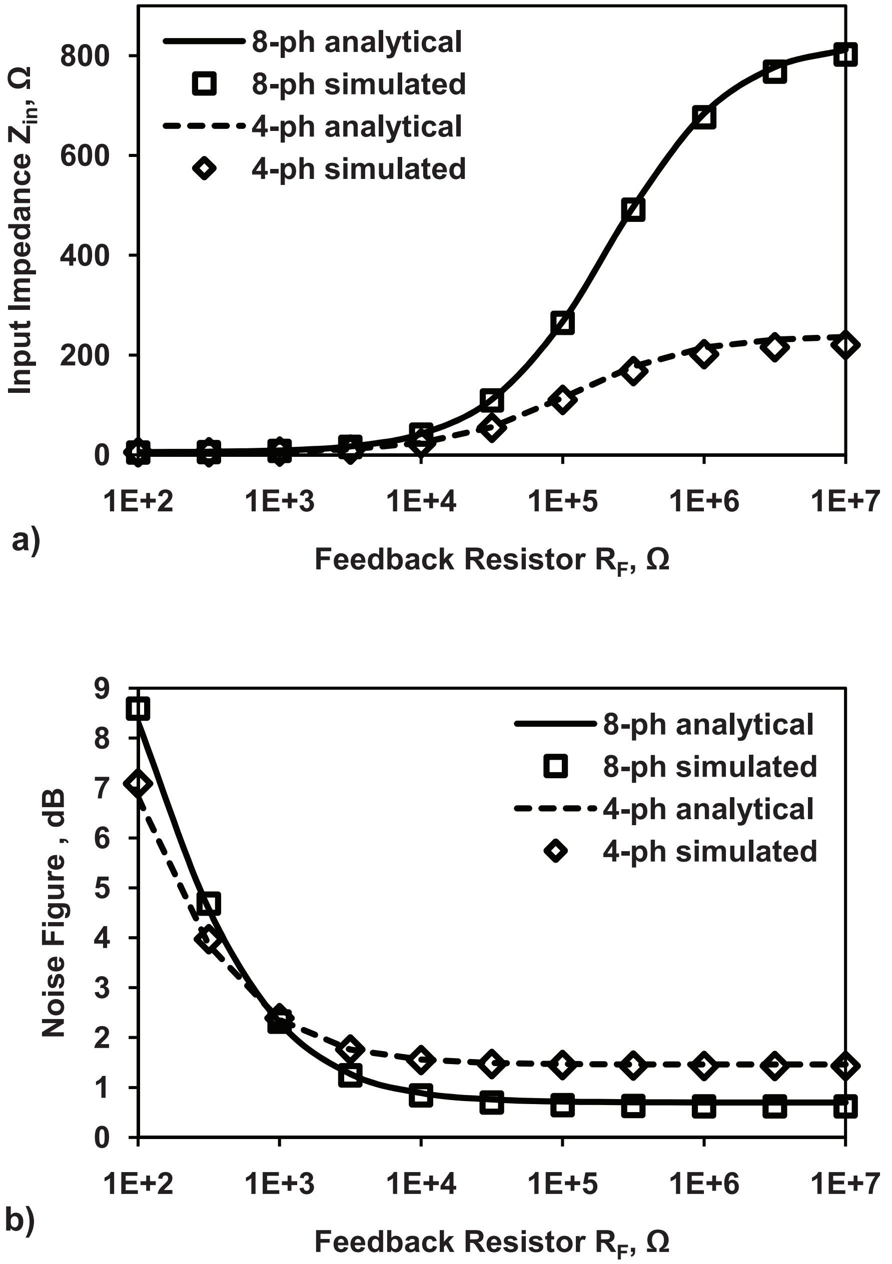

Figure 2.18: Comparison of a) input impedance and b) noise figure between 4-phase and 8-phase mixers

Which implies that even for a high Q match, good NF is possible with eight non-overlapping LO phases.

2.7 Conclusion

The analyses and simulations presented here reveal several important facts about passive mixer-first receivers. The first is that for quadrature passive mixers using non-overlapping clocks, the input impedance at the RF port of the device is strongly sensitive to the impedance presented to the baseband ports of the mixer, and increasing the baseband resistance acts to increase the apparent RF resistance, allowing for baseband-controlled impedance matching. Second, this method can be expanded with baseband feedback between in-phase and quadrature paths to implement a complex conjugate impedance match at the RF port. A third important point is that the degree to which the baseband impedance can influence the RF impedance depends on re-radiation back through the mixer at higher harmonic frequencies. In particular, this results in a shunting effect which in turn depends on the impedance presented to the mixer's RF port at these higher harmonics: lower impedance at harmonic frequencies translates to more shunting. Meanwhile, suppression of these harmonics with appropriate mixer design can reduce this shunting effect significantly, improving performance. What holds for impedance also holds for noise, with noise figure depending on both the antenna and baseband impedance, and with increased harmonic shunting degrading this NF. Finally, we have shown that with appropriate baseband design, the fundamental limit on noise figure in a passive mixer-first receiver is set by this shunting or reradiation effect, and can be lower than 3 dB.

CHAPTER 3

A PASSIVE MIXER-FIRST RECEIVER WITH DIGITALLY CONTROLLED AND WIDELY TUNABLE RF INTERFACE

3.1 Introduction

A software-defined radio (SDR) ideally allows all of the parameters of a radio to be programmed dynamically. In recent years, innovations in both circuit architectures and process technologies have enabled great programmability in bandwidth [21], oscillation frequency [5, 9, 22], gain, and modulation type. However, the antenna interface of receivers, ie. the RF LNA, matching network and RF-band filter (often a SAW filter), remain very hard to tune [1, 2, 23].

Ideally, the antenna interface of an RF receiver should perform three functions: (1) match the impedance of the antenna so as to extract the maximum possible wanted (in-band) signal power from the antenna and prevent reflections, (2) amplify the wanted signal with low noise, and (3) reject unwanted (out-of-band) interferers. However, in the current literature, achieving these goals over wide RF tuning range has proven challenging [5, 22]. The structures currently used to achieve both good impedance matching and low susceptibility to blockers require resonant structures that are inherently highly frequency dependent.

Current solutions for receivers capable of capturing several widely spaced bands either involve multiple, parallel, narrowband front-ends, used one at a time [3, 4, 24, 25], or wideband receivers with only moderate rejection of interference (out-of-band IIP3 of <0dBm) at many bands [5, 22, 26]. The former solution comes at significant cost in area both on chip and off, and the latter simply cannot achieve the necessary performance for many applications (cellular, etc.). The current state of the art does not allow for a high performance, high tuning range SDR.

The architecture of high performance (and therefore) narrowband direct conversion receivers includes (in order of the input signal path) an off-chip RF-band filter, a matching network, LNA, mixer, and baseband circuitry [25, 27]. The components which are difficult to tune across frequency are the ones which see the RF signal, coming before the mixer in the signal path. The RF-band filter rejects out-of-band blockers, and is typically implemented with high-Q off-chip components such as SAW filters. The matching network, typically implemented with a resonant LC network, transfers as much power as possible to the LNA. The LNA absorbs the RF power and provides amplification of the signal with as little noise as possible. Indeed, a good definition of an LNA is an amplifier that provides an impedance match with less than 3dB noise figure (something a simple resistive matching network cannot achieve). Widely tunable receivers reported so far remove the RF-band filter entirely and substitute a wideband but lower performance and higher power matched LNA [5, 22].

In principle, a homodyne (direct conversion) receiver does not require any RF components but a mixer and local oscillator in order to function, and indeed early receivers included only these components [28]. This simple approach has recently garnered more attention, as recent work suggests that connecting the antenna directly to a CMOS *passive* mixer without an RF LNA can provide significant benefits, such as extremely low power [8] or greatly increased tuning range and linearity [9, 12]. Interest has been renewed in passive mixers in LNA-first applications as well, because of their high linearity [10, 11, 14]. The receiver we present here begins with the passive mixer-first approach, eliminating the traditional RF filter, RF matching network, and LNA. Our receiver implements these three components at the baseband, and translates their effects to the antenna using the transparency property of passive mixers [11, 14, 29].

Here we present an expanded description and characterization of the architecture presented in [12], with minor revisions to the implementation to enhance performance (particularly noise). We also confirm some of the theoretical findings in [30] regarding impedance matching and noise performance. Specifically, we confirm in measurement the benefits of 8-phase mixing when implemented in a passive mixer-first receiver architecture. These include a higher impedance matching range, lower NF, and rejection of blockers at the harmonics of the LO.

We will show that our passive mixer-first receiver can achieve (1) S_{11} competitive with highly resonant matching networks while tracking the LO frequency, (2) front end filtering which results in out-of-band linearity competitive with implementations using off-chip high-Q filters, and (3) noise performance close to traditional receiver architectures. Additionally, we will show that we can tune (1) and (2) across a wide range of LO, IF and RF frequencies with digitally programmed baseband circuits.

3.2 Baseband-Controlled Impedance Matching

3.2.1 Analysis of Passive Mixer

In order to analyze the passive mixer, we begin with the model in Fig. 3.1(a). A quadrature passive mixer is connected directly to an antenna carrying input voltage waveform V_{RF} and with antenna impedance Z'_a. Here we model the transistors of the mixer as ideal switches with small series resistance R_{sw}. Each switch is loaded with a capacitor, C_L, and a resistive load R_B. The switches are driven with four 25% duty cycle non-overlapping

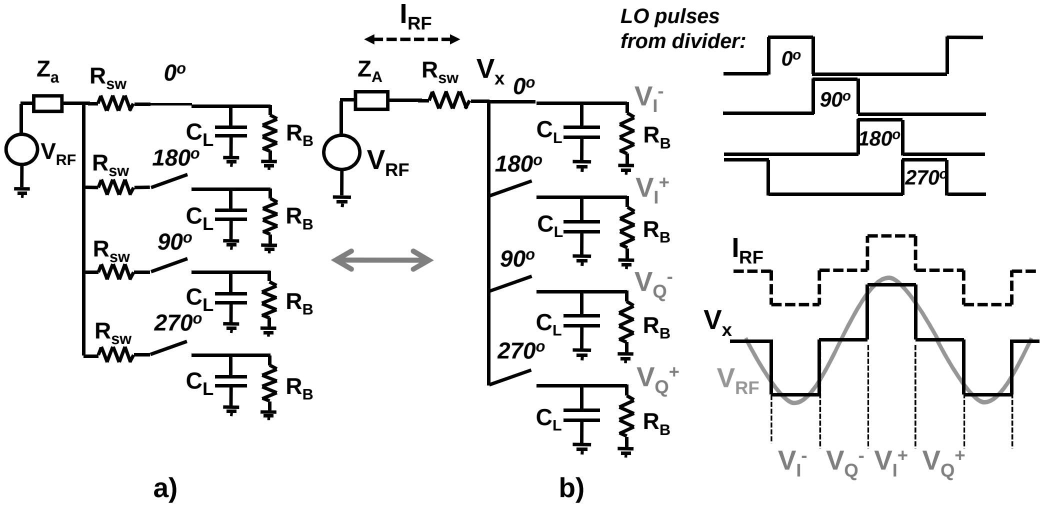

Figure 3.1: a) Model of 4-phase passive mixer with sampling capacitor C_L and load resistor R_B, b) equivalent model, with LO driving waveforms and resulting RF current and virtual voltage V_x

LO pulses [9, 12, 15–17, 29]. The non-overlapping nature of the pulses means that the antenna port will see only one path at a time, so we can treat the four parallel switch resistances as one, as seen in Fig. 3.1(b) and [31]. As each switch is closed, the signal V_{RF} during that LO pulse is sampled onto the corresponding C_L. The resulting four steady-state voltage levels correspond to differential I and Q down converted baseband signals. The charge on each capacitor slowly leaks through the load R_B to ground. However, as long as R_BC_L is chosen such that its resulting time constant is much larger than a period of the LO, the change in voltage due to this dissipation of charge over a single LO cycle will be small relative to the baseband signals V_I and V_Q.

Because passive mixers are bidirectional, the baseband signals present on the capacitors will also be back up-converted during each LO cycle. As a result, we may define a waveform V_x at the virtual node marked on Fig. 3.1(b), representing the up-converted and superposed baseband voltages. Furthermore, using this V_x, we can define a current I_{RF} representing the net current coming from the antenna port. Specifically, we expect that I_{RF} will be proportional to both the current discharged through the baseband resistors and the current coming from the antenna. In fact, we can surmise that the effective impedance seen by the antenna will be a series combination of R_{sw} and a scaled version of R_B. The scaling factor for R_B can by calculated by balancing the charge delivered by the input signal to the load C_L [29, 30, 32]:

$$\gamma = \frac{2}{\pi^2} \tag{3.1}$$

This implies that if we design the mixer switches to have a small resistance, the impedance presented to the antenna will largely be a function of R_B. We can therefore tune the impedance match with R_B.

3.2.2 Effect of Harmonic Conversion

Looking at the waveform V_x in Fig. 3.1b, we see that its spectrum must contain the original input signal, V_{RF}. However, the square shape of V_x indicates that it contains signal power at all of the odd harmonics of the LO in addition to the fundamental. The fact that the mixer samples with quadrature LO signals results in image rejection, and so reduces this content by eliminating one image for each harmonic, as seen in Fig. 3.2 and [33]. The remaining odd harmonics on the antenna port will reradiate, and so dissipate power at these frequencies. Because these harmonics depend on the incoming signal, they represent an additional loss mechanism other than R_B and R_{sw}. Since each harmonic is proportional to, and generated by the received signal on the baseband, this dissipation will reduce the power of the wanted signal. We model this loss as a frequency dependent conductance at each odd harmonic, shunting the mixer output.

$$Y_{a,n} = \frac{1}{n^2} \frac{1}{Z_a'(n\omega_{LO}) + R_{sw}} \tag{3.2}$$

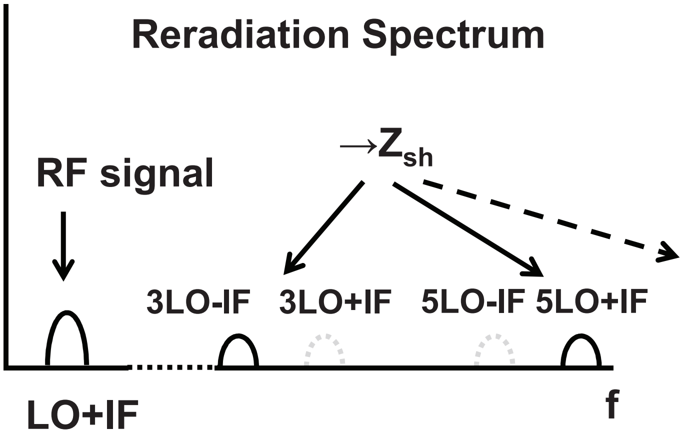

Figure 3.2: Spectrum of the reradiation at the antenna interface due to V_x

We calculate the total loss due to harmonic reradiation by summing the effect of each conductance. We model this overall loss as an impedance in shunt with the mixer output, Z_{sh}, defined as [30]:

$$Z_{sh} = \left[\sum_{n=3,5,7...}^{\infty} |Y_{a,n}| \exp(j(\angle Y_{a,n} + \frac{n\pi}{2})) \right]^{-1} \tag{3.3}$$

For a system with an antenna impedance which is constant across all frequencies, we can perform the sum in (3.3) and find a value for Z_{sh} as a function of the RF port impedance Z'_a and switch resistance R_{sw}:

$$Z_{sh} = \frac{4\gamma}{1-4\gamma}(R_{sw} + Z'_a) \approx 4.3(R_{sw} + Z'_a) \tag{3.4}$$

In a typical system, where $R_{sw} = 20\Omega$ and $Z'_a = 50\Omega$, this translates to $Z_{sh} = 300\Omega$.

With all the losses now taken into account, we can construct a linear time-invariant (LTI) model for the passive mixer. We have already combined the four switch resistances into one, since only one switch is on at a time. Now we can also do the same for the baseband load R_B, noting that we must multiply it by the scaling factor γ from (3.1). We must also add the virtual impedance Z_{sh} in shunt with R_B. The resulting model is shown in Fig. 3.3. This is similar to that presented in [31] but with the inclusion of Z_{sh}. From this model we can write a simple equation for the input impedance of the mixer:

$$Z_{in} = R_{sw} + \gamma R_B \parallel Z_{sh} \tag{3.5}$$

Note that this analysis applies to receive signals with a non-zero IF when R_B from (3.5) is changed to $Z_B(\omega_{IF})$ to account for reactive components in the baseband (such as C_L) [30].

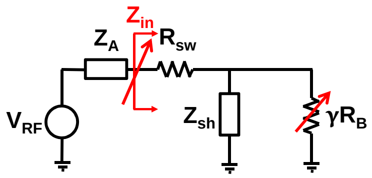

Figure 3.3: LTI model for 4-phase passive mixer

3.2.3 Benefits of 8-phase mixing

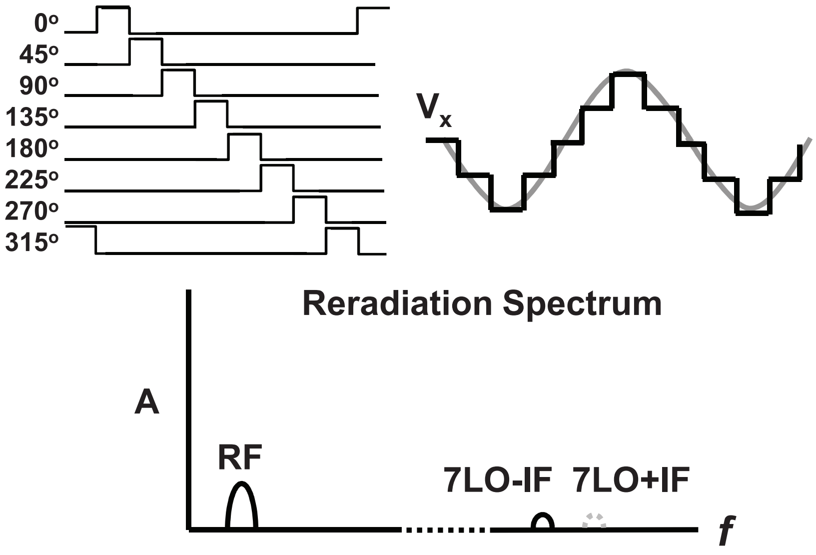

Figure 3.4: LO waveforms for an 8-phase passive mixer, approximation of waveform V_x for 8-phase mixer, and resulting reradiation spectrum

The expression for Z_{in} from (3.5) has two components which are a function of the duty cycle of the sampling waveform: γ and Z_{sh}. We can see that Z_{sh} will always limit the influence of R_B on the impedance match. From section 3.2.2 we see that Z_{sh} represents shunting due to power near the harmonics of the LO. In order to reduce harmonic reradiation, we introduce the mixer in Fig. 3.4, which contains eight switches instead of four and is driven with eight 12.5% duty cycle LO pulses [12, 13, 18, 20]. The resulting V_x waveform contains power at half as many harmonics as in the 4-phase mixer case (see Fig. 3.4). Specifically, the 8-phase passive mixer eliminates content at the 3rd, 5th, 11th, 13th harmonics and so on. As a result, R_{sh}, and the range of Z_{in}, increase dramatically. Additionally, the 8-phase mixer yields a new value for the γ scaling term:

$$\gamma_{8ph} = \frac{2}{\pi^2}(2 - \sqrt{2}) \tag{3.6}$$

For the case of a constant antenna impedance, this implies:

$$Z_{sh8ph} = \frac{8\gamma_{8ph}}{1 - 8\gamma_{8ph}}(R_{sw} + Z_a') \approx 18.9(R_{sw} + Z_a') \tag{3.7}$$

In a typical system, where $R_{sw} = 20\Omega$ and $Z_a' = 50\Omega$, this translates to $Z_{sh} = 1323\Omega$, which is about five times larger than in the 4-phase case.

3.3 Implementation

Following the analysis in section 3.2, we have designed a passive mixer-first receiver with tunable baseband impedance matching and the option of using either 4- or 8- phase mixers. Fig. 3.5 shows the implemented single-chip receiver architecture, including a programmable 4- or 8- phase frequency divider, quadrature passive mixers, baseband LNAs, and harmonic recombination amplifiers.

The receiver was fabricated in 65nm 1P9M CMOS. The photograph of the chip can

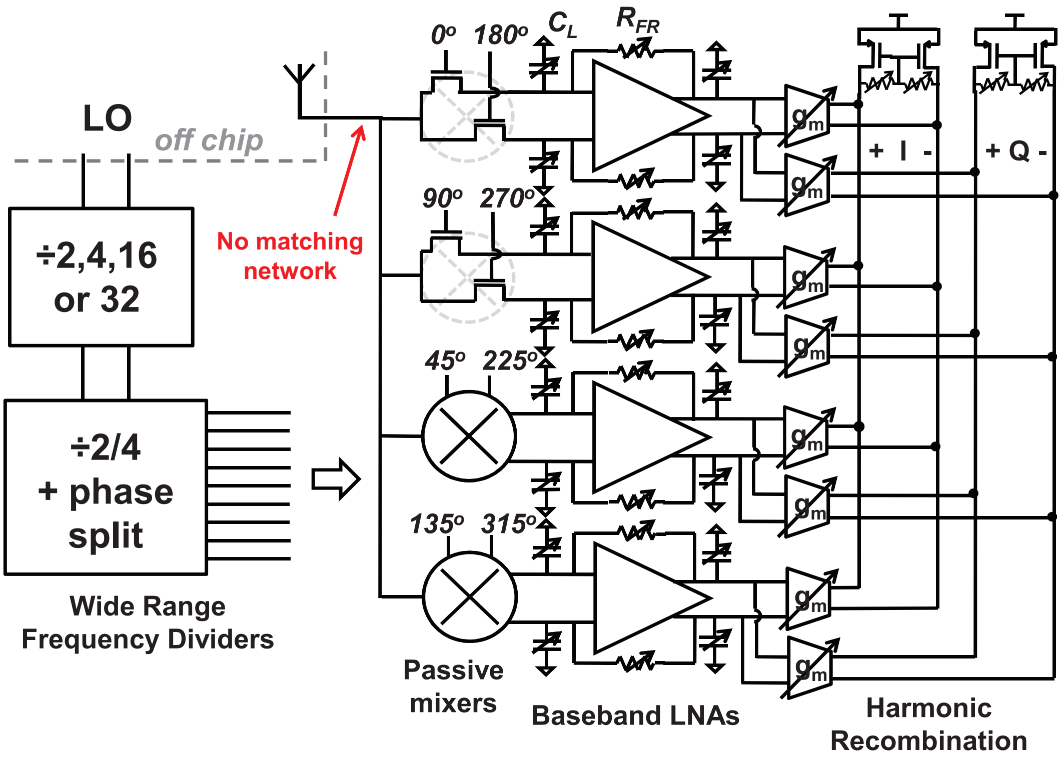

Figure 3.5: Block diagram of receiver including frequency dividers, passive mixers, baseband LNAs, and recombination buffers

be seen in Fig. 3.6. The total area is 2.5mm^2, with an active area of 0.75mm^2 The chip was packaged in a PQFP package and mounted onto a PCB for all measurements. The circuits operate off dual voltage supplies, with the LO buffer, frequency dividers, and mixers using 1.2V and the baseband circuitry using 2.5V. When all the strips are turned on, the 1.2V supply consumes between 6 and 33mA, depending on the LO frequency, and the 2.5V supply consumes 12mA. This translates to a power consumption of between 37 and 70mW.

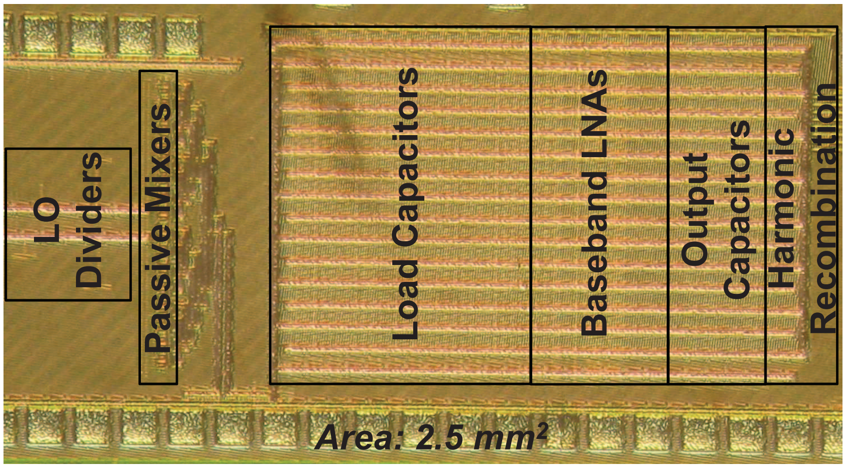

Figure 3.6: Picture of receiver implemented in 65nm CMOS showing functional blocks

3.3.1 Passive Mixer

The passive mixer was implemented with triple-well 1.2V NMOS transistors with $W = 16\mu\text{m}$, $L = 60\text{nm}$. The bulk of the mixer devices (and all 1.2V devices) is tied to the middle of the 2.5V rail. This allows both the inputs and the outputs of the mixer to sit at levels which bias the baseband amplifiers.

When operating in the 4-phase LO case, there is a maximum of eight of these transistors driven by each LO pulse (eight switches in parallel), which reduces the overall switch resistance. In 8-phase operation, a maximum of four unit switches are driven by each individual pulse. As a result, the effective R_{sw} for 8-phase operation is twice that of the 4-phase case. The receiver offers the option of turning off redundant switches, LO generation circuitry, and baseband circuitry in order to operate in a lower power state with as little as only one transistor for each LO pulse.

3.3.2 Frequency Dividers

In order to generate 25% duty cycle quadrature LO pulses, we employed a frequency divide-by-two, composed of two differential latches clocked by opposite phases of the input LO. The standard architecture then combines the outputs of the divider in AND gates to generate quadrature LO pulses [29]. In simulation we found that this approach tended to degrade noise figure, due to flicker noise in the dividers. This effect can be explained by coupling of LO onto the RF port, which is then down converted to baseband. Ideally, a 4-phase mixer will only reradiate at multiples of the 4^{th} harmonic of the effective LO. However, jitter of individual pulse edges results in reradiation at the receive frequency as well. These deviations are especially hard to suppress through device sizing, as the transistors in the dividers must drive significant internal loads at high speed as part of multi-transistor stacks.

Instead, we implemented pulse generation as shown in Fig. 3.7, by ANDing the divider outputs with the input LO to produce non-overlapping LO phases which are independent of timing variation in the counter itself [34]. This approach was expanded to the 8-phase case by building a four stage differential Johnson counter followed by AND gates to generate eight pulses, split by 45°, but 25% duty-cycle. These pulses were then ANDed with the original LO to generate 12.5% pulses whose edges are insensitive to deviations in the counter.

3.3.3 Baseband Feedback Amplifiers

A transistor level schematic of the baseband amplifiers is shown in Fig. 3.8. The amplifier consists of a fully differential PMOS pair with NMOS loads and digitally controlled common mode feedback resistors R_L which provide three gain settings (between 25 and

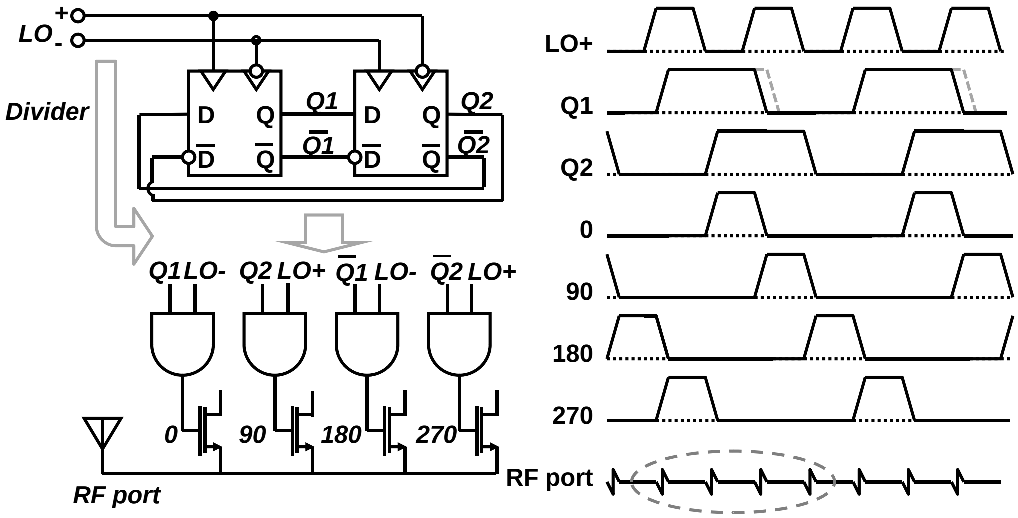

Figure 3.7: Schematic and timing diagram of 4-phase frequency divider

35dB). We chose PMOS transistors for the input pair and designed all amplifier transistors with long channels to reduce the $1/f$ corner to below 200 kHz. We implemented the

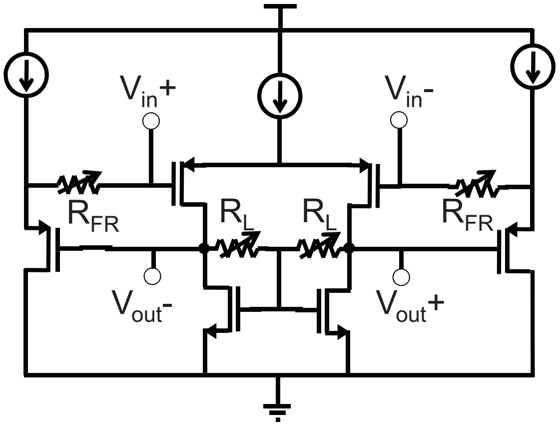

Figure 3.8: Transistor-level schematic of baseband LNA

matching resistor R_B from Fig. 3.1 by wrapping feedback loops around both paths. The feedback consists of a 5-bit tunable resistor R_{FR} connected to the input gates, in series with a source follower to buffer the output.

3.3.4 Harmonic Recombination Amplifiers

The receiver has a second stage of amplification (see right of Fig. 3.5) in which the eight signals are recombined into simple differential I and Q. These consist of tunable-g_m differential pairs which share a common PFET load with common mode feedback and four gain settings (from 16-34dB in 6dB steps). When operating in 4-phase mode, the separate but equal I and Q channels (0° and 90°) are simply added together. In 8-phase operation, the 0° phase channel is added with full weight to I, and the 90° phase with full weight to Q. The additional 45° and 135° channels are weighted by $1/\sqrt{2}$ and added to both I and Q, with different polarities. This weighting acts to cancel signals present at half the harmonics of the signal (i.e. the 3rd, 5th, 11th, 13th, etc) [13, 18, 20]. The degree of harmonic suppression achievable in these amplifiers is limited by the precision of the $1/\sqrt{2}$ weight (here it was designed to be $11/16$) and mismatch in the recombination stage.

In total, the LNAs and the recombination amplifiers provide more than 70dB of gain with a maximum BW of 20MHz, limited by the parasitic capacitance of the amplifiers and some fixed capacitance local to the mixer outputs to shunt switching transients.

3.4 Impedance Matching: Measurements

To provide a reference for the impedance matching measurements in this section and the following ones, we begin by defining an expected effective impedance presented to the mixer by the baseband which incorporates the gain of the feedback amplifier A, the feedback resistor R_{FR} and the scaling factor γ:

$$R_{EQ} = \gamma R_B = \gamma \frac{R_{FR}}{1 + A} \tag{3.8}$$

In order to confirm the analysis in section 3.2, we have measured the input impedance

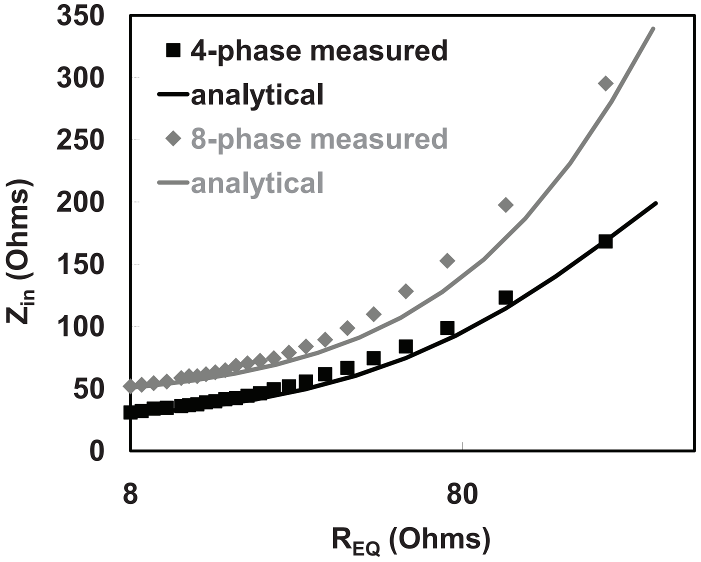

Figure 3.9: Comparison of direct measurement of input impedance at f_{LO} =100MHz with prediction from LTI model for both 4- and 8- phase mixers

of the receiver directly for f_{LO} = 100MHz, f_{RF} =101MHz. The resulting curves (shown in Fig. 3.9) show the effect of sweeping the real feedback resistor R_{FR} (scaled to R_{EQ} for both 4-phase and 8-phase operation. We have also included the curves which result from applying (3.5) for simulated A (30dB) and independently measured R_{sw} and R_{sh} (4-phase: R_{sw} = 20Ω, R_{sh} = 350Ω; 8-phase: R_{sw} = 40Ω, R_{sh} = 1100Ω). As predicted, the effective R_{sw} is about doubled for the 8-phase case. Note also that Z_{sh} is lower than predicted earlier for the 8-phase case. This is because the RF port impedance is frequency dependent. Since higher harmonics account for more of the value of Z_{sh} for the 8-phase case, if the impedance is lower at those higher frequencies, the constant Z'_a model will start to fail.

We also measured the harmonic reradiation out of the RF port predicted in section 3.2, and the difference in reradiation as a result of 8-phase mixing from Fig. 3.4. In particular, we looked at reradiation of injected RF signal up converted to a higher harmonic (as distinct from simple reradiation of LO signals coupling onto the RF port through mixer switch parasitics). Recall that this harmonic reradiation is the underlying mechanism behind the virtual lossy element Z_{sh} in the LTI mixer model in Fig. 3.3. Fig. 3.10 shows the measurement for an RF signal injected at 1.001GHz with a 1GHz effective LO, which generates a signal at 2.999GHz, 1MHz below the 3rd harmonic of the LO. This harmonic reradiation is indeed proportional to the input RF signal strength, and is reduced by about 18dB with 8-phase mixing. We also measured simple LO reradiation at 1GHz to be about -65dBm.

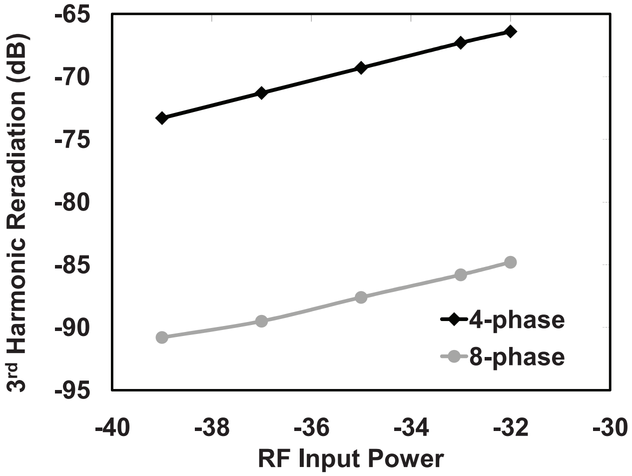

Figure 3.10: Measurement of reradiation out of the RF port at 2.999GHz for an RF signal injected at 1.001GHz

Beyond simply measuring the input impedance, we have also characterized the ability of the receiver to improve an impedance match by tuning R_{FR}. Fig. 3.11 shows a measurement of S_{11} at f_{RF}=1.001GHz and f_{LO}=1GHz as the feedback resistors are swept for both a 4-phase and 8-phase mixer and driven by a 50Ω source. These curves show that tuning the resistor does in fact allow for a minimum S_{11}. We have also overlaid simulation results for the same sweeps. In simulation, we modeled the packaging parasitics with a 2nH series inductance and 300fF shunt capacitance. These parasitics create a complex antenna impedance which is frequency dependent, and affects Z_{sh}. The minimum is for a different effective R_{EQ} in the different mixing cases, because of their different R_{sw} and Z_{sh} values. However, the match also changes for different IF frequencies, and is asymmetric due to the complex antenna impedance (as will be discussed in section 3.6.1). The effects of complex antenna impedance on matching are explored further in [30]. Figure 3.12 shows that our impedance match is not dependent on the LO frequency to first order but only on the IF (as explained in section 3.6.1). Here we tuned the feedback resistor to provide a good match for an LO of 800MHz. We then moved the LO in 100MHz steps both upwards and downwards and measured the S_{11} for 100MHz around the LO using a network analyzer (without retuning baseband components). The impedance match begins to break down at higher frequencies because the package parasitics begin to dramatically impact Z_{sh} at these frequencies.

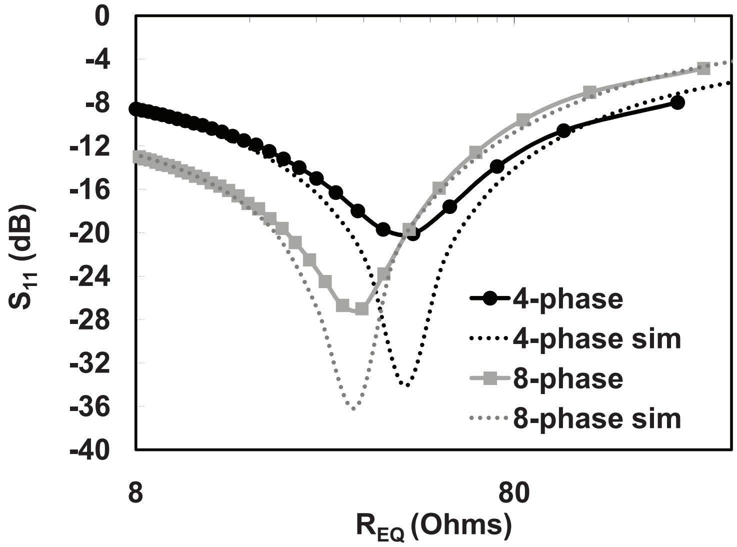

Figure 3.11: Comparison of simulation and measurement of S_{11} at f_{LO} =1GHz vs effective R_B for both 4- and 8- phase mixers

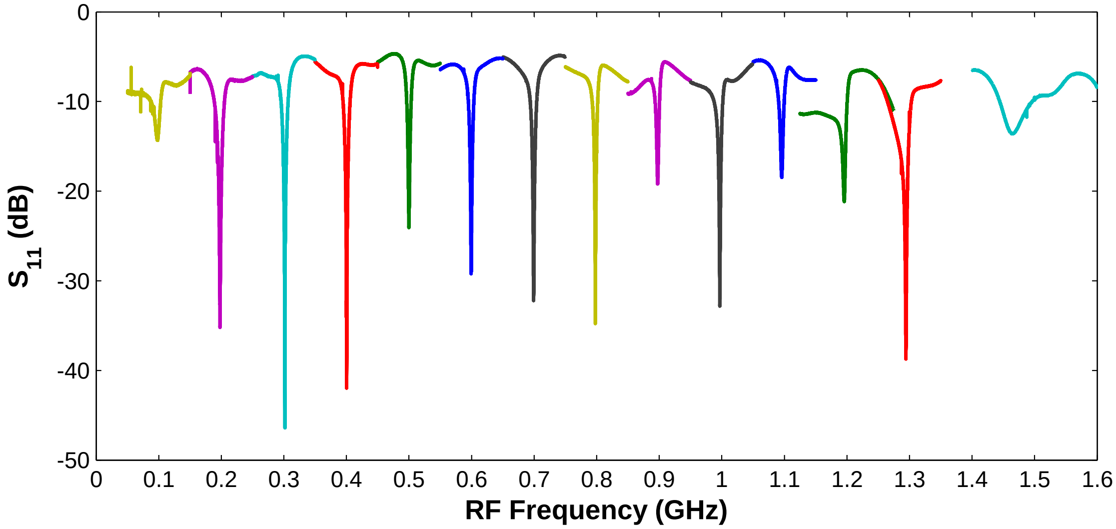

Figure 3.12: Measurement of S_{11} around LO frequency stepped by 100MHz, without any retuning of impedance match

3.5 Noise Performance

3.5.1 Analysis

In order to evaluate the noise performance of the receiver, we first need to look at the various sources of noise in the circuit shown in Fig. 3.1b. There are three fundamental sources of noise: the baseband resistance R_B, the switch resistance R_{sw}, and the thermal noise from the antenna itself, Z_a'. Recent work has shown that flicker noise from the switches in passive mixers is negligible [29]. Evaluating the noise figure (inside the baseband bandwidth) from this circuit yields a result which is dominated by R_B, and will always be greater than 3dB. However, our receiver implements R_B as a feedback resistor wrapped around the baseband low noise amplifier (see Fig. 3.13). This technique suppresses the noise from R_B by a factor proportional to the gain of the amplifier.

There is an additional source of noise in the circuit: the noise which is down-

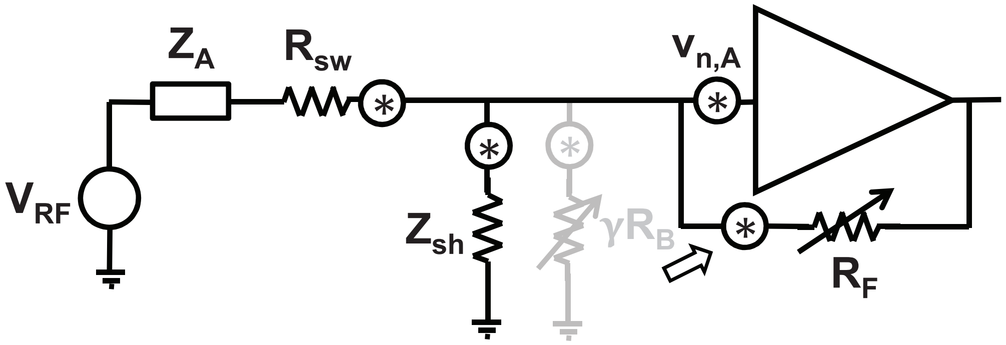

Figure 3.13: Schematic displaying noise sources in equivalent receiver model

converted by the mixer at odd harmonics of the LO. We can represent this as a noise current which passes through the RF port at each of the harmonics with:

$$\frac{\overline{i^2_{n,a}(n\omega_{LO})}}{Hz} = \frac{4kT}{n^2(Z'_a(n\omega_{LO}) + R_{sw})} \tag{3.9}$$

However, we note that the sum of the RF port noise currents at the harmonics of the LO is exactly the noise that would be generated by R_{sh} if it was a real resistor defined by (3.4). We can therefore use the model in Fig. 3.13 to find the noise factor of our receiver:

$$\begin{aligned} F \;=\;& 1 + \frac{R_{sw}}{R'_a} + \frac{R_{sh}}{R'_a}\left(\frac{R'_a + R_{sw}}{R_{sh}}\right)^2 \\ & + \gamma\frac{R_{FR}}{R'_a}\left(\frac{R'_a + R_{sw}}{\gamma R_{FR}}\right)^2 \\ & + \gamma\frac{\overline{v}^{*2}_{n,A}}{4kTR'_a}\left(\frac{R'_a + R_{sw}}{\gamma R_{FR}} + \frac{R'_a + R_{sw} + R_{sh}}{R_{sh}}\right)^2 \end{aligned} \tag{3.10}$$

The second term represents the noise contributed by R_{sw}. The third term represents the noise contributed by the virtual shunt resistor R_{sh}. The fourth term represents the noise contributed by the feedback resistor R_{FR}. The fifth term represents the noise contributed by the amplifier. Note that (3.11) applies to both 4- and 8-phase mixing, with the parameters Z_{sh}, γ, and in our implementation, R_{sw} changing. In the ideal case where R'_a is constant across frequency, the 8-phase mixer will have a significantly lower NF than the 4-phase mixer. The analysis leading up to (3.11) is provided in greater detail in [30].

3.5.2 Measurements

Fig. 3.14 shows the measured DSB NF for the receiver across the frequency range of operation, with an IF at 1MHz in each case. The frequency range in the 8-phase mode is lower because it divides the input LO by four instead of two as in the 4-phase case. As predicted, the NF for 8-phase operation is lower than for 4-phase operation. NF degradation at higher frequencies is likely due to shunting by package and device parasitics. Such parasitics will also have more effect at higher harmonics, and so will decrease R_{sh}, degrading NF. In addition, at higher frequencies, the LO pulses driving the mixers are likely to become less ideal, potentially increasing the effective R_{sw} and decreasing R_{sh}. Following the analytical result in the previous section, we have also

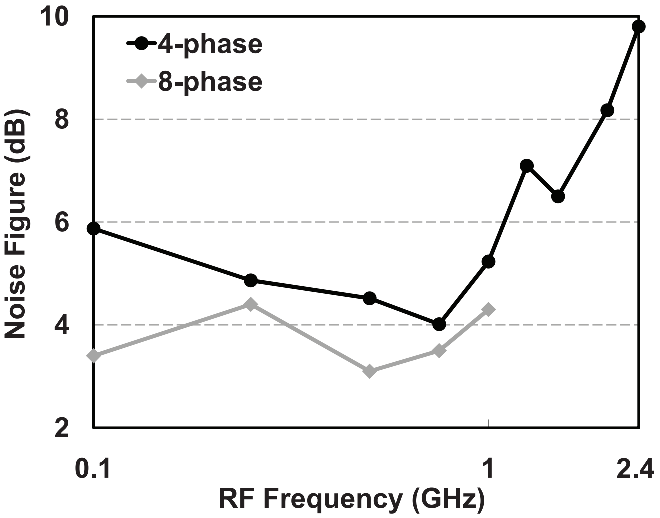

Figure 3.14: Measurement of NF vs RF frequency for both 4-phase and 8-phase operation

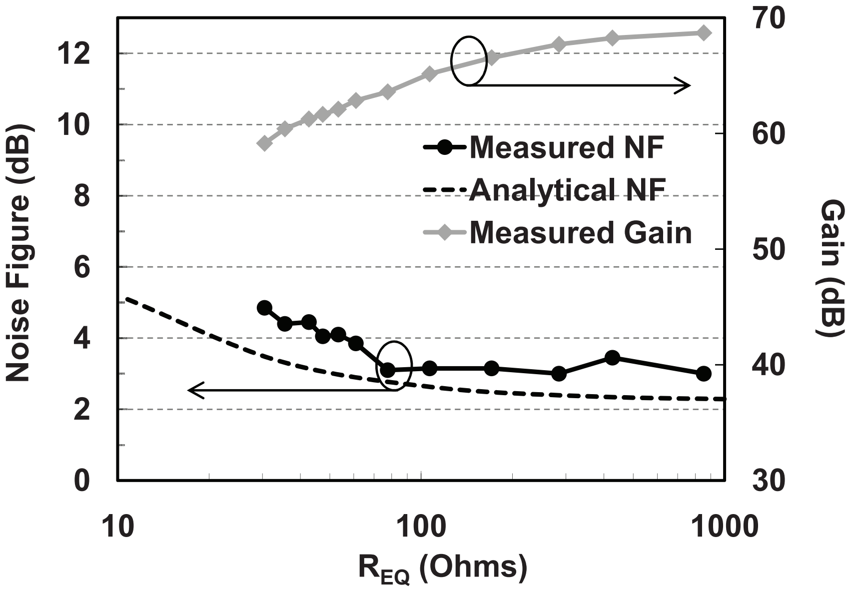

Figure 3.15: Measurement of NF and voltage gain vs R_{EQ} as R_{FR} is swept for the 8-phase receiver at f_{RF} = 900MHz, with analytical NF result for comparison

measured the noise figure of the 8-phase receiver for a range of values of R_{FR} (shown in Fig. 3.15). As predicted from (3.11), as long as the ratio of R_{FR} to R'_a and the ratio of R_{sh} to R'_a are large, the noise figure will be fairly constant, low, and dominated by the baseband amplifier noise. As R_{FR} decreases, these ratios increase and the 3rd and 4th terms in (3.11) eventually blow up, increasing the noise figure. Fig. 3.15 also shows the gain of the receiver for the same values of R_{FR}, where gain decreases as R_{FR} (and so R_{EQ}) decreases. Note that while this NF result reaches levels as low as 3dB, this is still 1-2dB higher than that predicted in simulations in [30], and by (3.11), whose result is overlaid with the measurement above. The flicker noise corner of the receiver was also measured and found to be less than 200kHz under minimum NF conditions.

3.6 Blocker Filtering and Linearity

3.6.1 Effect of Sampling Capacitor C_L

The presence of the baseband capacitor C_L has several notable effects on the tunable impedance presented to the RF port. As f_{IF} passes the RC bandwidth of the baseband, Z_{in} becomes dominated by C_L, and ultimately approaches R_{sw}. By making this capacitor tunable (as shown in Fig. 3.5), we create a tunable-Q BPF. This transfer of filtering through a switching mixer was first introduced as N-path filtering many years ago [35], and has been used recently in literature to provide filtering for systems which place an LNA at the RF-front-end [14, 32, 36, 37].

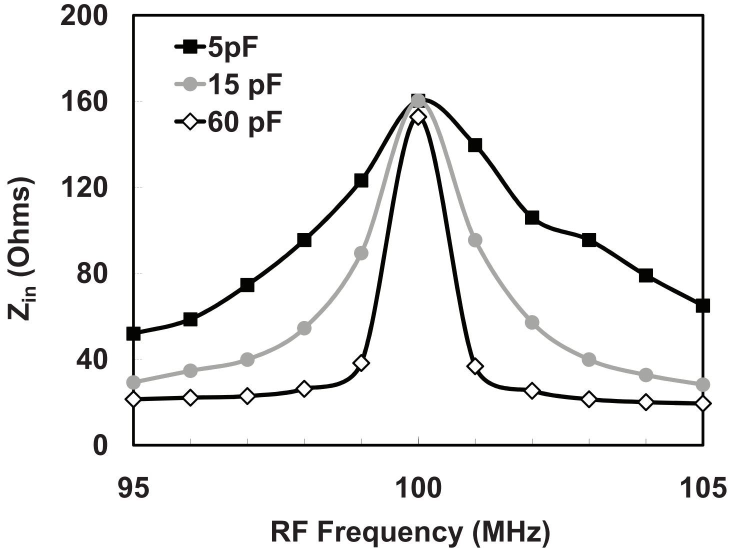

Figure 3.16: Direct measurement of tunable bandpass filter created by C_L

In our implemented receiver, we have made C_L digitally controllable with 6 bits of resolution (from 5pF to 120pF). Fig. 3.16 shows measurements of the magnitude of impedance presented by the receiver for three different values of C_L as RF frequency is swept around a 100MHz LO. For frequencies very near the LO, the receiver presents the impedance we expect based on the chosen feedback resistance, and as the RF moves away, this impedance is controlled by the capacitor and reduces as $|f_{LO} - f_{RF}|$ increases (or as C_L increases). Note also that this impedance reaches a lower limit set by the on resistance of the mixer switches (about 20Ω).

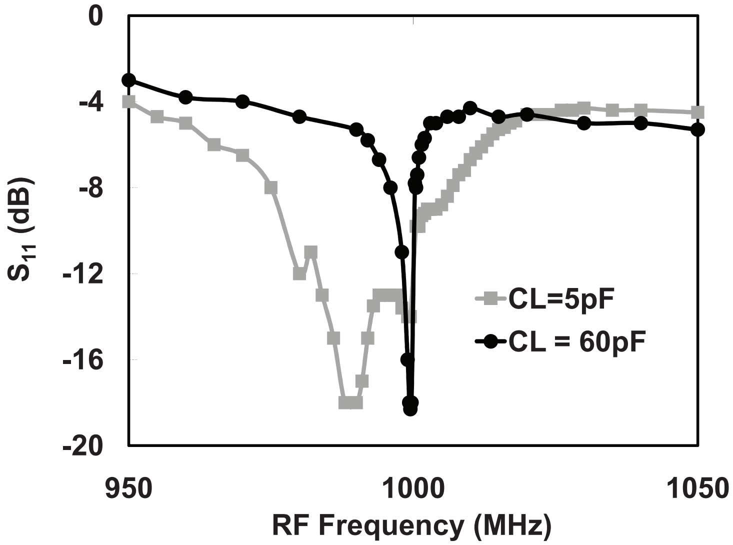

Figure 3.17: Measurement of effect on S_{11} curve of tunable bandpass filter created by C_L

Furthermore, in Fig. 3.17, we have confirmed this effect at higher frequency with a measurement of S_{11} for an R_{FR} value tuned to a good match. As we increase the capacitor value, the curve becomes much narrower and the deepest S_{11} notch is closer to the LO.

Finally, we also took direct measurement of both the real and complex components of the input impedance for f_{LO}=200MHz and C_L=60pF using a network analyzer (see Fig. 3.18). Clearly, the range of a good impedance match here is quite small, as the capacitor dominates the impedance for larger offset frequencies. Additionally, the imag-

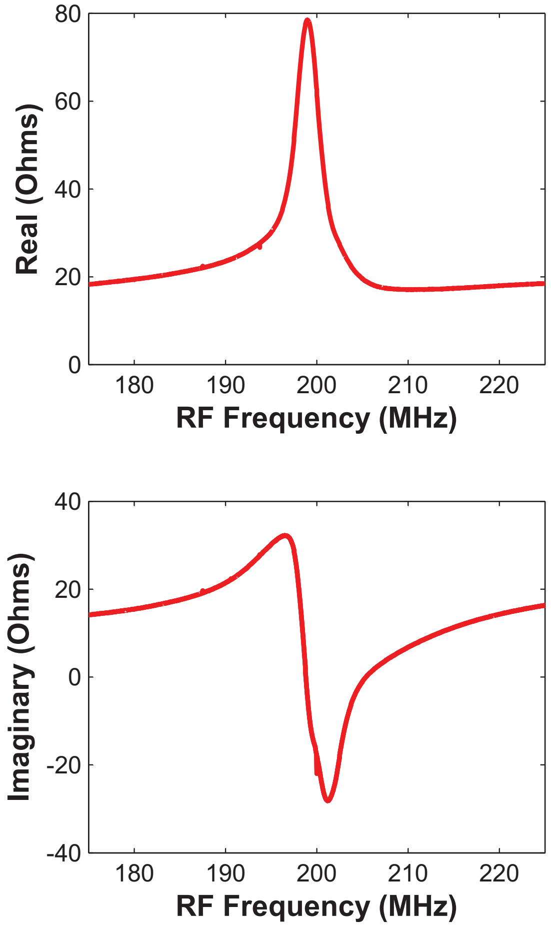

Figure 3.18: Measurement of real and imaginary components of impedance presented to the RF port by the receiver

inary component of the impedance demonstrates the interesting property of switching polarities for negative offset frequencies, as predicted theoretically in [30] and [31], and discussed in greater detail in section 3.4.

3.6.2 IIP2, IIP3 and Out-of-band Compression Measurements

One implication of having this tunable BPF on the RF port is that it will have a large influence on the out-of-band linearity performance of the receiver [16, 31, 38]. We have

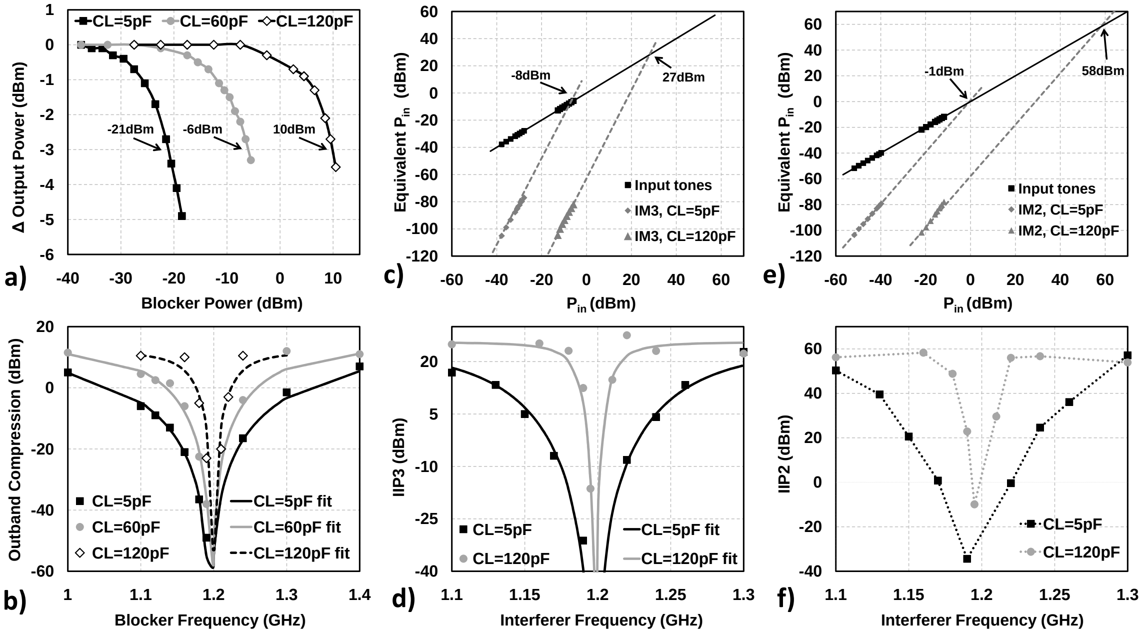

Figure 3.19: Measurements of outband compression, IIP3 and IIP2 around f_{LO}=1.2GHz

characterized the linearity of the receiver for various offset frequencies and capacitor settings. Figure 3.19(a) shows out-of-band compression due to a blocker at 1.16GHz for a 1.2006GHz RF, for three different C_L values. We define the out-of-band compression level as the power of the blocker which makes the wanted signal diminish by 3dB. In Fig. 3.19(b) we have also performed sweeps of the blocker frequency around the 1.2GHz RF for the three capacitor settings and measured out-of-band compression for each of them. We find that the measured compression levels are well fit by a simple equation (solid lines in Fig. 3.19(b)):

$$P_{OB3dB} = -20\log(k1 + \frac{k2}{f_{IFint}^2}) \tag{3.11}$$

Where $k1$ and $k2$ are fitting parameters and the form of the equation is consistent with a combination of two mechanisms: 1) a constant outband compression point of +10dBm for far out-of-band blockers which probably reflects compression in the mixer itself, and 2) a frequency dependent term that dominates at lower interferer IF frequencies and follows a $1/f_{IFint}^2$ dependency. This second component becomes weaker with larger capacitor values, and is consistent with a compressive third-order nonlinearity that acts after one pole of blocker filtering, and reflects nonlinearity in the baseband LNAs.

Fig. 3.19(c) shows the IIP3 measured using two tones (one at 1.22GHz and the other at 1.2406GHz), with a 1.2GHz LO (generating an IM3 product at 1.1994GHz, which was downconverted to a 600kHz IF), for two different settings of C_L. We achieve an IIP3 of 27dBm when a large C_L is chosen, and much worse IIP3 of -8dBm for the lower C_L. Fig. 3.19(d) shows the measured IIP3 for various offset frequencies (where the x-axis represents the frequency of the tone which is closer to the RF) for both C_L=5pF and C_L=120pF. This also shows that with a higher C_L engaged, the receiver maintains good linearity for much closer interferers. As before, this result is well fit by equations of a form similar to (3.11) which incorporate a combination of two mechanisms: a constant, very high IIP3 mechanism (presumably from the mixer), and a frequency dependent component that goes as $1/f_{IFint}^3$ and reflects a third-order nonlinearity in the baseband. These results are consistent with simulations of the baseband amplifiers alone, with the attenuation of the passive mixers and the RC pole accounted for. The out-of-band results are more difficult to replicate in simulation, as discussed in [31]. However, by applying a square-law model to the mixer switches, we computed an out-of-band IIP3 of 24dBm, which is close to our measurement.

Fig. 3.19(e) shows the IIP2 for a 2$^{\text{nd}}$ order inter-modulation product for two tones (one at 1.22GHz and one at 1.2206GHz), for a 1.2GHz LO, generating an IM2 at 1.2006GHz. We achieve an IIP2 of 58 dBm when a large C_L is chosen, and much worse IIP2 of -1dBm for minimum capacitor settings, as 20MHz is close to being within the bandwidth of the receiver. Fig. 3.19(f) shows the measured IIP2 for various offset frequencies for both C_L=5pF and C_L=120pF. As with other nonlinear effects, as interferers move in-band, they generate larger distortion products. Engaging a larger C_L decreases bandwidth, improving robustness to interferers much closer in frequency. Unlike the 3^{rd}-order nonlinearity described above, IIP2 does not follow a simple-to-fit rule, indicating that the mechanisms generating IIP2 are likely to be more complex than those generating IIP3.

Because the front-end bandwidth of this receiver is programmable, it is possible to trade off bandwidth for interference tolerance. Thus, the receiver can be programmed to receive signals with bandwidths >10MHz, but can also be reprogrammed to receive narrower bandwidth signals in the presence of blockers that would badly degrade the system if it were set to its original bandwidth.

Because this work focused on demonstrating low noise, impedance tunability and out-of-band linearity performance, little effort was made to linearize the baseband LNAs and recombination amplifiers for in-band linearity. We nonetheless have measured the in-band linearity of the receiver. For a 1GHz LO, we injected signals at 1.0012GHz and 1.0016GHz. These produced an IM2 product at 1.0004GHz and an IM3 product at 1.0008GHz. This resulted in an in-band IIP2 of -45dBm and an in-band IIP3 of -67dBm. In future designs, in-band linearity can easily be improved by designing higher linearity baseband circuits such as those used in [18]. Indeed, a sensible SDR-style approach would be to make linearity (traded off against power consumption) a programmable feature of the baseband.

3.6.3 Harmonic Suppression

In addition to characterizing the susceptibility of the receiver to general wideband interferers, we also measured the ability of the 8-phase mixer and recombination amplifiers to reduce the effect of blockers at the harmonics of the LO frequency. Because we have no RF front-end filter, the mixer will downconvert signals present at those harmonics.

We set up the receiver with an input LO of 2GHz, for an effective LO of 500MHz. In order to directly compare the 4-phase case with the 8-phase case, an additional divide-by-two is engaged for the 4-phase case such that both will receive signals around 500MHz. We then measured the difference in gain between signals injected at the fundamental (499MHz) and those injected at the 3rd and 5th harmonics (1.499GHz and 2.499GHz respectively). In the 4-phase case, the output power for the 3$^{\text{rd}}$ harmonic was 11dB less than the fundamental, and the 5$^{\text{th}}$ harmonic output was 19.9dB less. This is fairly consistent with the $1/3$ and $1/5$ weights which accompany these harmonics in the Fourier series of the square wave sampling signals. For the 8-phase case, which actively rejects these harmonics, the output due to the 3$^{\text{rd}}$ harmonic was 35.4dB less than the fundamental and that due to the 5th harmonic was 42.6dB less.

The harmonic rejection ratio achieved here is not sufficient to eliminate the influence of large blockers at the harmonics of the LO, limiting its applicability to some wireless standards. The limitations of our implementation come from the late harmonic recombination, coming after a first stage with 30dB of gain. However, recent works have presented harmonic rejection schemes which provide 60dB-80dB of rejection (depending on implementation) [18, 39]. These techniques could easily be applied to our design as well, providing a similar degree of rejection.

3.7 Complex Feedback

3.7.1 Motivation

While radios are most often designed to match a constant, purely real antenna impedance of 50Ω, in reality, the actual impedance of an antenna can vary widely at different operating frequencies and in different environments. Additionally, the mere presence of parasitics on the PCB, package, bond wires and pads inherently make the effective antenna impedance complex. As seen in Fig. 3.11, the center of the S_{11} notch for our passive mixer-first receiver is not directly centered around the LO but offset by several megahertz. This is due to the baseband complex impedance presented by the capacitor C_L interacting with the parasitic complex components of the antenna port.

Figure 3.18, which shows the impedance presented by the receiver as a function of IF frequency, shows that the imaginary component of Z_{in} looks negative for positive IF and positive for negative IF. On the upper sideband of the LO, the antenna port sees the impedance presented by the baseband port as a function of the IF, but the lower sideband sees the *complex conjugate* of this impedance [30, 31]. This implies that the required complex conjugate match for a complex antenna impedance can only exist at a single IF frequency.

In principle, the imaginary component of this match is tunable since we have control over the value of the capacitor. However, using the sampling capacitor to provide a complex impedance match has the disadvantage that it will limit the bandwidth of a good match. Worse, it can only be used to match one polarity of imaginary antenna impedance, or in other words it can only match that impedance on one of the side bands of the LO.

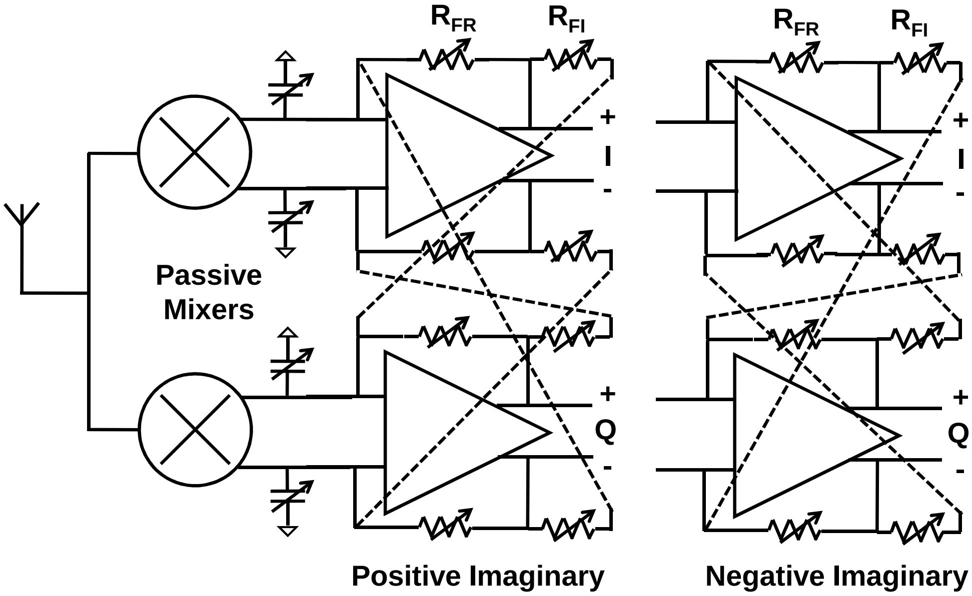

Figure 3.20: Receiver schematic with complex feedback

3.7.2 Implementation

In order to solve the problem of matching to complex antenna impedances, we have implemented the circuit in Fig. 3.20, which modifies our original feedback amplifiers to provide “complex feedback”. Here we connect feedback resistors from the output of the I-channel of the amplifier to the input of the Q-channel, and vice-versa. These additional feedback paths present a 90° phase shifted (and scaled by R_{FI}) version of the original signals back to the amplifier inputs. This phase translates to a complex impedance presented to the antenna port through the passive mixer. A similar feedback technique is utilized in [40] and [19] but was used to modify the phase of a filter rather than to present a complex impedance to the input. Implementing R_{FI} in the same way as R_{FR}, and allowing for its polarity to be switched (as in Fig. 3.20) provides a programmable complex impedance match.

Analysis of the circuit in Fig. 3.20 yields an expression for the new baseband impedance Z_B where the real part is still mostly a function of the real feedback resistor R_{FR}, and the imaginary component depends on the value of the resistor R_{FI}. Note that R_{EQ} from (3.8) will change with the new Z_B from (3.12) to become Z_{EQ}.

$$Z_B = \left[\left(\frac{1 + A}{R_{FR}} + \frac{1}{R_{FI}} \right) \pm j \frac{A}{R_{FI}} \right]^{-1} . \tag{3.12}$$

One additional note is that because of the relative phases of sine and cosine, we actually need to flip the polarity of the feedback resistors from the Q channel to the I channel, in order to get the same equivalent phase shift. Of course this effect only operates within the bandwidth set by the baseband capacitors.

3.7.3 Measurements

In order to measure the effects of complex feedback, we set up the receiver to receive an RF frequency around 500MHz and swept the RF frequency using a network analyzer (see 27Ω curve in Fig. 3.21). We tuned the impedance match with the real feedback resistor to provide a deep S_{11} notch, without yet engaging the complex feedback (see 36Ω curve). We then turned on the complex feedback path with a positive R_{FI} value and swept the RF frequency again, as expected this shifted the IF frequency of the optimum S_{11}. We repeated this measurement with the opposite polarity of complex feedback, which results in a notch on the opposite side of the LO frequency. To show that complex feedback can be used to provide matching on both sidebands in the face of significant impedance mismatch on the RF port, we moved the effective LO frequency to 1GHz, where capacitive parasitics were much more dominant. Fig. 3.22 shows that without complex feedback, S_{11} is minimum at a significant IF offset from the LO. Engaging complex feedback shifts this optimum to very close to the LO frequency,

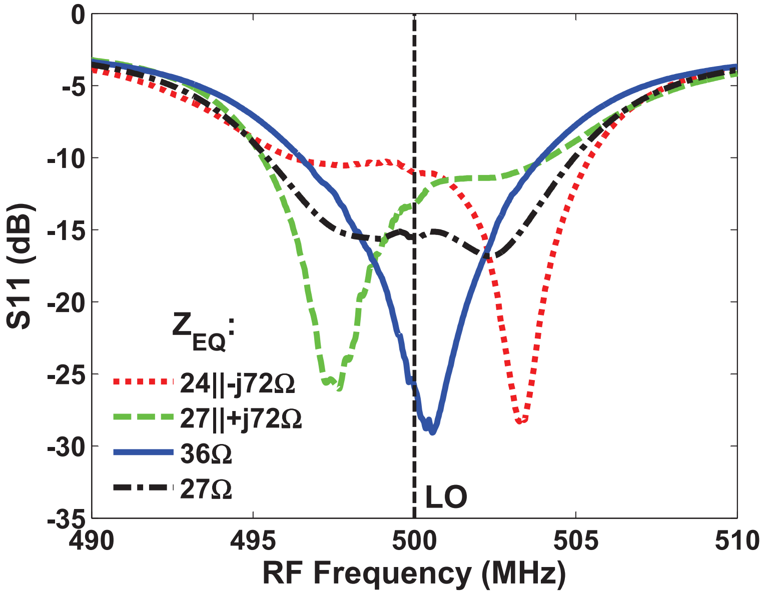

Figure 3.21: Measurement of moving S_{11} curve for both polarities of complex feedback, compared to curves without any complex feedback, with both tuned and untuned R_{FR}

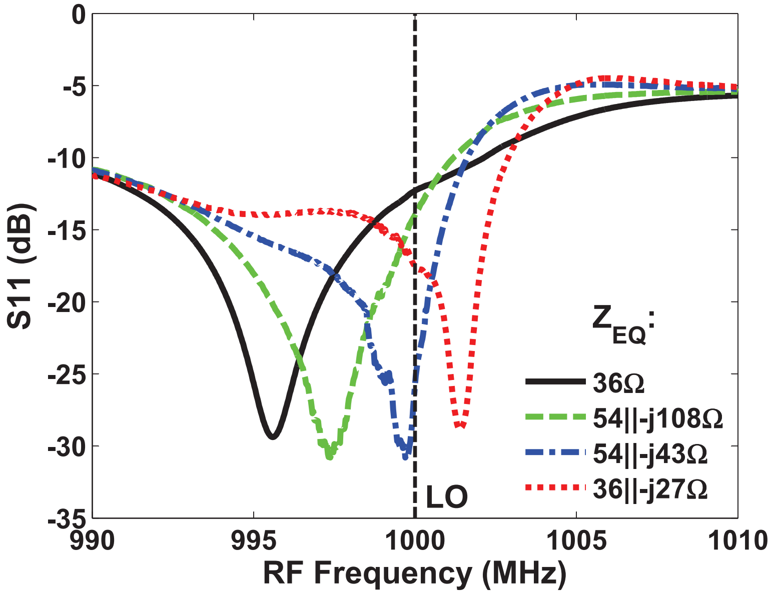

Figure 3.22: Measurement showing complex feedback pushing notch of S_{11} curve to the other sideband of the LO

and by further decreasing R_{FI} (effectively increasing the influence of complex feedback), we can move the S_{11} notch to the other sideband of the LO, dramatically improving S_{11} for that sideband.

The potential for instability is a limitation of complex feedback. As the magnitude of the cross-channel conductance is increased (R_{FI} is decreased), the inputs of the amplifier can see enough phase rotation to elicit oscillation in the baseband amplifiers (the baseband essentially becomes a ring oscillator). This can be an issue if the imaginary matching term is significantly stronger than the real term, and represents a limit on the complex antenna impedance that can be matched reliably.

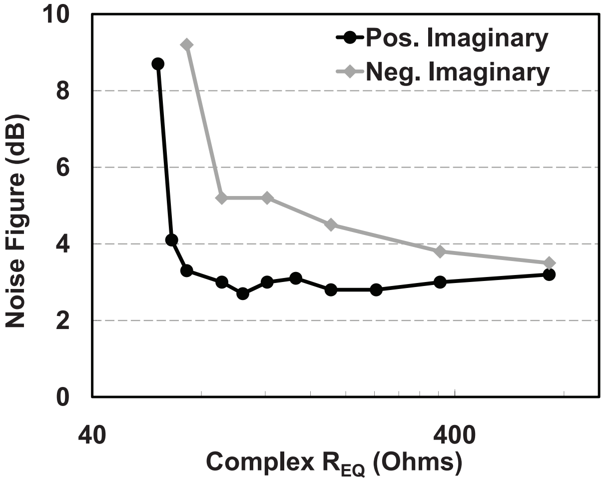

Figure 3.23: Measurement of NF of receiver vs imaginary component of Z_{EQ} for swept complex feedback resistor R_{FI}, in both polarities of complex feedback

Finally, we measured the effect of complex feedback on the NF of the receiver. Fig. 3.23 shows the DSB NF of the 8-phase mode receiver for swept R_{FI} of both polarities for an LO at 900MHz and a 1MHz IF. Not surprisingly, one polarity provides a better NF than the other because it provides an improved complex conjugate impedance match to the RF port.

Table 3.1: Summary of Performance

Technology	**65nm**
Frequency Range	**0.1-2.4GHz**
Gain	**40-70dB**
DSB NF	**4dB±1dB**
Out-of-band IIP3	**+25dBm**
Out-of-band IIP2	**+56dBm**
Power	**37-70mW**
Power Supply	**1.2V (RF) / 2.5V (Baseband)**
Impedance Match	$\boldsymbol{Z_{EQ} = (8 - 250) \parallel \pm j(8 - 250)\Omega}$

3.8 Conclusion

We have presented a software defined radio receiver capable of NF close to 3dB, out of band IIP3 up to 27dBm and 0.1-2.4GHz frequency tuning range, as summarized in Table 3.1. The architecture uses a passive mixer-first, LNA-less approach in order provide digital control of parameters in the entire antenna interface. The transparency of passive mixers translates the impedance on one side of them to the other. We used this effect to translate a LPF on the baseband to a BPF on the RF port, allowing for the selected rejection of out-of-band interferers. Feedback resistors on baseband differential LNAs allow for a tunable real impedance match within the bandwidth of the BPF. Additionally, we demonstrate “complex feedback”, which creates an effective complex impedance on the RF port by using feedback between the in-phase and quadrature paths of the baseband. We use this complex impedance to match complex RF port impedances. We show that the S_{11} notch tracks the LO frequency of the receiver, and is to first order only a function of the circuits present on the baseband. Finally, the receiver achieves competitive noise performance with state of the art receivers. This work demonstrates a receiver architecture that for the first time provides programmable RF impedance matching and filtering without sacrificing performance.

CHAPTER 4

EFFECTS OF LO HARMONICS AND OVERLAP SHUNTING ON N-PHASE PASSIVE MIXER BASED RECEIVERS

4.1 Introduction

Recent CMOS RF receiver designs have adopted passive mixers combined with frequency dividers to achieve a large frequency tuning range. With process scaling allowing for fast, low resistance switches, some designs have removed the LNAs at the front end of the receiver and connected a passive mixer directly to the antenna [8, 9, 41, 42]. These mixer-first architectures have now achieved noise figures competitive with LNA-first designs [41, 42], as well as providing RF impedance tunability (both for matching and filtering) to the front end by exploiting the impedance translation property of these mixers [30, 43, 44].

With passive structures at the receiver front-end, minimizing loss mechanisms (and therefore conversion loss) is critical to achieving low noise figure and strong impedance control. Two recent advances have enabled performance leaps by addressing such losses. The first is the use of 4 non-overlapping LO pulses to eliminate leakage between I and Q pathways. The second is using 8 non-overlapping phases of LO to alleviate loss to harmonic up-conversion, improving the noise performance as well as allowing for rejection of the 3rd and 5th harmonics [41, 42]. Here we look at two expansions on these ideas: 1) Increasing the number of phases beyond 8, and 2) exploring the effects of LO overlap on passive mixer performance, as well as demonstrating a technique for alleviating the effects of overlap.

Increasing the number of phases has many benefits in passive mixers particularly

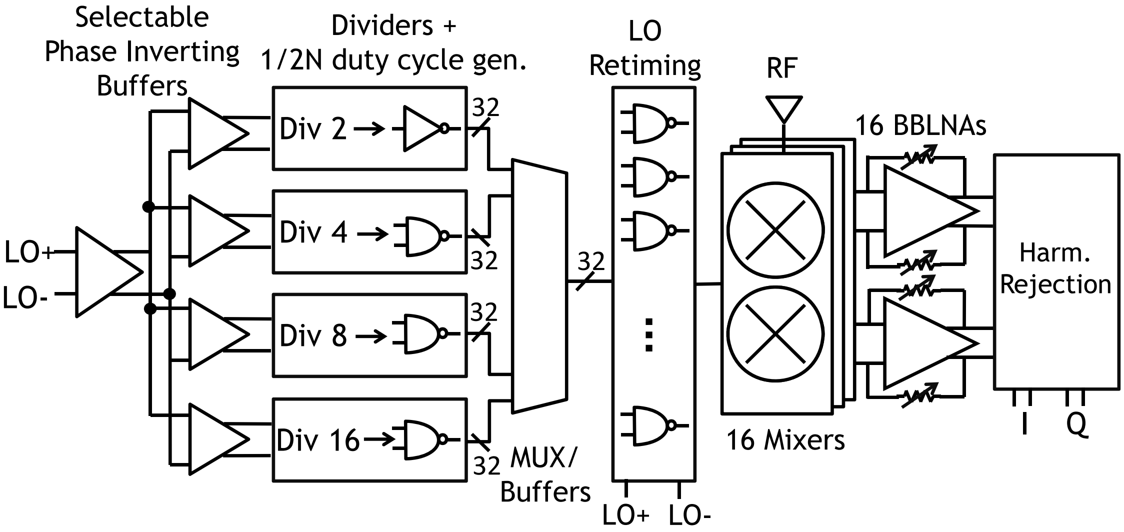

Figure 4.1: Block diagram of non-overlapping 4/8/16/32 phase receiver

when a system is designed to operate over a decade or more in frequency. In this chapter we propose a receiver configurable to 4, 8, 16 or 32 LO phases which can theoretically reject up to the 30th harmonic of the LO [45]. With these many phases and associated dividers, the receiver can use an input LO of 1.6GHz to 5.6GHz to receive from 100MHz to 2.8 GHz while rejecting all harmonics below 2.8GHz.

One of the primary limits to multi-phase mixing is generating 1/N duty-cycle non-overlapping pulses at high frequencies. It would be beneficial if this requirement of non-overlapping pulses could be relaxed. We have therefore included two additional RF front-ends (dividers and mixers tied to the same baseband) with controllable overlap, one of which includes a modified RF port to suppress leakage paths through overlap.

4.2 N-Phase Passive Mixer-First Receiver Architecture

Figure 4.1 shows the architecture of our non-overlapping N-phase receiver. The LO generation circuitry is comprised of four selectable separate Johnson counters which divide the incoming LO by 2, 4, 8, or 16 respectively, generating $N = 4, 8, 16$, or 32 LO phases. These phases are AND-ed together before exiting the divider block to generate pulses with $2/N$ the duty cycle at the divided-down frequency. The outputs are then driven into 32 dual purpose MUX/buffers, twice, to select the outputs of a single divider. Those dividers with fewer than 32 phases drive several of the MUXes with a single output. Finally these pulses are retimed by the original (pre-divider) LO signal, producing 32 distinct pulses (whose noise depends only on the original LO), which drive 32 distinct mixer switches. When in lower than $N = 32$ mode, each phase of pulse drives more than one mixer switch. Thus, the total fan-out is constant, and, for a given receive frequency, all four modes consume roughly equal power.

The outputs of the passive mixers feed into 16 parallel baseband LNAs with tunable feedback resistors to tune the input impedance of the receiver, and tunable shunt capacitors to set bandwidth. When 32 LO phases are used, each baseband path sees a different phase signal, but when fewer phases are used, all of the amplifiers are still used but with many seeing identical signals. In this design, because the number of phases is increased by splitting mixer switches into different phases, the effective switch resistance of the system will be lowest in 4-phase mode and increase as we increase the number of phases used. Additionally, adapting the model for the input impedance of the receiver in equation 4.1 and first presented in [41], we must modify the γ and R_{sh} terms for each number of phases as well. R_{sh} is higher with higher numbers of phases, and γ becomes lower.

$$Z_{in} = R_{sw} + \gamma R_B \parallel R_{sh} \tag{4.1}$$

$$Z_{sh} = \frac{N\gamma}{1 - N\gamma}(R_{sw} + Z_a')) \tag{4.2}$$

$$\gamma = \frac{\operatorname{sinc}\left(\frac{\pi}{N}\right)^2}{N} \tag{4.3}$$

Where, R_{sw} is the series resistance of the mixer switches, Z_a' is the RF source impedance, and R_B is the baseband load impedance. Equation 4.1 sets upper and lower bounds on the input impedance of the receiver, specifically such that:

$$R_{sw} < Z_{in} < R_{sw} + Z_{sh} \tag{4.4}$$

Figure 4.2 shows the effective linear time-invariant model for the impedance next to its graphical representation as a function of frequency. We see that the upper bound on input impedance occurs at the LO frequency and is set by Z_{sh}, with the width set by the filter created by the sampling capacitor C_L. The lower bound is set by the wideband switch resistance which is constant across frequency. Thus, the maximum in- to out-of-band attenuation at the RF input is limited to R_{sw}/Z_{sh}. Noise figure is enhanced minimizing R_{sw} while simultaneously maximizing Z_{sh}.

4.3 N-Phase Measurement Results

We fabricated the N-phase receiver in 65nm CMOS, with a total chip area of 3.5mm^2. The receiver achieved a frequency range of 0.1-2.8GHz, with a power consumption

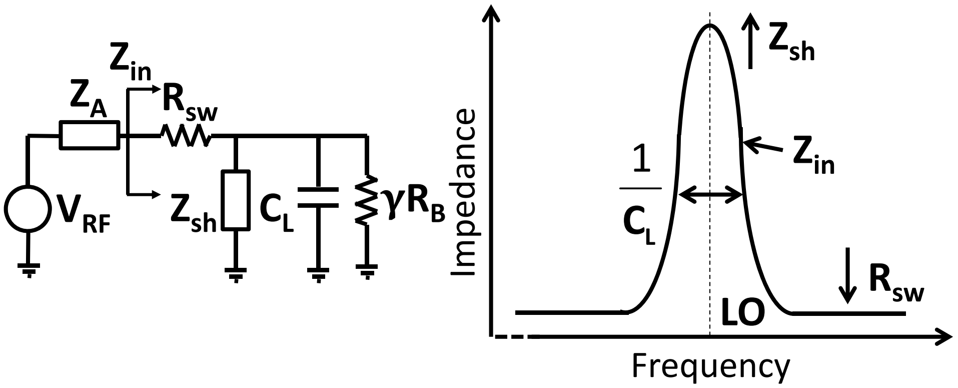

Figure 4.2: Schematic of input impedance model of passive mixer and theoretical shape of impedance across frequency, showing the limits placed by various components

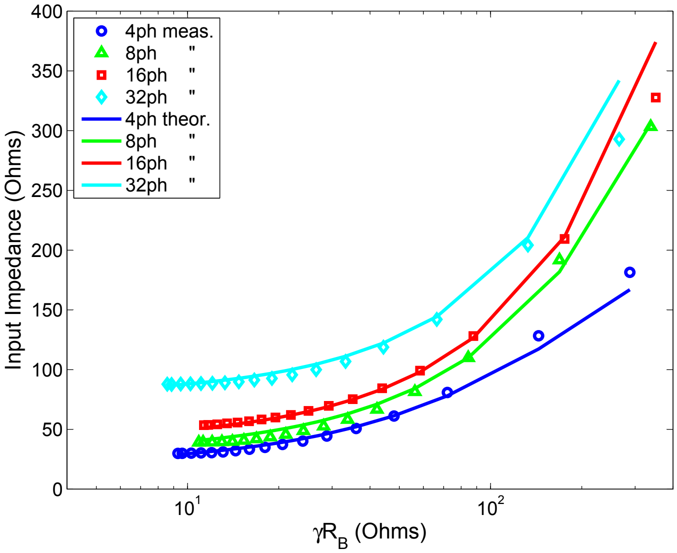

Figure 4.3: Measured input impedance Z_{in} at 200MHz, for each number of phases of the N-phase receiver, as a function of the baseband input resistance.

varying from 45 to 70mW (with split supplies of 1.2V and 2.5V for the LO and baseband respectively). The IIP_3 for 8-phase was measured to be +16dBm at 20MHz offset.

Figure 4.3 shows the input impedance of the receiver at 200MHz as a function of N and effective tuned input impedance of the baseband amplifiers. While the low end of Z_{in} asymptotes to the effective switch resistance for each case, the high end is dominated by

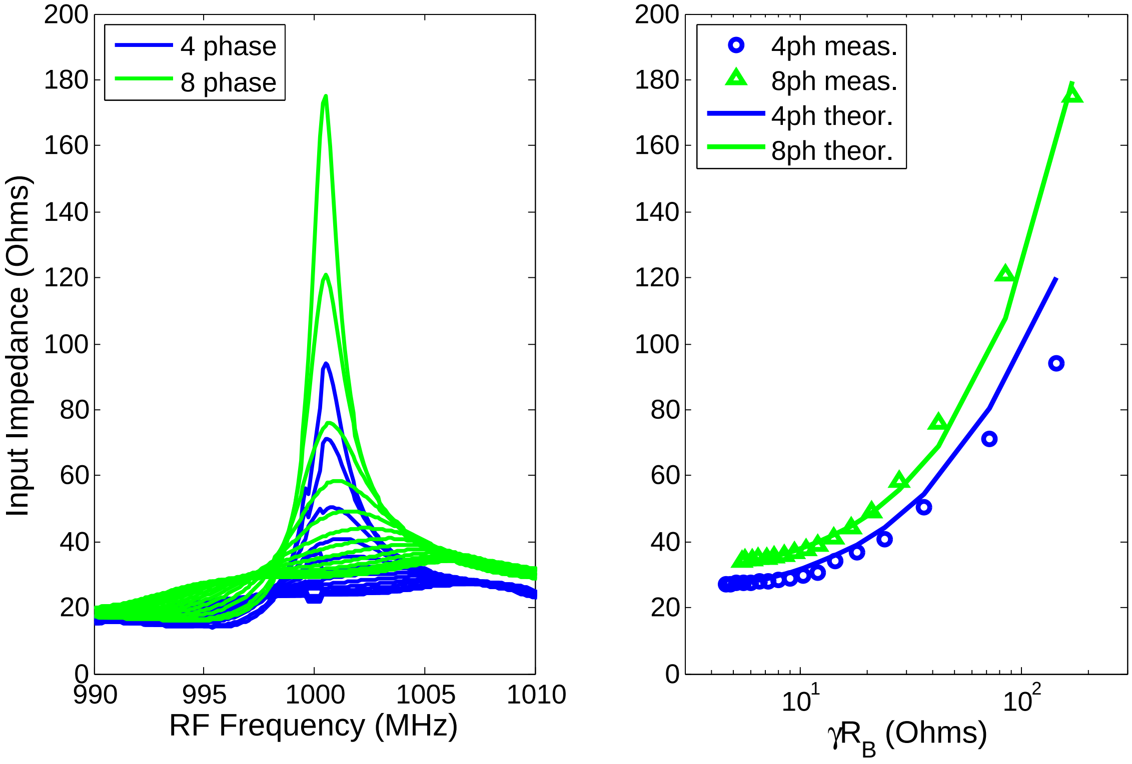

Figure 4.4: Measured input impedance Z_{in} around 1GHz, on the left around the LO frequency of 1GHz, on the right showing the impedance at the LO as a function the baseband input resistance.

Z_{sh}. Here we see the effects of the higher R_{sh} values when using >8 LO phases. Overlaid on the measured data are theoretical curves which are fitted with R_{sw} and amplifier gain, and with Z_{sh} calculated with purely real antenna impedance of 50Ω.

Figure 4.4 shows the same measurement as Fig. 4.3, except at f_{RF} =1GHz, with the addition of the raw impedance data from the network analyzer across frequency (similar to Fig. 4.2). As we move to these higher receive frequencies, we see that the measured Z_{in} does not follow the theoretical one at higher values. This is likely because our model treats Z'_a as a wideband 50Ω, whereas packaging and mixer parasitics will start to reduce Z'_a at the harmonics of the RF frequency, shunting harmonics, and so reducing R_{sh} [30]. This effect is especially pronounced for 4-phase case, where proportional decreases in

R_{sh}, which was intrinsically lower to begin with, have a stronger influence on impedance.

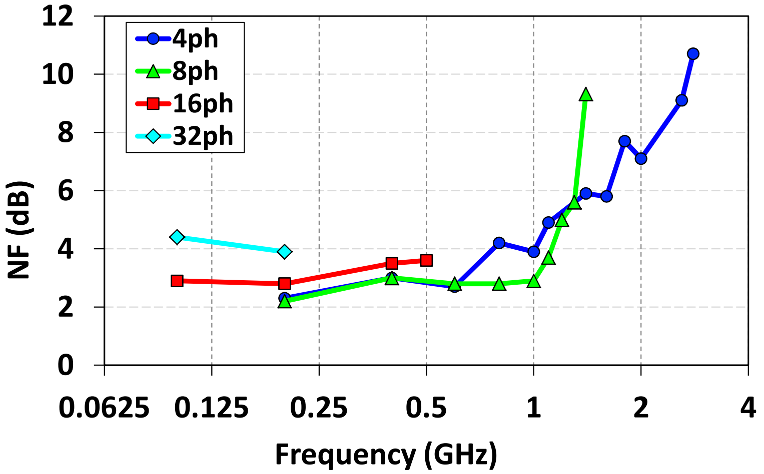

Figure 4.5: Measured NF of the N-phase non-overlapping receiver across frequency, and for each number of phases.

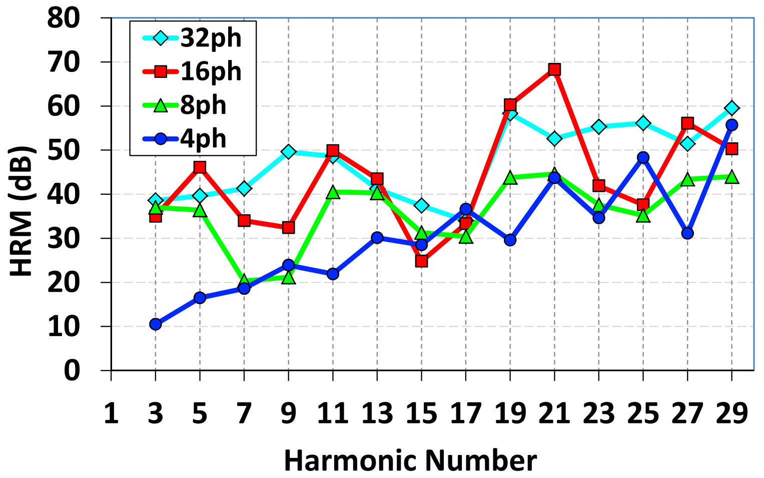

Figure 4.6: Measured harmonic rejection ratio of the receiver, for each number of phases, for a fundamental of 200MHz.

Figure 4.5 shows the NF of the N-phase receiver across its entire frequency range of operation. Because the LO dividers only worked up to input LO frequencies of ~6GHz, this placed limits on the range of operation for each number of phases. However we see that the receiver is able to achieve NF<4dB for all numbers of phases for frequencies below 1.2GHz. For N=4, 8 and 16, the roughly equal NF can be explained as a balancing-out of increased noise from increased R_{sw} with decreased noise from increased R_{sh}. $N = 32$ has the highest NF at low frequencies as its higher switch resistance begins to dominate. With increasing f_{RF}, the NF degrades as a result of both RF-port parasitics and LO pulse non-ideality. Capacitive parasitics decrease R_{sh}, impacting noise directly, especially affecting the $N = 4$ case (compare $N = 4$ and $N = 8$ for $f_{RF} > 600MHz$.

Figure 4.6 shows the harmonic rejection of the receiver when operated at each number of phases with an f_{RF} of 200MHz. We chose a low frequency here in order to show the difference between the HRM capabilities of the standard 4 and 8 phases and our higher numbers of phases (16 and 32). The data shows an increase HRM ratio across most of the frequency range for $N = 16$ and 32. The rejection is achieved via current summation of the various phases, to the closest 1/16 of the desired weighting (4-bit encoding), and is likely further degraded by imperfect gain matching between the various baseband paths. Nevertheless, this kind of N-phase LO scheme, combined with a stronger (likely adaptive) harmonic recombination scheme will be crucial to operating wideband receivers across more than a decade of receive frequency without filtering.

4.4 Overlap current description and reduction scheme

One of the biggest design challenges when using passive mixers is the generation of non-overlapping, multi-phase, multi-GHz LO pulses. This necessitates fast, wide fan-out digital switching circuits, which dominate the power consumption of a receiver. A non-overlapping N-phase clock must switch $N/2$ times faster than a 50% duty cycle clock with the same number of phases. We have characterized the effects of overlap on the gain and input impedance of the receiver (which in the case of passive mixer-first receivers, are related).

As seen in Fig. 4.7.a), when passive mixer LO pulses overlap, more than one of the mixer switches presents a low impedance to the RF port at a time. The result is a current I_{OL} which flows during the overlapping period from one sampling capacitor to the next, dissipating energy from the baseband signal. We model this charge-sharing as an overall shunt impedance to the system, which acts in parallel with the R_{sh} we use to model power lost to harmonic up-conversion.

$$Z_{in} = R_{sw} + \gamma R_B \parallel Z_{sh} \parallel Z_{OL} \tag{4.5}$$

This overlap leakage current will have its fundamental frequency components at $f_{OL} = f_{LO} \cdot (N/2 \pm 1)$, corresponding to a series of leakage pulses at each overlap time. In this chapter, we focus our attention on an overlapping period which is at most 1/2 the overall pulse width. That is to say that each sampling capacitor will only share charge

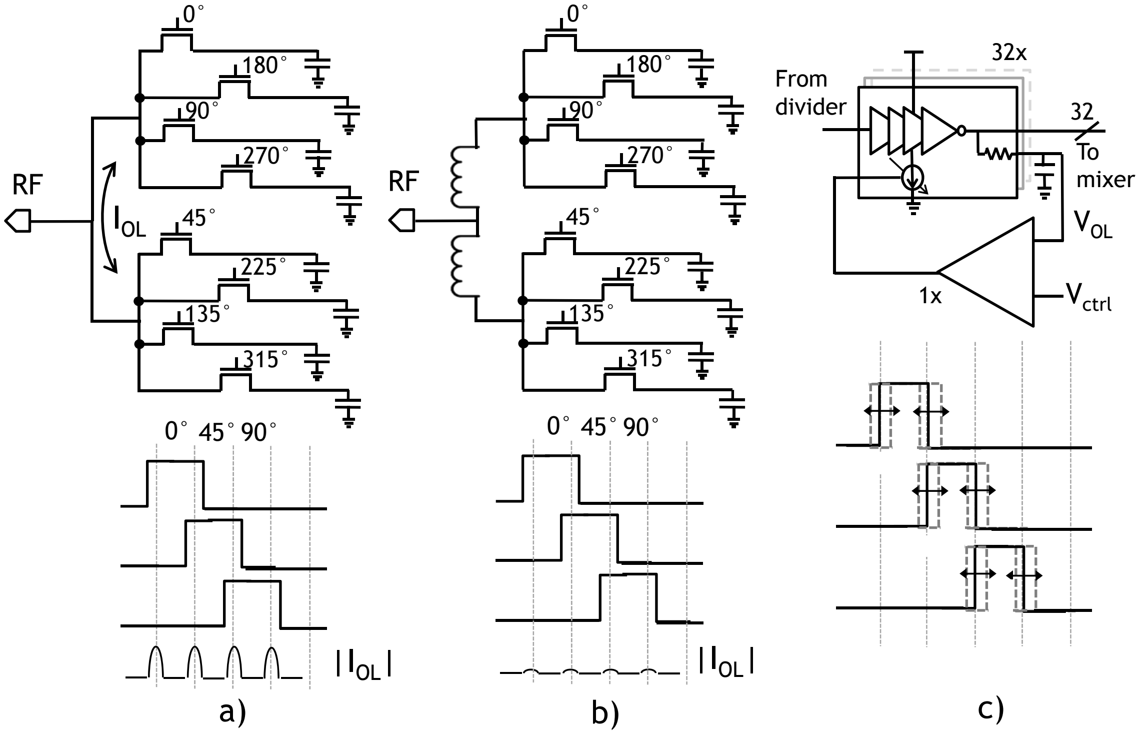

Figure 4.7: Overlap current description and reduction scheme

with up to two others (those with adjacent phases).

To better understand overlap effects, one can treat the RF path as two separate mixers, as shown in Fig. 4.7.a). Each mixer contains half of the overall mixer switches, and the switches driven by adjacent LO pulses are placed in separate mixers. In this arrangement, the current due to overlap, I_{OL} flows back and forth between these two sub-mixers. Figure 4.7.b) shows our overlap current choking technique, where two inductors are placed in series between the split mixers. These inductors are sized so that they look relatively low impedance (sub 10Ω) when viewed in parallel at the desired RF frequencies of the receiver, but present an impedance much higher than R_{sw} when viewed in series at overlap frequency (note that f_{OL} scales with N, so that even at low receive frequencies, f_{OL} may be quite high). This means that when two mixer switches are on at the same time, relatively little current will flow between them, suppressing this leakage. In simulation, this technique showed an improvement in the NF of the mixer from 6dB to 1dB for an 8-phase mixer with 25% duty cycle pulses (meaning each LO pulse overlapped completely its two adjacent pulses).

In order to verify the effect of overlap current on the receiver input impedance, we have implemented a tunable delay line to provide programmable degrees of overlap between the pulses. This delay line takes the $2/N$ duty cycle pulses coming from the frequency divider and feeds them into a line of inverters with controllable, asymmetric delays for rising and falling edges. The averaged delay of the 32 lines is wrapped in a feedback loop that matches pulse duty cycle to an external voltage. The duty cycle can be set to generate overlapping pulses, non-overlapping pulses, and even “underlapping” pulses with period where no mixer switches are on. As the degree of overlap is changed in the pulses, we expect a drastic difference in the input impedance of the receiver as leakage currents shunt the incoming signal.

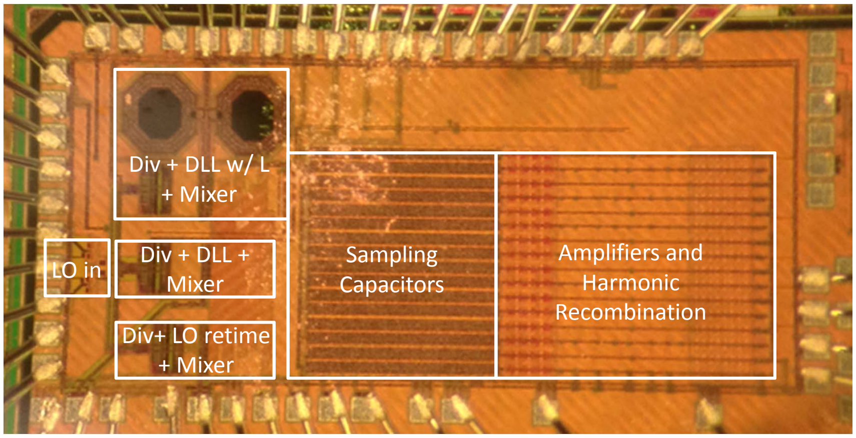

Figure 4.8: Microphotograph of implemented receivers

4.5 Overlap Measurement Results

In addition to the receiver detailed in Fig. 4.1, we also implemented two additional RF front-ends which share an identical baseband, as seen in the die photo in Fig. 4.8. The standard front-end with LO pulse retiming on the bottom, a front-end with the retiming replaced with the DLL from Fig. 4.7.c), and third front-end with the DLL and the RF input split by two 3nH choke inductors, as in Fig. 4.7.b).

For the two receivers with controllable overlap, we measured Z_{in} as a function of both the degree of overlap given by V_{OL} from Fig. 4.7.b) and the feedback resistors in the baseband amplifiers. Figure 4.9 shows measured input impedance as a function of duty cycle, presence of inductors, and R_B for an f_{RF} =500MHz for N=8-phase operation. The receivers show a similar impedance for a non-overlapping duty cycle of 12.5%. As the pulse width increases past 12.5%, the maximum in-band input impedance drops rapidly for the un-choked design, but stays close to the ideal value when choke inductors are included. We were unable to veryify the expected associated improvement in NF as the delay lines used to control duy cycle also back-injected significant noise onto the RF port degrading NF. However, since including these inductors dramatically increases the maximum reachable impedance (set by shunting losses) while only mildly affecting the minimum impedance presented by the mixer, this approach significantly extends the impedance tuning range and enhances the filtering performance as LO pulses start to overlap.

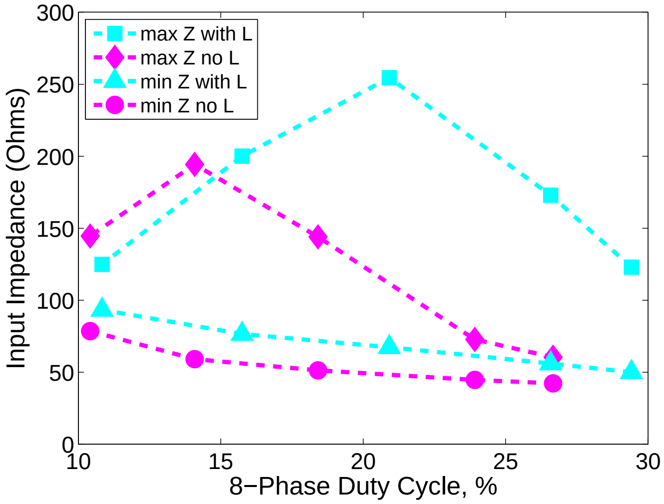

Figure 4.9: Measurement of Z_{in} of the tunable overlap receivers, as a function of duty cycle, where 12.5% is completely non-overlapping

4.6 Conclusion

In this chapter we have presented a passive mixer-first receiver with a selectable number of phases from 4 to 32. This allows the receiver to reject up to the 30th harmonic, and operate up to 2.8GHz, while achieving NFs below 3dB for most frequencies below 1GHz. We have also investigated the effect of LO overlap on shunting impedance, and implemented a structure to mitigate these effects even under large amounts of overlap.

CHAPTER 5

A <12MW, 0.7-3.2GHZ RECEIVER WITH RESONANT MULTI-PHASE LO AND CURRENT REUSE HARMONIC REJECTION BASEBAND

In this chapter we present a wide tuning range passive mixer-first receiver with resonant non-overlapping LO drive and noise-power optimized multi-path baseband amplifier [46]. The receiver consumes 10-12mW (including VCOs, pulse generation and baseband) over a frequency range of 0.7-3.2GHz with a 1.3V supply. An LO generation architecture generates a 12.5% duty cycle resonant clock from standard complementary LC-tank VCOs. A capacitor sharing technique on the baseband side of the mixer doubles the RX frequency range of the 8-phase clock, achieving a NF as low as 7dB. The 1.8mW low noise baseband amplifier reuses the bias current of its four input channels while rejecting the $3^{rd}/5^{th}$ harmonics by >34dB.

5.1 Introduction

Recent interest in single chip software defined radios has led to the development of many low noise, highly linear, wideband receivers based on passive mixers [9, 41, 47]. These mixers provide both filtering and frequency downconversion across a wide frequency range limited only by the tuning range of the pulsed LO that drives them.

In exchange for flexibility, power consumption of SDRs has increased significantly relative to comparable narrowband architectures. This is largely due to the digital frequency dividers used to expand the frequency range and drive the large transistors associated with low noise passive mixers. In narrowband architectures the most efficient way to drive large switches is to incorporate their capacitance into a resonant tank, allowing for very low power [8]. Unfortunately, highly efficient resonant structures do not lend themselves to wide tuning ranges, thus establishing a trade-off between easily programmable, power hungry digital circuits driving large switches, and less easily tunable voltage controlled LC-oscillators with mixers incorporated into their tanks.

Additionally, recent work has shown that driving passive mixer transistors with non-overlapping, 25% or 12.5% duty cycle LO pulses provides better noise figure and linearity [18, 41], but places further demands on the LO generation. Generating 12.5% duty cycle pulses allows for harmonic rejection, but limits the ranges of such receivers because the VCO frequency must be divided by 4 instead of 2. Most designs generate these pulses from differential LO signals fed into frequency dividers, whose 50% duty cycle outputs are AND-ed together to create non-overlapping pulses [18]. The pulses are then heavily buffered to drive the large switches of the mixer.

In this paper we present a passive mixer-first receiver equipped with three techniques for saving power while maintaining high tunability with only mild degradation noise and linearity performance: 1) An LO generation scheme which provides eight resonant non-overlapping pulses 2) a method to combine the outputs of 8-phase mixers at baseband to effectively double the RX frequency range, 3) a noise and power optimized 4 input harmonic rejection baseband LNA.

5.2 Resonant 8 phase mixer drive

Figure 5.1 shows the 8-phase passive mixer driven by resonant non-overlapping pulses. A VCO operating at 4 times the desired RF frequency drives a divide-by-4 Johnson counter whose outputs are AND-ed together to generate 8 phases with 25% duty cycle. The outputs of the divider are connected to the gates of eight NMOS transistors which constitute an RF MUX. One at a time, phases 0°, 90°, 180° and 270° connect their mixer

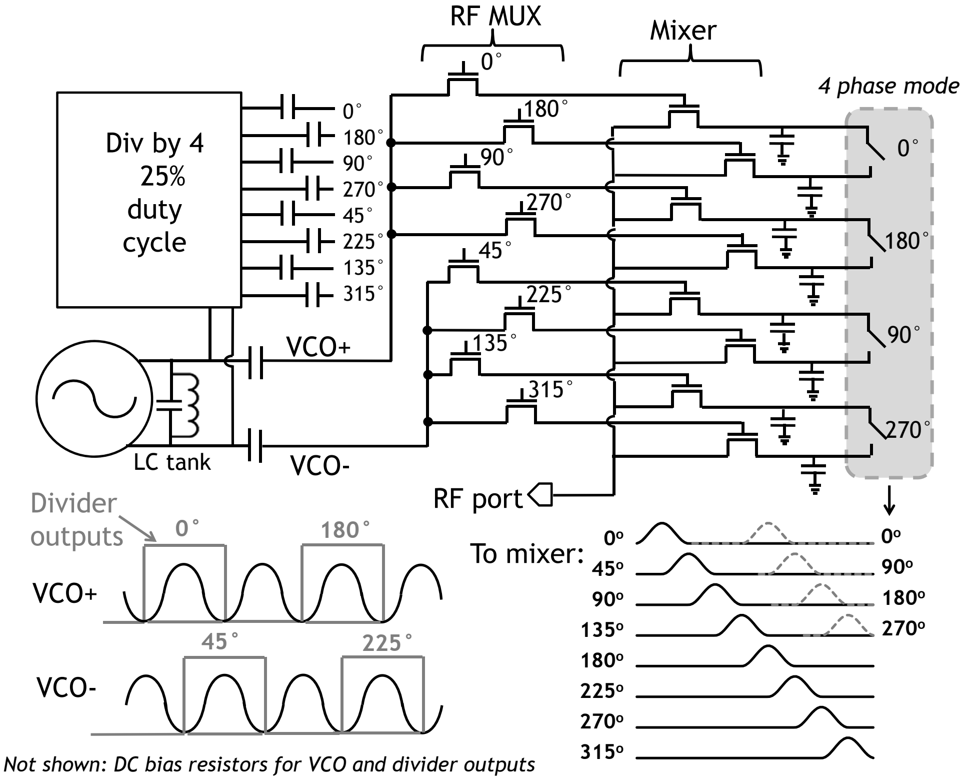

Not shown: DC bias resistors for VCO and divider outputs

Figure 5.1: Schematic diagram and waveforms for the resonant drive LO generation and passive mixer.

switch to one side of the VCO (VCO+). The other four phases short their mixer switches to the other side of the VCO (VCO-). Both sides of the VCO see a constant load of one mixer switch. The tank of the VCO therefore incorporates the mixer switch capacitance directly, without lossy digital buffering.

This approach leads to a fundamental trade-off: the RF MUX devices must be wide enough that their series resistance minimally decreases the amplitude of the signal coming from the VCO (and so minimally reduces the Q of the oscillator's tank). However, because the MUX is driven by purely digital circuits (the frequency divider), its size directly affects the power consumption. This trade-off can be quantified by observing that for a given V_{GS}, channel length and process, the product of an NFET's on-resistance and gate capacitance is independent of width, and has a characteristic cut-off frequency:

$\omega_{sw} = (R_{on}C_g)^{-1}$.

Given a MUX-to-mixer switch ratio of $F = W_{mix}/W_{mux}$, an oscillator with frequency ω_{osc} and differential peak amplitude of V_{DD}, the LO signal at the gates of the mixer will have peak-to-peak amplitude $V_{DD}/|1 + \frac{jF\omega_{osc}}{\omega_{sw}}|$. Keeping strong coupling from oscillator to mixer implies $F\frac{\omega_{osc}}{\omega_{sw}} \ll 1$. For a mixer with gate capacitance C_{mix}, and an unloaded oscillator quality factor of Q, the power dissipated to drive the mixer will be:

$$P \approx V_{DD}^2 C_{mix}\omega_{osc}\left(\frac{F\frac{\omega_{osc}}{\omega_{sw}}}{1 + (F\frac{\omega_{osc}}{\omega_{sw}})^2} + \frac{1}{F\pi} + \frac{1}{4Q}\right) \tag{5.1}$$

Which compares favorably with the power required to directly digitally drive the mixer:

$$P \approx \frac{V_{DD}^2 C_{mix}\omega_{osc}}{\pi} \tag{5.2}$$

In fact, greater savings can occur because the reduced digital drive (by $1/F$) applies not only to the MUX drivers, but to digital circuits in the dividers as well. In this design we used a fan-out factor of $F = 4$, which provided a reasonable trade-off between the series resistance and capacitive load presented by the MUX transistors.

This method provides benefits similar to the LO re-timing used in purely digital non-overlapping pulse generators. Because the actual switching times of the mixer are independent of the precise divider switching times (depending upon the resonant core of the oscillator instead), the dividers do not, to first order, contribute to the phase noise of the down-conversion [41].

This architecture alone will receive signals at $1/4$ the VCO frequency. To provide an additional octave of range, we have placed a set of switches on the mixer outputs to short together the anti-phase outputs of the 8-phase mixer (see right side of Fig. 5.1). Since the LO pulses remain the same, the RF signal will be sampled twice as often onto the shorted output capacitors, allowing the receiver to down-convert signals at twice the output frequency of the dividers. This is equivalent to using a 4-phase mixer with 25% duty cycle LO. This method of switching between sampling capacitors on the baseband side of the mixer simplifies the LO architecture, saving power.

5.3 Receiver Architecture

Figure 5.2 shows the block diagram of the receiver. Two complementary LC-tank VCOs cover a frequency range of 2.8-6.4GHz, each with 6 bit capacitor resolution and a varactor for fine tuning. Using the 8 to 4 phase mode-switching, this translates to effective RX range of 0.7-3.2GHz. Each VCO has its own divide-by-4 which generates 25% duty cycle pulses to drive the RF MUX. Each mixer transistor has two MUX transistors connected to its gate, coupling it to the appropriate VCO. The MUX and mixer present a load of 60fF to each side of the VCO, which is about 3% of the total tank capacitance for the low VCO and 6% for the high VCO. The mixer outputs are connected to transmission gates which switch between the 4 and 8 phase states by providing low resistance connections between the sampling capacitors. The outputs are then directed to the baseband LNA through large AC coupling capacitors, allowing for independent biasing of the baseband amplifier.

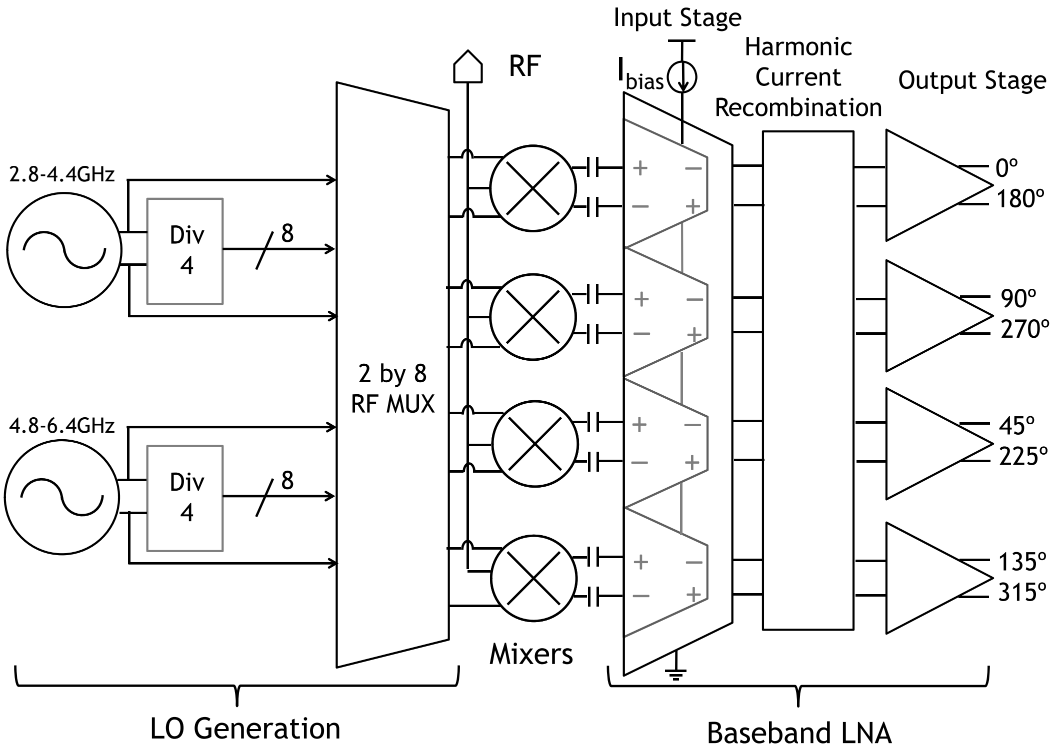

Figure 5.2: Block diagram of receiver with VCOs, pulse generation, passive mixer, and orthogonal current reuse amplifier.

5.4 Orthogonal Current Reuse Baseband LNA

Since input-referred noise in an amplifier is directly related to bias current, the second major consumer of power in an RF receiver is its LNA, be it an RF LNA before the mixer, or a baseband LNA after the mixer. To alleviate this trade-off, we applied a technique recently developed for implantable neural amplifiers [48], and incorporated harmonic rejection [18, 41]. Figure 5.3 shows the schematic diagram of the orthogonal current reuse baseband LNA. The amplifier design minimizes the noise-power trade-off by reusing bias current through four stacked differential amplifier input channels.

The first channel (the 0° and 180° phases from the mixer) is connected to the inputs of the top differential pair, which is biased by tail current I_{bias}. The two output currents

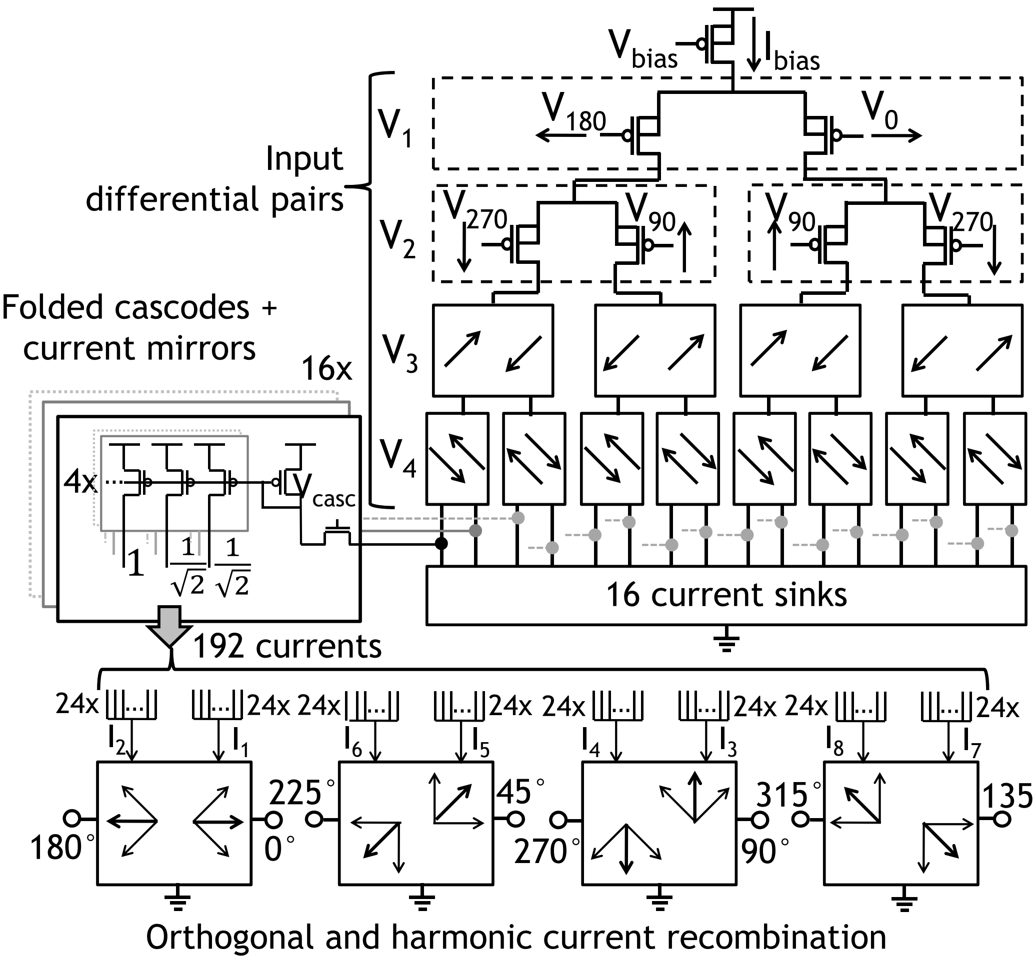

Figure 5.3: Schematic diagram of orthogonal current reuse harmonic recombination amplifier.

from the first channel provide tail currents equal to $I_{bias}/2 \pm g_m V_1$ (where $V_1 = V_0 - V_{180}$) to two identical differential pairs, which share the same inputs (V_{90} and V_{270} from the mixer). All of the input devices are long channel PFETs, biased in sub-threshold. The signal currents from V_1 are common-mode to channel two, with total current I_{bias}, so the combined transconductance of the channel 2 differential pairs is independent of V_1, and equal to that of channel 1. The four output currents of channel 2 are used as tail currents for 4 parallel differential pairs in channel 3, and likewise the third channel generates bias current for the 8 differential pairs of the fourth channel. At the bottom of the input stack, the 16 signal currents pass through folded cascode transistors combined with a reduced bias current ΔI_{bias}, saving power in subsequent stages where noise-current trade-offs are relaxed. Each channel has the same input referred noise as would be expected for a single differential pair biased by I_{bias}. Including the power of the second stage, this architecture reduces the total power by a factor of 3 compared to four parallel amplifiers with the same input referred noise.

Following the folded cascode device, each of the 16 currents contains a unique combination of the four differential voltage inputs, and can be treated as 8 pairs of differential currents, related to the input voltages by the linear transform:

$$\begin{pmatrix} I_1 \\ I_2 \\ I_3 \\ \vdots \\ I_8 \end{pmatrix} = \frac{g_m}{8} \begin{pmatrix} 1 & 1 & 1 & 1 \\ 1 & 1 & 1 & -1 \\ 1 & 1 & -1 & 1 \\ \vdots & \vdots & \vdots & \vdots \\ 1 & -1 & -1 & -1 \end{pmatrix} \begin{pmatrix} V_1 \\ V_2 \\ V_3 \\ V_4 \end{pmatrix} = \frac{g_m}{8} \mathbf{A} \vec{v}_{in} \tag{5.3}$$

Where the rows of **A** are 1 followed by each possible combination of 1's and -1's.

The following stage of the amplifier (on the left and bottom of Fig. 5.3) performs two separate functions simultaneously: to retrieve the individual amplified input signals from these currents while also rejecting the signal content from the 3^{rd} and 5^{th} harmonics of the RF signal. Each of the cascode currents is mirrored 12 times: four times with a weight of 1 and 8 times with a weight of $1/\sqrt{2}$. These 192 currents are then combined into four differential output loads. The linear recombination of these currents generates a second matrix operation, **B**, such that $\vec{v}_{out} = R_L \mathbf{B} \vec{i}_{mid} = g_m R_L \mathbf{B} \mathbf{A} \vec{v}_{in}$. Thus, the 2^{nd} stage of the amplifier performs a matrix multiplication of the currents coming out of the stack such the output loads generate voltages which represent the amplified independent inputs.

Each load receives 24 currents, selected with the polarities which cancel the signal and noise from the other channels. In 4 phase mode, the current recombination is chosen as in [48] such that $\mathbf{B_{4ph}} = \mathbf{A}^{\mathrm{T}}$. In 8 phase mixer mode, this operation is combined with a redistribution of the $1/\sqrt{2}$ weighted current mirrors to the nearest neighbors in phase (+ and - 45°). Mathematically, this requires a current arrangement such that:

$$\mathbf{B_{8ph}} = \frac{1}{2}\begin{pmatrix} 2 & \sqrt{2} & 0 & -\sqrt{2} \\ \sqrt{2} & 2 & \sqrt{2} & 0 \\ 0 & \sqrt{2} & 2 & \sqrt{2} \\ -\sqrt{2} & 0 & \sqrt{2} & 2 \end{pmatrix}\mathbf{A}^{\mathrm{T}} \tag{5.4}$$

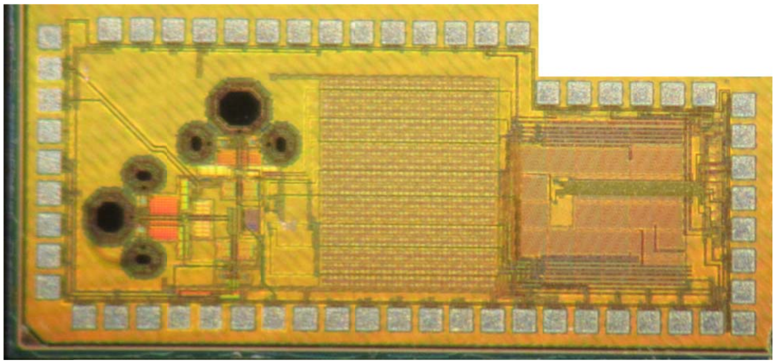

Figure 5.4: Microphotograph of implemented receiver

5.5 Measurement Results

The receiver was fabricated in 65nm CMOS, with an area of 2.9mm^2, as seen in Fig. 5.4. The total power consumption varies with the LO frequency from 10mW to 12mW. The receiver covers an RF frequency range of 0.7-3.2GHz when employing both 4 and 8 phase modes.

Figure 5.5 shows the NF and power consumption of the receiver across its entire

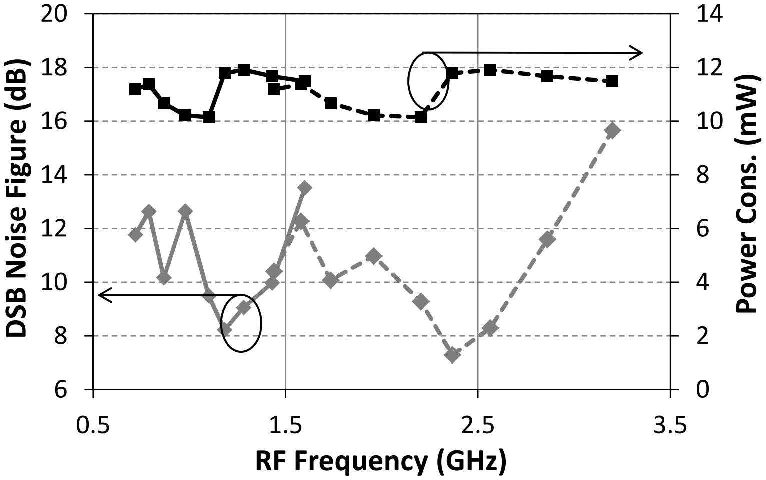

Figure 5.5: Measured noise figure and power consumption of entire receiver across RF frequency (dashed lines: 4 phase, solid lines: 8 phase).

Table 5.1: Performance Comparison

	This work	**[47]**	**[41]**	**[9]**	**[8]**
Topology	Mixer-first	LNA/Mixer-first	Mixer-first	Mixer-first	Mixer-first
Frequency [GHz]	0.7-3.2	0.4-6	0.1-2.4	0.2-2	2.4
Gain [dB]	36	70	70	19	17
DSB NF [dB]	7-16	3/6.5	4	6	11.5/6.5
OB-IIP3 [dBm]	4	10	25	11	-7
Power [mW]	10-12	30-55[a]	65[a]	67[a]	0.3/0.7[a]
Technology	65nm	40nm	65nm	65nm	.130μm

[a] Does not include VCO power

range of operating frequencies. The receiver achieves 7-13dB NF across 2GHz, while maintaining power consumption below 12mW. This compares with a simulated NF of approximately 5dB (3dB for the mixer, 2dB for the baseband). The LO power supply was increased to 1.3V from a nominal 1.2V in order to maintain the swing of the oscillators in the presence of unexpected parasitics. Changing frequencies results in a phase mismatch between the 25% duty cycle pulse coming from the divider and the oscillator output on the RF MUX. To accommodate for the difference, the delay in the buffer from VCO to divider was changed with frequency, helping to maintain performance across the entire range of operation. Note that switching from 8 phase to 4 phase (doubling the RF frequency) does not change the power consumption. At higher frequencies, increases in divider current are offset by decreases in VCO current due to higher tank Q at lower capacitance values.

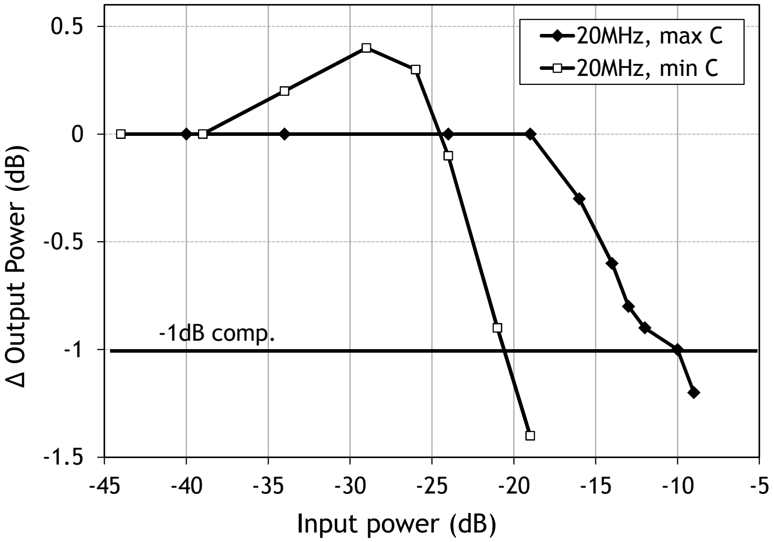

Figure 5.6: Measurement of -1dB compression point for two capacitor settings at f_{RF} =900MHz

We also characterized the out-of-band linearity of the receiver. Figure 5.6 shows the effects of filtering on compression by out-of-band interferers for two different values of the programmable baseband capacitor. As expected, interferers that are out-of-band (for maximum C) generate less nonlinearity than when inside the band (minimum C). We measured the out of band IIP3 to be +4dBm at 20MHz offset and the IIP2 was +24dBm. When we tried to characterize in-band linearity, we observed a dominant 5th order nonlinearity, presumably due to the baseband amplifier. The phase noise of the lower frequency VCO (fully loaded by the mixer) is −107dBc/Hz at 1MHz offset for 3.6GHz; that of the higher VCO was −100dBc/Hz at 5.9GHz.

Table 5.1 shows a comparison with other mixer-first designs. The baseband LNA consumes 1.8mW with each channel providing 36dB of receiver gain and 34dB of 3rd harmonic rejection (compared to 11dB in 4 phase mode). Harmonic rejection is only enabled in 8 phase mode, such that the 3rd and 5th harmonics are rejected for f_{RF} up to 1.6GHz.

5.6 Conclusion

In this work we developed techniques to drastically decrease the power consumption of highly tunable receivers. We present a method for generating resonant, non-overlapping pulses with 8 phases. Additionally we have doubled the range of a single ratio frequency divider in a passive mixer based receiver by recombining signals at the baseband side. Finally we have proposed a baseband amplifier scheme which reduces power by reusing bias current over 4 inputs, while also rejecting harmonics in a single stage.

Further improvements in the performance in this receiver could be made by increasing the LO swing on the passive mixer, which was somewhat less than V_{DD} due to imperfectly modeled parasitics. Modifying the VCO architecture to cross-coupled NFETs with a programmable current drive would allow us to increase the swing and improve noise and linearity performance for only a small cost in additional power consumption.

CHAPTER 6

FINAL COMMENTS

The works from the previous chapters contributed both to the theoretical understanding and the physical demonstration of wideband passive mixer-first receivers. However, the receivers presented were all based on a very similar architecture, and there remains much to be investigated about what other circuit functions could be achieved with passive mixers in general.

Notably, we did not present a transmitter, a crucial component of any wireless system. Developing a transmitter architecture that could work in conjunction with a passive mixer first receiver (using the same mixer) is a subject that should become of interest in the coming years.

The baseband RF mode switch from Chapter 5 is a technique which could be generalized to achieve other goals. The idea of manipulating the RF behavior with changes to the baseband (and particularly by combining mixer outputs together in different configurations) is likely to be much more powerful than what was demonstrated in this work (doubling the RF frequency by shorting baseband paths).

Overall, it seems as though the work to date on passive mixer structures in modern CMOS processes, presented in this dissertation and by others, has barely scratched the surface on what can be accomplished using these humble switches and capacitors.

BIBLIOGRAPHY

[1] J. Liu, G. Vandersteen, J. Craninckx, M. Libois, M. Wouters, F. Petre, and A. Barel, “A novel and low-cost analog front-end mismatch calibration scheme for MIMO-OFDM WLANs,” *IEEE Radio and Wireless Symposium*, pp. 219–222, Jan. 2006.

[2] A. van Bezooijen, M. de Jongh, C. Chanlo, L. Ruijs, F. van Straten, R. Mahmoudi, and A. van Roermund, “A GSM/EDGE/WCDMA adaptive series-LC matching network using RF-MEMS switches,” *IEEE J. Solid-State Circuits*, pp. 2259–2268, Oct. 2008.

[3] J. Craninckx, M. Liu, D. Hauspie, V. Giannini, T. Kim, J. Lee, M. Libois, D. Debaillie, C. Soens, M. Ingels, A. Baschirotto, J. V. Driessche, L. V. der Perre, and P. Vanbekbergen, “Fully reconfigurable software-defined radio transceiver in 0.13μm CMOS,” *ISSCC Dig. Tech. Papers*, pp. 346–347, Feb. 2007.

[4] A. Bourdoux, J. Craninckx, A. Dejonghe, and L. V. der Perre, “Receiver architectures for software-defined radios in mobile terminals: the path to cognitive radios,” *IEEE Radio and Wireless Symposium*, pp. 535–538, Jan. 2007.

[5] R. van de Beek, J. Bergerboet, H. Kundur, D. Leenaerts, and G. van de Weide, “A 0.6-to-10GHz receiver front-end in 45nm CMOS,” *ISSCC Dig. Tech. Papers*, pp. 128–129, Feb. 2008.

[6] J.-H. Zhan and S. Taylor, “A 5GHz resistive-feedback CMOS LNA for low-cost multi-standard applications,” *ISSCC Dig. Tech. Papers*, pp. 721–730, Feb. 2006.

[7] W.-H. Chen, G. Liu, B. Zdravko, and A. Niknejad, “A highly linear broadband CMOS LNA employing noise and distortion cancellation,” *IEEE J. Solid-State Circuits*, pp. 1164–1176, May 2008.

[8] B. Cook, A. Berny, A. Molnar, S. Lanzisera, and K. Pister, “Low power 2.4GHz transceiver with passive RX front-end and 400mV supply,” *IEEE J. Solid-State Circuits*, pp. 2757–2766, Dec. 2006.

[9] M. Soer, E. Klumperink, Z. Ru, F. V. van, and B. Nauta, “A 0.2-to-2.0GHz 65nm CMOS receiver without LNA achieving 11dbm IIP3 and 6.5 dB NF,” *ISSCC Dig. Tech. Papers*, pp. 222–223, Feb. 2009.

[10] S. Zhou and M.-C. Chang, “A CMOS passive mixer with low flicker noise for low-power direct-conversion receiver,” *IEEE J. Solid-State Circuits*, pp. 1084–1093, May 2005.

[11] A. Mirzaei, H. Darabi, J. Leete, X. Chen, K. Juan, and A. Yazdi, "Analysis and optimization of current-driven passive mixers in narrowband direct-conversion receivers," *IEEE J. Solid-State Circuits*, pp. 2678–2688, Oct. 2009.

[12] C. Andrews and A. C. Molnar, "A passive-mixer-first receiver with baseband-controlled RF impedance matching, < 6dB NF, and > 27dBm wideband IIP3," *ISSCC Dig. Tech. Papers*, pp. 46–47, Feb. 2010.

[13] A. Molnar, B. Lu, S. Lanzisera, B. Cook, and K. Pister, "An ultra-low power 900MHz RF transceiver for wireless sensor networks," *IEEE Custom Integrated Circuits Conf.*, pp. 401–404, Oct. 2004.

[14] N. Kim, L. Larson, and V. Aparin, "A highly linear SAW-less CMOS receiver using a mixer with embedded Tx filtering for CDMA," *IEEE J. Solid-State Circuits*, pp. 2126–2137, Aug. 2009.

[15] D. Kaczman, M. Shah, M. Alam, M. Rachedine, D. Cashen, L. Han, and A. Raghavan, "A singlechip 10-band WCDMA/HSDPA 4-band GSM/EDGE SAW-less CMOS receiver with DigRF 3G interface and +90 dBm IIP2," *IEEE J. Solid-State Circuits*, pp. 718–739, Mar. 2009.

[16] H. Khatri, L. Liu, T. Chang, P. Gudem, and L. Larson, "A SAW-less CDMA receiver front-end with single-ended LNA and single-balanced mixer with 25% duty-cycle LO in 65nm CMOS," *IEEE Radio Frequency Integrated Circuits Symp.*, pp. 13–16, Jun. 2009.

[17] M. Camus, B. Butaye, L. Garcia, M. Sie, B. Pellat, and T. Parra, "A 5.4 mW/0.07 mm^2 2.4 GHz front-end receiver in 90 nm CMOS for IEEE 802.15.4 WPAN standard," *IEEE J. Solid-State Circuits*, pp. 1372–1383, Aug. 2008.

[18] Z. Ru, N. Moseley, E. A. M. Klumperink, and B. Nauta, "Digitally enhanced software-defined radio receiver robust to out-of-band interference," *IEEE J. Solid-State Circuits*, pp. 3359–3375, Dec. 2009.

[19] K.-W. Cheng, K. Natarajan, and D. Allstot, "A current reuse quadrature GPS receiver in 0.13 μm CMOS," *IEEE J. Solid-State Circuits*, pp. 510–523, Mar. 2010.

[20] J. Weldon, R. Narayanaswami, J. Rudell, L. Lin, M. Otsuka, S. Dedieu, L. Tee, K.-C. Tsai, C.-W. Lee, and P. Gray, "A 1.75-GHz highly integrated narrow-band CMOS transmitter with harmonic-rejection mixers," *IEEE J. Solid-State Circuits*, pp. 2003–2015, Dec. 2001.

[21] M. Kitsunezuka, S. Hori, and T. Maeda, “A widely-tunable, reconfigurable CMOS analog baseband IC for software-defined radio,” *IEEE J. Solid-State Circuits*, pp. 2496–2502, Sep. 2009.

[22] R. Bagheri, A. Mirzaei, S. Chehrazi, M. E. Heidari, M. Lee, M. Mikhemar, W. Tang, and A. A. Abidi, “An 800-MHz–6-GHz software-defined wireless receiver in 90-nm CMOS,” *IEEE J. Solid-State Circuits*, pp. 2860–2876, Dec. 2006.

[23] H. Song, B. Bakkaloglu, and J. T. Aberle, “A CMOS adaptive antenna-impedance-tuning IC operating in the 850MHz-to-2GHz band,” *ISSCC Dig. Tech. Papers*, pp. 384–385, Feb. 2009.

[24] J. Ryynanen, S. Lindfors, K. Stadius, and K. Halonen, “Integrated circuits for multi-band multi-mode receivers,” *IEEE Circuits and Systems Mag.*, pp. 5–16, Jul. 2006.

[25] K. Lim, S.-H. Lee, S. Min, S. Ock, M.-W. Hwang, C.-H. Lee, K.-L. Kim, and S. Han, “A fully integrated direct-conversion receiver for CDMA and GPS applications,” *IEEE J. Solid-State Circuits*, pp. 2408–2416, Nov. 2006.

[26] T. Tikka, J. Ryynanen, and K. Halonen, “Multiband receiver for base-station applications,” *IEEE Radio and Wireless Symposium*, pp. 871–874, Jan. 2008.

[27] J. A. M. Jarvinen, J. Kaukovuori, J. Ryynanen, J. Jussila, K. Kivekas, M. Honkanen, and K. A. I. Halonen, “2.4-GHz receiver for sensor applications,” *IEEE J. Solid-State Circuits*, pp. 1426–1433, Jul. 2005.

[28] D. Tucker, “The history of the homodyne and synchrodyne,” *J. of the British Radio Engineers*, pp. 143–154, Apr. 1954.

[29] A. Mirzaei, H. Darabi, J. C. Leete, and Y. Chang, “Analysis and optimization of direct-conversion receivers with 25% duty-cycle current-driven passive mixers,” *IEEE Trans. Circuits Syst. I, Reg. Papers*, pp. 2353–2366, Sep. 2010.

[30] C. Andrews and A. C. Molnar, “Implications of passive mixer transparency for impedance matching and noise figure in passive mixer-first receivers,” *IEEE Trans. Circuits Syst. I, Reg. Papers*, pp. 3092–3103, Dec. 2010.

[31] H. Khatri, P. S. Gudem, and L. E. Larson, “Distortion in current commutating passive CMOS downconversion mixers,” *IEEE Trans. Microwave Theory Tech.*, pp. 2671–2681, Nov. 2009.

[32] A. Ghaffari, E. A. M. Klumperink, and B. Nauta, “A differential 4-path highly linear widely tunable on-chip band-pass filter,” *IEEE Radio Frequency Integrated Circuits Symp.*, pp. 299–302, Jun. 2010.

[33] M. C. M. Soer, E. A. M. Klumperink, P.-T. de Boer, F. E. van Vliet, and B. Nauta, “Unified frequency-domain analysis of switched-series-*RC* passive mixers and samplers,” *IEEE Trans. Circuits Syst. I, Reg. Papers*, pp. 2618–2631, Oct. 2010.

[34] X. He and J. van Sinderen, “A low-power, low-EVM, SAW-less WCDMA transmitter using direct quadrature voltage modulation,” *IEEE J. Solid-State Circuits*, pp. 3448–3458, Dec. 2009.

[35] L. Franks and F. Witt, “Solid-state sampled-data bandpass filters,” *ISSCC Dig. Tech. Papers*, pp. 70–71, Feb. 1960.

[36] H. Darabi, “A blocker filtering technique for SAW-less wireless receivers,” *IEEE J. Solid-State Circuits*, pp. 2766–2733, Dec. 2007.

[37] A. Mirzaei, X. Chen, A. Yazdi, J. Chiu, J. Leete, and H. Darabi, “A frequency translation technique for SAW-less 3G receivers,” *IEEE Symp. on VLSI Circuits*, pp. 280–281, Jun. 2009.

[38] N. Kim, V. Aparin, and L. E. Larson, “A resistively degenerated wide-band passive mixer with low noise figure and high IIP2,” *IEEE Trans. Microwave Theory Tech.*, pp. 820–830, Apr. 2010.

[39] E. A. Keehr and A. Hajimiri, “A rail-to-rail input receiver employing successive regeneration and adaptive cancellation of intermodulation products,” *IEEE Radio Frequency Integrated Circuits Symp.*, pp. 47–50, Jun. 2010.

[40] O. E. Erdogan, R. Gupta, D. G. Yee, J. C. Rudell, J.-S. Ko, R. Brockenbrough, S.-O. Lee, E. Lei, J. L. Tham, H. Wu, C. Conroy, and B. Kim, “A single-chip quad-band GSM/GPRS transceiver in 0.18μm standard CMOS,” *ISSCC Dig. Tech. Papers*, pp. 318–319, Feb. 2005.

[41] C. Andrews and A. C. Molnar, “A passive mixer-first receiver with digitally controlled and widely tunable RF interface,” *IEEE J. Solid-State Circuits*, pp. 2696–2708, Dec. 2010.

[42] D. Murphy, A. Hafez, A. Mirzaei, M. Mikhemar, H. Darabi, M.-C. F. Chang, and A. Abidi, “A blocker-tolerant wideband noise-cancelling receiver with a 2db noise figure,” *ISSCC Dig. Tech. Papers*, pp. 74–75, Feb. 2012.

[43] A. Mirzaei, H. Darabi, and D. Murphy, "Architectural evolution of integrated m-phase high-q bandpass filters," *IEEE Trans. Circuits Syst. I, Reg. Papers*, pp. 52–65, Jan. 2012.

[44] A. Ghaffari, E. Klumperink, and B. Nauta, "8-path tunable rf notch filters for blocker suppression," *ISSCC Dig. Tech. Papers*, pp. 76–77, Feb. 2012.

[45] C. Andrews, C. Lee, and A. Molnar, "Effects of lo harmonics and overlap shunting on n-phase passive mixer based receivers," *IEEE Eur. Solid-State Circuits Conf.*, Sep. 2012.

[46] C. Andrews, L. Diamente, B. Johnson, and A. Molnar, "A <12mw, 0.7-3.2ghz receiver with resonant multi-phase lo and current reuse harmonic rejection baseband," *IEEE Radio Frequency Integrated Circuits Symp.*, pp. 43–46, Jun. 2012.

[47] J. Borremans, G. Mandal, V. Giannini, B. Debaillie, M. Ingels, T. Sano, B. Verbruggen, and J. Craninckx, "A 40nm CMOS highly linear 0.4-to-6GHz receiver resilient to 0dBm out-of-band blockers," *IEEE J. Solid-State Circuits*, pp. 1659–1671, Jul. 2011.

[48] B. Johnson, D. DeTomaso, and A. Molnar, "A low-power orthogonal current-reuse amplifer for parallel sensing applications," *IEEE Eur. Solid-State Circuits Conf.*, pp. 318–321, Sep. 2010.